Efficient generation and characterization of soft x-ray by laser-driven high-order harmonic generation

ANNE-LISE VIOTTI

Master's Thesis at Paul Scherrer Institute
Supervisor at KTH: Valdas Pasiskevicius
Supervisor at PSI: Christoph Hauri
Examiner: Fredrik Laurell

TRITA-FYS 2014:53 ISSN 0280-316X ISRN KTH/FYS/–14:53–SE

Abstract

As a final year student specialized in laser physics and nonlinear optics at the Royal Institute of Technology (KTH, Stockholm), I chose to explore the field of high-harmonic generation by doing a master thesis at the Paul Scherrer Institute in Switzerland. There, in the laser group of the SwissFEL project, researchers are developing new table-top laser systems able to generate high-order harmonics in several gas media.

The context of this master thesis project is the future scientific large-scale facility under construction at Paul Scherrer Institute (PSI). The SwissFEL project is a x-ray free electron laser which should provide soon new opportunities for the research world.

The main advantage of this new type of light source is the ability to witness fast processes in detail. Those processes which can be found in nature or in the human body are occurring very rapidly. For instance, this kind of facility could help looking for new types of medicine drugs or new types of materials...

To develop this unique kind of light facility, PSI's researchers have gained experience with the SLS facility which is a synchrotron (Swiss Light Source). Among several areas of research, work on proton therapy was carried out in order to deal with certain types of cancer.

The aim of the master thesis is to investigate and characterize soft x-ray radiation. The scheme is based on nonlinear frequency conversion of an intense mid-infrared femtosecond laser by high-order harmonic generation (HHG). The photon energy range is hard to access by HHG at high flux and enhancement needs systematic investigations. During this project different experimental schemes will be explored and the obtained harmonic generation will be fully characterized thanks to different methods.

Contents

Chapter 1

Introduction

1.1 Master thesis project

The x-ray free electron laser source is based on electron accelerators which generate extremely short pulses of coherent x-ray light. The emitted radiation of such a facility is produced by the resonant interaction of a relativistic electron beam with a photon beam in an undulator. The main advantages of those light sources are that they are tunable, powerful and they provide coherent radiation. The first operation of a FEL occurred at Stanford University in 1977. Nowadays, we reached the 4^{th} generation of facilities with single pass FEL in SASE or seeded configuration.

Apart from these technical developments, such facilities are also considering several options for running FELs. The historical way is to use SASE (self-amplified stimulated emission). SASE is based on the interaction of the electron beam inside the undulator with the initial noisy radiation caused by the electron movement before they get bunched and emit in phase.

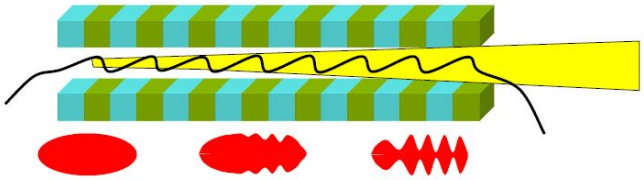

Figure 1.1: Self-Amplified Stimulated Emission sketch, *Tutorial on FEL, MAX-lab*

However, one problem with the SASE configuration for FEL is that this is a noisy startup process, meaning that the output radiation will lack of temporal coherence. Indeed, the different bunches of electrons emit with different phases and

the spectrum obtained at the output of a SASE FEL present spikes which vary shot-to-shot.
One alternate process is to use a seed, that is to say an external laser source that will come to seed the FEL. This laser must be tuned to the resonance of the FEL (matching of the wavelength required by the undulator configuration). Then the output radiation will have the coherence properties of the seed, that is to say a much better temporal coherence for instance because one will mainly coherently amplified the incident radiation. Thus the challenge is to produce this kind of seeding source. A possible candidate is HHG [1]. That is why we may use high-harmonic generation that allows reaching the appropriate wavelength range. Moreover, the use of HHG for seeding FEL provides improved conditions for pump-probe experiments, especially by allowing a better temporal coherence.

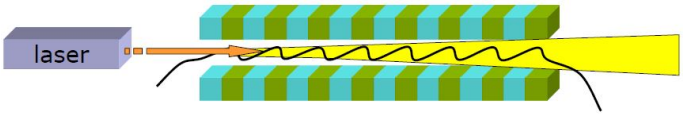

Figure 1.2: Seeding option with high harmonic generation, *Tutorial on FEL, MAX-lab*

Nevertheless, seeding options by HHG present some challenges, in particular it is difficult to reach the necessary seeding power at short wavelengths (typically under 20nm) to overcome the noise power of the SASE process. Indeed, the HHG power which is needed to start FEL radiation scales with the inverse of the wavelength of the FEL radiation [1].

The challenges of this master project are thus to characterize the high-harmonics generated in gas cells (hollow waveguides) in the spectral and temporal domains first in order to determine the pulse durations of the produced XUV beam. To maximize the generation, different focusing geometries can also be implemented. Then, another step would be to generate harmonics from a fundamental beam of higher wavelength which would allow reaching shorter harmonic wavelengths (see the cut-off law in chapter 2 which scales with λ^2).

1.2 The SwissFEL project

The SwissFEL facility will begin operation in 2016. Researchers will be able to carry out experiments at the facility for up to 5000 hours per year. The SwissFEL will also be the first energy-efficient x-ray free-electron laser because its power consumption will be drastically reduced compared to other facilities in Europe, Japan or the USA. Moreover, the facility will benefit from a heat recovery system

and the waste heat will be fed into PSI's heating network.
According to the theory of free-electron laser, the x-ray light of the facility is emitted by fast-moving electrons which are directed by powerful magnets to follow a narrow, slalom-shaped path. Indeed, when electrons are forced to change their velocity or direction of propagation, they act as dipoles emitting electromagnetic radiation as they move. Depending on the type of movement that the electrons undergo, the type of electromagnetic radiation can be selected. For instance it can be visible light or x-ray light.
The SwissFEL will have a length of 740 m and it will consist of four main sections. First, there is an electron injector followed by a linear accelerator. Then, one can find a series of undulators and finally all the required equipment to lead the experiments. In the injector, the electrons are extracted from a metal plate by a flash of light. They are then pre-accelerated by an electric field before going to the linear accelerator. They are first sent to a quadrupole magnet which guides the electron beam along the desired path. Then, in the linear accelerator, the electrons are accelerated to almost the speed of light by means of microwaves. As said previously, the electrons are sent to the undulators part where they follow a slalom-shaped path where they acquired kinetic energy. Those undulators are mainly constituted of periodically arrangement of alternately-oriented magnets. During this FEL process, which include micro-bunching, the electrons generate a coherent radiation (x-ray light) which in turn acts back on the electron beam which then radiate. The whole process is a circle. The facility involves 12 undulators, each having 1060 magnets (ultra-strong neodymium magnets). The whole part is 60 m long. The engineering challenge within this step is to guarantee the best 'phase-matching' between the electron beam and the x-ray radiation along the undulators. Once the x-ray light has been correctly generated, the electron beam is no longer needed so it is captured with the help of an electron absorber. Only the x-ray beam is left and directed towards the experimental stations where it will be available for use to researchers.

1.3 What is HHG

A nonlinear process is at the origin of the high-harmonic generation (HHG). It allows to convert standard available wavelengths (near infrared) into coherent radiation at shorter wavelengths, for instance in the extreme ultraviolet range or even in the soft x-ray domain. However, one must take care about the efficiency of this type of light conversion phenomena because it might turn to be very low and thus become a drawback in an experiment.
The best example of these nonlinear optical effects is the second harmonic generation or SHG. It was the first experimental demonstration of nonlinear optical effect in history (Franken, 1961) with a ruby crystal. However, this process involves the production of light with twice the frequency of the incident radiation.
What will be studied in this master thesis project is high-order harmonics, that is

to say generation of light with higher frequency multiples (generation of radiations with lower wavelength range) through nonlinear optical effects in gases.
In our case, high harmonics will be generated starting from an IR laser beam at around 800nm. We will be able to produce light falling in the XUV region (30 to 100nm) or even in the soft x-ray domain (0.2 to 30nm).

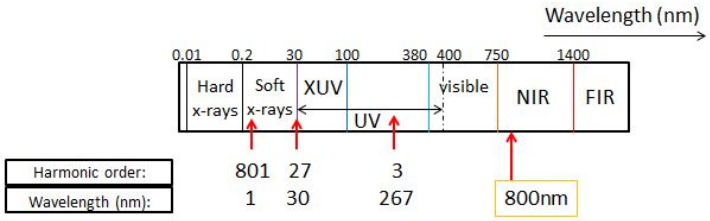

Figure 1.3: Electromagnetic spectrum and the harmonics of a light radiation at 800nm.

What is challenging concerning high-order harmonics is the waythey are generated. Indeed, they require quite extreme conditions. For instance, we must work in vacuum because of the strong absorption of air molecules in this range of short wavelength.

Moreover, HHG also requires that the generating medium is exposed to high intensity linearly polarized light, mainly intensities in the range of 10^{14} W/cm^2. So this can only be achieved by focusing ultrashort laser pulses, typically femtosecond pulses, on a gas jet. The basic setup for generating high harmonics is shown below:

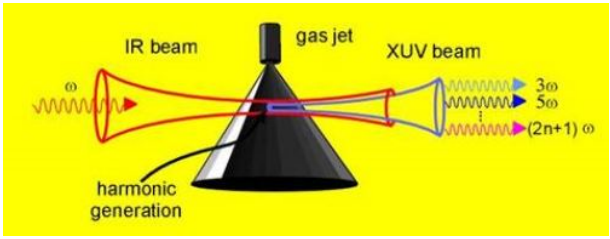

Figure 1.4: HHG setup of the Instituto Nazionale di Ottica, Italy.

Compared to conventional x-ray sources such as x-ray tubes, HHG sources have two strong advantages: they generate coherent radiation and they can provide very short pulses in the attosecond range. And this makes HHG suitable for different applications which require coherent radiations at such short wavelengths. HHG sources are less expensive than synchrotron or FEL sources and can be designed to be table-top devices, thus fitting in a conventional laser lab. High harmonics

also have a unique feature which make them very interesting for some applications. Indeed, they are produced in the form of very short light pulses of duration in the attosecond range.
On the other side, one must face a huge drawback with HHG, that is to say the efficiency of this process. Compared to the energy of the incident beam, the energy contained in the resulting harmonic beam is very small and the best efficiencies reported are around 10^{-4} for generation of radiation in the XUV domain. Moreover, HHG sources are polychromatic and give access to soft x-ray domain, whereas FEL and synchrotron have almost monochromatic radiation and allow to reach hard x-rays.

1.4 Applications of HHG

Apart form the seeding option for FEL, HHG is a source which can find applications in other domains of physics.
On first advantage of using HHG is the resolution achievable in certain circumstances. For example, in microscopy, the resolution of the optical imaging system is proportional to the wavelength used for illumination (in the diffraction limited case). This means that the resolution is enhanced by employing shorter wavelengths. This is called X-ray Transmission Microscopy (XTM)[2]. In this configuration the illumination of the sample is done in the soft x-ray range (achievable by HHG).

Theoretically a best resolution (down to 0.2nm) can be reached thanks to electron beams but in this case (Transmission Electron Microscopy TEM), one needs to freeze the samples and cut them in thin slices to be held in vacuum. This has the drawback that biological samples are no longer living. Using HHG may allow to work on living samples such as living cells.
Another advantage of the XTM technique involving HHG is that light radiation falling in the water window can be used thus allowing high contrast imaging in the region 280 to 420eV, that is to say around 2.96 to 4.43nm. In this domain, the absorption due to water molecules is weaker. As those molecules are relatively abundant in living samples, one can then image cells with high contrast (down to tens of nm).

1.5 The challenges of attosecond science

One unique feature of the HHG sources is that they provide trains of attosecond pulses. Attosecond science aims at studying and analyzing ultrafast phenomena which are likely to happen on attosecond time scales such as dynamics of electrons in a sample. This requires a good temporal resolution which can be reached via attosecond light pulses. It is like taking picture of an ultrafast process with the

corresponding ultrashort flash duration suitable for the illumination of the sample (mainly shorter time scale than the dynamics observed). Thus, it allows to take sharp pictures so that we get a better accuracy. The temporal resolution of the imaging system is then determined by the duration of the illumination.
However, such ultrafast experiments have drawbacks. First, how can we measure such short light pulse durations? This question is one of the leading axes of this master thesis project.

This report is organized as follows. First, it gives an introduction on high-harmonic generation theory in chapter 2. Then chapter 3 presents the laser driving system of the lab and some of its main features. The next chapter shows the experimental set-ups of the lab. Chapter 5 deals with the commissioning of a new x-ray spectrometer as a diagnosis tool for the HHG beam line. Chapter 6 aims at describing the optimization of the HHG beam line and finally chapter 7 presents the temporal reconstruction of XUV pulses thanks to THz streaking method.

Chapter 2

Introduction to high-order harmonic generation theory

This chapter highlights the basics of HHG theory by describing first the interaction between electrons and a given laser light.

2.1 Interaction with an electron

When an electron interacts with an intense laser beam, it starts to quiver. Actually, the electron is accelerating in the electric field of the light wave and submitted to the force (Lorentz picture):

$$\vec{F} = q\left[\vec{E} + \vec{v} \times \vec{B}\right] \tag{2.1}$$

Where q is the charge of the free electron and $\vec{E}$ is the electric field and $\vec{B}$ is the magnetic field of the optical wave. Speaking of intense laser pulse depends on the force it exerts on the electron. Basically, does it overpass the binding forces? But in the case of free electron, there is no binding force to compete with.

From equation (2.3):

$$\nabla \times \vec{E} = -\frac{\partial \vec{B}}{\partial t} \tag{2.2}$$

Thus we get, for an electromagnetic field of the form $\vec{E} = E\exp(\mathrm{i}\omega t)$ (where E describes the envelop of the field, so it has a slower variation):

$$\vec{B} = \frac{\mathrm{i}}{\omega}\nabla \times \vec{E} \tag{2.3}$$

From this starting point, the ponderomotive force can be derived [3]:

$$\vec{F} = -\frac{q^2}{4m\omega^2}\nabla|E|^2 \tag{2.4}$$

Where m is the mass of the electron and ω is the laser frequency. Thus, the ponderomotive potential is proportional to the laser intensity $|E|^2$:

$$U_{\mathrm{p}} = \frac{q^2}{4m\omega^2}|E|^2 = \frac{q^2}{4m\omega^2}I_{\mathrm{L}} \tag{2.5}$$

The ponderomotive potential increases with longer wavelengths. It is the energy acquired by the electron which is oscillating in the laser field.

2.2 Interaction laser-matter

What happens is that the pulse ionizes the medium, that is to say it takes away one electron from an atom of the medium. One should first understand how the electron is bound to the atom and how it can be taken away from it by the action of the laser pulses. The electron is bound to the atom thanks to a potential field around the core which acts as an attractive force onto the electron(s). This force is due to the electric positive charge of the nucleus and the expression of the potential U_{C} is the following (Coulomb force):

$$U_{\mathrm{C}} = -\frac{Zq^2}{4\pi\epsilon_0 r} \tag{2.6}$$

Where Z is the atomic number and r is the radial distance between the nucleus and the electron considered. When the electron is only submitted to this force, it stays bound to the nucleus. However, if an external optical wave is applied to the atom (for instance high-intensity laser pulses), then electrons can be taken away from the atom. Actually, this process can happen through different mechanisms which will be soon detailled. Then the question will be to determine in which case our set-up configuration is; and this is done by looking at the laser intensity applied to the atom.

So, what happens at the scale of the atom is that the applied intense electric field of the optical wave is acting on the Coulomb potential, mainly distorting it up to the suppression of the barrier potential for intensities above 10^{15} W.cm^{-2}. Then the electron is free to leave the surroundings of the nucleus. If the intensity of the incoming radiation is a bit lower, for instance starting around 10^{13} W.cm^{-2}, then the barrier is no longer suppressed but it is lowered and the electron can escape the nucleus bounding by tunneling mechanism.

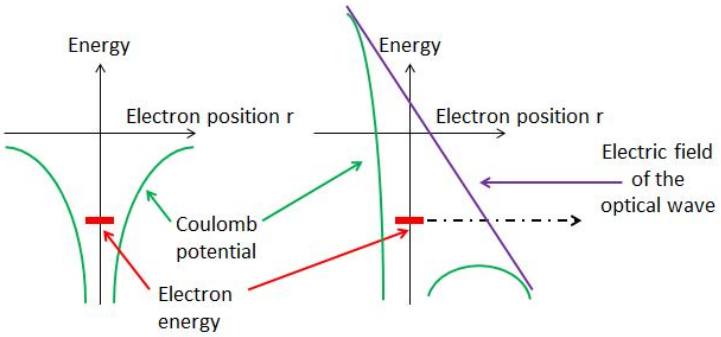

Figure 2.1: On this sketch on can see on the left the Coulomb potential in the usual configuration. On the right, an electric field is applied and the Coulomb potential is so much distorted that the barrier is suppressed and the electron can escape. This mechanism is called *over barrier ionization*.

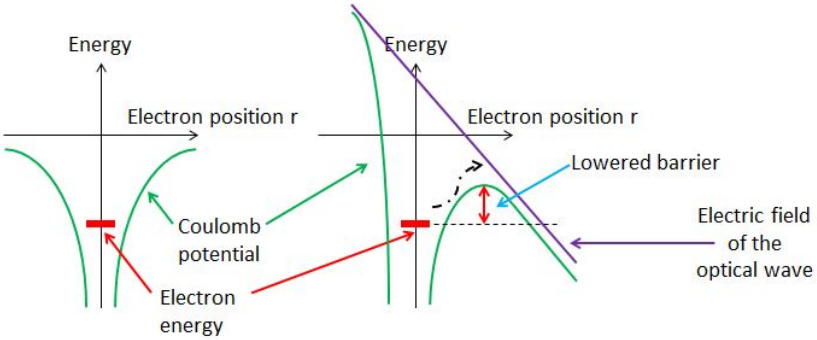

Figure 2.2: On this sketch one can see on the left the Coulomb potential in the usual configuration. On the right, an electric field is applied, a bit less intense than previously and the Coulomb potential is distorted so that the barrier is only lowered. The electron can still escape through a mechanism called *tunneling ionization*.

In our case the laser source is a Ti:Sa laser at 800nm with, for instance, a waist at the focus of $200\mu m$, pulse durations of around $55fs$ and an energy of 8mJ. This gives an intensity around 10^{14} W.cm^{-2}, so the second configuration is selected. More generally, the Keldysh dimensionless parameter can be introduced. It defines the transistion between the two regimes of ionization [22]

$$\gamma = \sqrt{\frac{I_{\mathrm{P}}}{2U_{\mathrm{P}}}} \tag{2.7}$$

Where I_P is the first ionization potential of the considered gas medium and U_P is the ponderomotive potential for the laser light. Thus, this parameter lets us compare the ionization potential of the electron and the ponderomotive potential of the laser. In the case $\gamma \gg 1$ the atomic potential will dominate the laser potential and we will get multi-photon ionization process, that is to say one electron of the atom will be removed if it absorbs a sufficient number of photons in order to acquire an energy equal to its binding energy. In the opposite case ($\gamma \ll 1$) the electric field of the laser is strong enough to distort the Coulomb potential and tunneling ionization mechanism will prevail.

In the case of barrier suppression, the electric field of the laser is strong enough to overcome the potential binding the electron to the nucleus. Thus it gives the following condition on the laser intensity:

$$I_S = 3.8 \times 10^9 \frac{{I_P}^4}{Z^2} \tag{2.8}$$

Where I_S is the threshold intensity in W/cm^2 that needs to be reached to get the suppression of the barrier potential, I_P is the ionization potential in eV and Z the atomic number.

There is also a maximal intensity for the laser beam, like a saturation intensity. This is the intensity above which ionization can not occur anymore because all the atoms of the medium have been ionized. This upper limit for the laser intensity is due to the lateral drift of the electrons which becomes stronger for intensities over $10^{17} W/cm^2$ and can prevent electron/ion recombination.

For the generation of harmonics, one must be in the case where $I_L \leq I_S$ because only the neutral atoms are likely to emit harmonics. The following table recall the first ionization energies and suppression intensities for the gases of interest for us:

Table 2.1: Useful potentials for neutral gases

Gas	I_P (eV)	I_S (W.cm^{-2})
Argon	15.76	2.34×10^{14}
Neon	21.56	8.2×10^{14}
Xenon	12.13	8.23×10^{13}
Helium	24.59	3.47×10^{14}

Finally, the ionization probability can be derived for an atom submitted to an optical wave thanks to the ADK model (from Ammosov-Delone-Krainov) [4]. It mainly gives the tunneling ionization rate in a given medium exposed to a given laser pulse.

2.3 HHG

Spectrum of HHG

High intensities are used to generate high-order harmonics and the perturbation theory common to usual nonlinear optics is no longer fully describing the polarization mechanisms of the nonlinear medium.
The conventional nonlinear optical phenomena we are used to study such as Second Harmonic Generation (SHG) are different processes: they belong to perturbative nonlinear optics. This is not the case for HHG, which is a non-perturbative nonlinear process.

The spectral characteristics of HHG is particular that is to say, it shows a *plateau* followed by a *cut-off* towards the harmonics of higher orders, that is to say there is a wavelength limit. This cut-off increases for higher laser intensities and it also depends on the gas used to generate the harmonics.

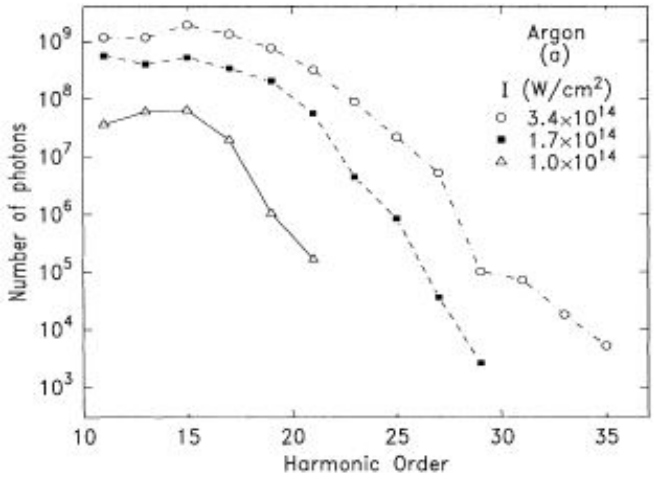

Figure 2.3: Some spectra obtained for high-harmonic generation in Argon with different laser intensities. The curves are issued from [5].

The energy corresponding to the cut-off frequency is expressed as follows:

$$E_{\mathrm{Cut}} = I_{\mathrm{P}} + 3.17 \times U_{\mathrm{P}} \tag{2.9}$$

Where I_{P} is the ionization potential and U_{P} is the ponderomotive potential. It defines the lower wavelength achievable on the HHG spectrum. All the lines which can be seen on an HHG spectrum are at odd frequency multiples of the fundamental

frequency of the laser light (800nm for us with Ti:Sa laser). The region called *plateau* is a domain where all the harmonic lines have the same intensity.

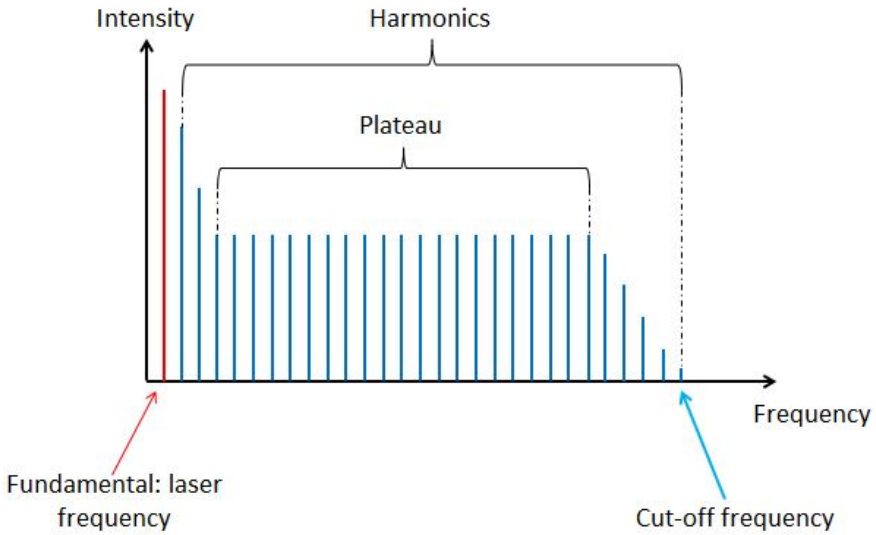

Figure 2.4: This sketch shows the aspect of the high-order harmonic spectrum, with the *plateau* region and the *cut-off* frequency.

The recollision picture

The generation of high-order harmonics is done in three steps. First, there is the ionization by tunneling effect thanks to strong enough laser intensity. Then, the electron taken away from the atom is accelerated by the the laser field in the direction perpendicular to the optical axis of propagation of the laser beam and does not feel any longer the effect of the attractive potential of the nucleus. Thus, it acquires a kinetic energy. Basically, the electron is pulled away from the nucleus. However, the laser field is oscillating and at one point it changes signs and the electron starts to decelerate up to reaching a zero-velocity position where it can recombine with a parent ion. While recombining, the electron can loose a part of the amount of kinetic energy it acquired. The energy which is then available after recombination is transferred to an electromagnetic wave and thus to light radiation, this is HHG. The emitted photon will have a total energy equal to the sum of the kinetic energy of the electron and ionization potential of the electron.

Two models were developed to explain these mechanisms: the Simpleman's classical model and the Lewenstein's quantum-mechanical description.

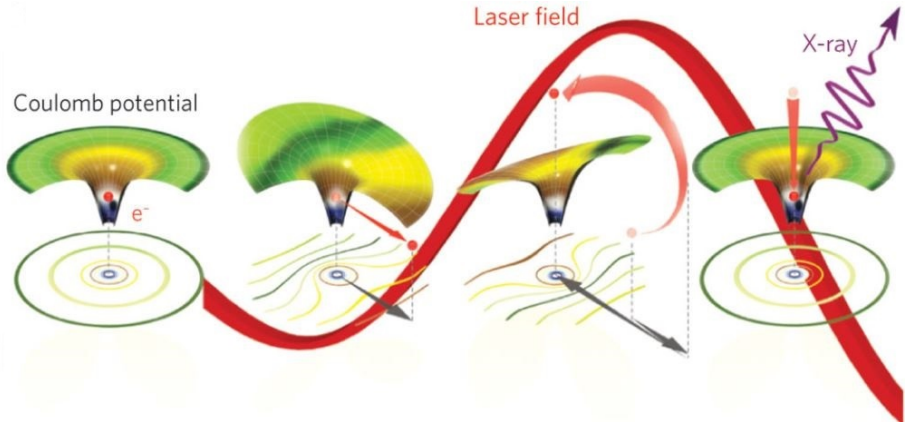

Figure 2.5: This sketch explains the three steps of high-harmonic generation. The figure is taken from [6].

Classical model

This model relies on basic assumptions.The velocity of the electron right after ionization can be considered as being zero and the dynamics of the electron in the laser field can be described as a classical free electron model.
Let's define the time right after the ionization step by t_0, then the velocity of the electron is:

$$v(t_0) = 0 \tag{2.10}$$

The laser field is assumed to be monochromatic, polarized in the x direction and is expressed as:

$$E(t) = E_0 \sin(\omega t) \tag{2.11}$$

The fundamental Newton's law for the dynamics is used:

$$\frac{d^2x(t)}{dt^2} = -\frac{eE_0}{m} \sin(\omega t) \tag{2.12}$$

Where e is the electron charge (absolute value). Then integration can be done, knowing the initial condition on the position and the velocity:

$$\frac{dx(t)}{dt} = \frac{eE_0}{m\omega} [\cos(\omega t) - \cos(\omega t_0)] \tag{2.13}$$

$$x(t) = \frac{eE_0}{m\omega^2} \left[\sin(\omega t) - \sin(\omega t_0) - \omega (t - t_0) \cos(\omega t_0)\right] \tag{2.14}$$

In the equation describing the velocity, two different term show up. First, the drift velocity which implies that the trajectory of the electron depends on the initial phase of the electric field of the optical wave, that is to say ωt_0:

$$v_{\text{drift}} = -\frac{eE_0}{m\omega} \cos(\omega t_0) \tag{2.15}$$

And second, the *quiver* term which describes the oscillations of the electron in the external laser field:

$$v_{\text{osc}} = \frac{eE_0}{m\omega} \cos(\omega t) \tag{2.16}$$

The photon emitted after the recombination process has the total energy of the electron, that is to say the acquired kinetic energy plus the ionization potential. The maximum photon energy which can be reached is function of the maximum kinetic energy which achievable by the electron. Let's look at the kinetic energy:

$$E_{\text{kin}} = \frac{1}{2} m \left(\frac{dx}{dt}\right)^2 \tag{2.17}$$

Thanks to equation (2.17), the cut-off law can be derived $E_{kin}^{max} = 3.17 \cdot U_{\text{P}}$.

Equation (2.18) describe the trajectory of the electron before recombination. Analytical calculations show that for $t_0 = 0$ and laser intensities of around $10^{16} W.cm^{-2}$ the electron can go away from the atom at a distance of around 20nm. One can divide trajectories into two categories: short and long trajectories depending on the path the electron is taking. But this result in same energies for the produced harmonics. It just means that the recombination can be achieved by two different paths.

It was said previously that the maximal energy which achievable in harmonics is a function of the ponderomotive potential:

$$E_{harm}^{max} = I_{\text{P}} + 3.17 \cdot U_{\text{P}} \tag{2.18}$$

This means that the shortest wavelength available is given by the formula:

$$\lambda_{harm}^{min} = \frac{hc}{E_{harm}^{max}} = \frac{hc}{I_{\text{P}} + 3.17 \cdot U_{\text{P}}} \tag{2.19}$$

Harmonics are produced at odd multiples of the fundamental frequency of the drive laser. The latter has a period $T = \frac{2\pi}{\omega}$ but then the electric field it carries changes direction twice in one laser period. In a centro-symmetric medium such as

atomic gas, the response from the field excitation is the same (change every half-cycle) so harmonics are produced each half-cycle for long driven field with many cycles. This means that the output radiation has a period of $\frac{T}{2} = \frac{\pi}{\omega}$. That is why, in the spectra domain, the harmonic lines are separated by 2ω starting from the fundamental frequency. So we generate 3ω, 5ω, 7ω and so on... that is to say odd multiples!

Quantum-mechanical description

This model is based on the Lewenstein's model [7]. In this case, the assumption is that $I_\mathrm{P} \ll U_\mathrm{P}$ such that the electron, once ionized, will no longer feel the attraction of the nucleus. This is called Strong Field Approximation (SFA). Moreover, I_P is large compared to the energy contained in one incoming photon (which is true because one photon at 800nm has an energy of 1.55eV).

The system's dynamics can be described by the time-dependent Schrödinger equation:

$$\mathrm{i}\hbar\frac{\partial}{\partial t}\left|\psi(t)\right\rangle = \left[-\frac{\hbar^2}{2m}\nabla^2 + V(t)\right]\left|\psi(t)\right\rangle \tag{2.20}$$

Where ψ is the wave function. It describes the position of the electron. To get the probability to find the electron in a position, we just need to calculate the expectation value of this wave function at a given time. The above equation describes the evolution of this wave function. $V(t)$ is the electrical potential and it comes from the laser field oscillations. One can solve the Schrödinger equation in order to study electron trajectories for instance or recombination probabilities for harmonics generation.

The quantum-mechanical description predict the same results as the classical model. First, odd multiples of the fundamental frequency are produced. However, the maximal energy achievable is somewhat different:

$$E_{harm}^{max} = \alpha I_\mathrm{P} + 3.17 U_\mathrm{P} \tag{2.21}$$

Where $\alpha = 1.32$. It is larger than the value obtained with the classical model because the quantum calculations involve wave-packet spreading (spatial extension of the wave function).

2.4 Attosecond pulses

The attosecond pulses issued from the generation of high-order harmonics are released under the form of pulse trains (Attosecond Pulse Train APT). Indeed, harmonics are radiated every half-cycle of the driven laser pulse, so radiation appears under the form of *bursts*.

However, for some experiments it might be interesting to isolate one Single Attosecond Pulse (SAP) in order to gain a very good temporal resolution. One way to generate SAP is to use the technique of polarization gating [23]. Usually, an incident linearly polarized laser field is used to generate high harmonics. But the polarization of this incoming field can be modulated, for instance making it elliptical for a certain amount of time and then suddenly linearly polarized again. This means that when the polarization is elliptical, there will be no generation of high harmonics. Thus, the generation of harmonics is restrained to a specific moment in time, lasting less than a full optical cycle, where the polarization turns back to linear. Then a SAP is achieved instead of a burst.

An alternative approach is the use of ultrashort laser pulses which present only one cycle leading to the production of one high-harmonic burst. In order to implement this technique, pulses of the order of 5fs are needed and they must undergo stabilized CEP (carrier envelope phase) to control over the chirp and allow to keep the pulse waveform quite stable along the propagation.

2.5 HHG configuration

In the lab, the generation configuration which is chosen is a loose focusing geometry in a gas cell in form of a capillary. This allows a longer interaction length with the nonlinear medium, that is to say the gas filling the cell.

Phase-matching

It is important to get a good phase-matching because we need the highest high-harmonic output as possible and enhancing phase-matching is a way to increase the conversion efficiency.

Each half-cycle there is a recombination of electrons and thus generation of harmonics (each half-cycle). Then, in order to enhance the harmonic output, the different productions of harmonics must interfere constructively, that is to say the harmonic radiations must have the same phase at a given production location.

On fig. 2.6, the laser beam propagates at the fundamental frequency ω and at each point P high-harmonics are generated. Here the example of the 4^{th} harmonic is taken, which has the frequency 4ω. The harmonics, once generated, are propagating collinearly with the incident beam. In case of perfect phase-matching, the generated harmonics are in phase at each point P and they interfere constructively. This way, the amplitudes add up and the harmonic beam is enhanced. However, this is an ideal case and in reality,it exists dispersion mechanisms due to the fact that the fundamental beam and the harmonics are going through a medium with different refractive index.

Let's define ω being the frequency for the fundamental beam and n the refractive index it sees in the gas medium. The harmonic considered propagates at frequency

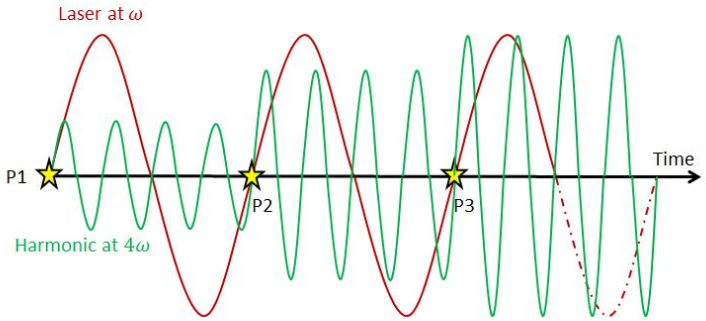

Figure 2.6: This sketch shows the importance of phase-matching in order to get higher harmonic output.

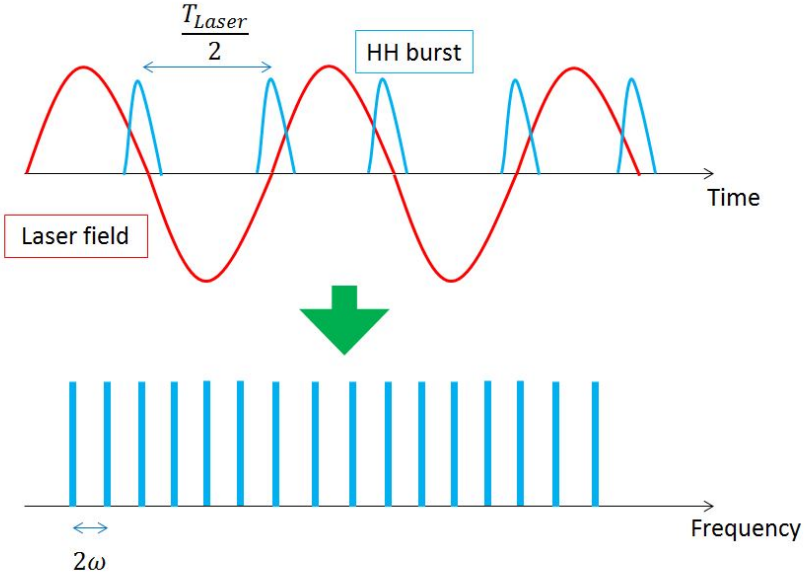

Figure 2.7: This sketch shows where the high-harmonic bursts are generated and the direct link to the spectrum obtained with the spacing parameter.

ω_{harm} and sees a refractive index n_{harm}. The order of the considered harmonic is called q. The following relationships is then deduced:

$$\omega = q \cdot \omega_{\text{harm}} \tag{2.22}$$

$$\lambda = \frac{2\pi c}{\omega_0 n} \tag{2.23}$$

$$\lambda_{\text{harm}} = \frac{2\pi c}{\omega_{\text{harm}} n_{\text{harm}}} = \frac{2\pi c}{q\omega_0 n_{\text{harm}}} \tag{2.24}$$

Where ω_0 is the frequency in vacuum. One has $n \neq n_{\text{harm}}$ so wavelengths cannot be equalized and thus:

$$\frac{\lambda}{\lambda_{\text{harm}}} = \frac{q n_{\text{harm}}}{n} \tag{2.25}$$

This means that harmonics are not really in phase at each point P of the sketch above, so the harmonics generated at different locations will interfere destructively. One solution to this problem is to guarantee phase-matching, for at least a certain distance in the medium, allowing the amplitudes of the harmonics to add up. To do that it is necessary to have the same refractive indexes for both the fundamental laser beam and the harmonics.

That is why the coherence length is defined, that is to say the distance in the medium which separates two source points of the medium emitting harmonics with a phase-shift of π. At this point the harmonics are completely out of phase and they interfere destructively, reducing the output intensity. Thus, the aim is to get the longest coherence length as possible. The coherence length can be expressed as follows:

$$\Delta\phi = \pi \tag{2.26}$$

$$\Delta\phi = \Delta k L_{\text{coh}} = \pi \tag{2.27}$$

That is to say:

$$L_{\text{coh}} = \frac{\pi}{\Delta k} \tag{2.28}$$

Where Δk is the difference in wave vector (wave-number) for the considered conversion scheme, that is to say between the fundamental beam and the q^{th} harmonic.

The efficiency, and then the phase-matching process, is even lower when we want to generate harmonics of higher energies (lower wavelengths) because we inject higher intensities to get a lower cut-off frequency. The drawback of this increase in energy is that the medium gets even more ionized and the refractive index which is seen by the harmonics is even more degraded from the one that the fundamental

sees due to a bigger contribution of free electrons (which are then in higher quantity in the medium). This leads to a stronger phase-mismatch and then a shorter coherence length, reducing drastically the HHG process.

Due to the high intensities at stake in the high-harmonic generation process, it is also important to take into considerations the behavior of the refractive index of the gas media as a function of the laser intensity.

$$n(I) = n_0 + n_2 \times I \tag{2.29}$$

Where n_0 is the fundamental refractive index of the material and $n_2 \times I$ is the effective nonlinear index of refraction due to the intensity I.

Another important parameter is the distance of the medium l_{med}. One can show that the number of harmonic photons emitted is of the following form:

$$N_{\text{ph}} \propto {l_{\text{med}}}^2 \cdot sinc^2(\Delta k \frac{l_{\text{med}}}{2}) \tag{2.30}$$

$$\propto {l_{\text{med}}}^2 \cdot sinc^2(\frac{\pi l_{\text{med}}}{2 l_{\text{coh}}}) \tag{2.31}$$

In the case where $l_{\text{med}} \leq l_{\text{coh}}$ then one can witness generation of harmonics. However if l_{med} becomes higher than the coherence length then each points separated by l_{coh} annihilate each other and starting from a distance of two times the coherence length, the output signal becomes zero. So when there is no absorption and perfect phase-matching (ideal case where $l_{\text{med}} \ll l_{\text{coh}}$), the $sinc^2$ in the above equation tends to be 1 and the number of harmonic photons at the output is proportional to the length of the medium squared.
Nevertheless, one may also pay attention to another important parameter which is the absorption length that is to say the distance an harmonic photon can travel before being absorbed.

Focusing geometry

Between the fundamental beam and the harmonics, the phase difference can be expressed as:

$$\phi(z) = (k_{harm} - qk_0) \cdot z - \phi_{at} \tag{2.32}$$

Where ϕ_{at} is the atomic phase, q is the harmonic order and k_0 is the wave vector of the fundamental beam. The wave vector mismatch is then the gradient of the phase:

$$\delta k = k_k - qk_0 - \nabla \phi_{at} \tag{2.33}$$

The wave vector k_0 can have different impacts especially concerning the focusing geometry. This leads to a particular phase term called Gouy phase.

Due to the high laser intensities which are needed for the generation of harmonics, the medium (gas cell) is located near the focal plane. When the beam passes through the focus, it phase changes by π because the converging beam becomes a diverging beam (geometry variation changes in sign).
To this change, the beam also acquires a propagation phase over the Rayleigh range. This phase is called the Gouy phase and can be expressed as:

$$\psi(z) = arctan\left(\frac{z}{z_R}\right) \tag{2.34}$$

Where z_R is the Rayleigh range. Then, the actual modification in terms of wave vector is the following:

$$\delta k_{Gouy} = \frac{d}{dz}\left(-arctan\left(\frac{z}{z_R}\right)\right) \tag{2.35}$$

$$= -\frac{\frac{1}{z_R}}{1+\frac{z^2}{z_R^2}} \tag{2.36}$$

This term is always negative and is maximal at the focus position. However, by increasing the Rayleigh range (longer focal length for the focusing optics, that is to say loose focusing), it is possible to reduce considerably this phase term. This is why our setup involves a loose focusing configuration in the gas cell. The Rayleigh range is then longer and the interaction length with the nonlinear medium is longer.

Chapter 3

Drive laser system

The aim of this chapter is to describe the whole laser driving system which we use in the lab. We will also describe the underlying principle which enables us to generate such short pulses with such high intensities: *Chirped Pulse Amplification*.

3.1 Properties of ultrashort light pulses

Femtosecond light pulses in the range of 10fs and below are generated by laser systems such as oscillators. It allows to use the pump probe technique on fast events such as the motion of electrons or molecules. What is more, another unique feature of ultrashort light pulses is that they concentrate a modest amount of energy (typically mJ) in focused femtosecond durations, thus allowing very high peak intensities (of the order of 10^{14} W.cm^{-2}) able to transform matter into plasma at the focal spot of the beam.

The expression of the electric field of an ultrashort light pulse can be expressed as:

$$E(t) = E_0 \exp\left(-\frac{t^2}{\tau^2}\right) \exp\left(\mathrm{i}\omega t\right) \tag{3.1}$$

Thus the corresponding intensity becomes:

$$I(t) = |E(t)|^2 = E_0^2 \exp\left(-\frac{2t^2}{\tau^2}\right) \tag{3.2}$$

Where this time we note τ the pulse duration. One can relate this light pulse duration to the FWHM thanks to the following formula:

$$\tau = \frac{FWHM}{2\ln 2} \tag{3.3}$$

The amount of energy contained in a pulse can be linked to the intensity measured at the focus, knowing the transverse profile of our beam, that is to say the beam waist w_0:

$$Energy = I \cdot \tau \cdot \pi {w_0}^2 \tag{3.4}$$

To the previous description of the electric field Gausssian envelop of our ultrashort light pulse, it is necessary to add the fast oscillations of the electric field. Those oscillations can have a constant frequency but it can also depend on time ($\omega(t)$). In this last case, a chirped light pulse is obtained.

$$E(t) = E_0 \cdot \exp\left(-\frac{t^2}{\tau^2}\right) \cdot \exp\left(\mathrm{i}\omega(t) \cdot t\right) \tag{3.5}$$

$$\omega(t) = \omega_0 + \beta_1 t + \beta_2 t^2 + ... \tag{3.6}$$

The different β coefficients describe the order of the chirp. For positive β, the chirp is also positive, as in fig. 2.3. This means that the trailing edge of the chirped pulse will have a higher frequency than the leading edge, so it will be blue-shifted. This is the contrary for negative β.

Only unchirped pulses are Fourier transform limited (pulse duration minimized). Those type of pulses are desired to get high-intensity pulses. However, it is difficult to maintain this limit as the pulses propagate because they may face dispersive optical elements (windows, lenses...) and thus get chirped. That is why the number of dispersive optics tends to be reduced in the setup and the use of reflective optics instead of transmitting optics is recomended. And finally, it is still possible to compensate introduced chirp by adding optics with dispersion of opposite sign.

Another important aspect of light pulses of great interest for high-harmonic generation is the bandwidth of the laser pulses produced by the oscillator and generally by the whole laser-driven system. Indeed, the pulses are not monochromatic light, meaning that their spectrum contains several frequencies. This bandwidth will affect the spectrum of the high-order harmonics we will generate. The spectra of the different harmonic lines are determined by the spectrum width of the laser pulse because harmonics simply result in the generation of frequency multiple of every frequency present in the spectrum of the incident light pulse.

3.2 Chirped pulse amplification

In order to generate high-order harmonics, high intensities within ultrashort pulses are needed, of the order of magnitude of $10^{14} W.cm^{-2}$. Those intensities are only achievable by using ultrashort laser beams. However, using directly short pulses in amplifiers can create nonlinear distortion or even worse completely destroy the gain medium of the amplifier. CPA (*Chirped Pulse Amplification*) is a

solution to this problem.

The principle is that the pulses are first chirped and expanded temporally before entering the amplifier(s) by a factor 1000 to 10 000 in order to safely amplify the pulses in crystals. This stretching is done thanks to dispersive optical elements, mainly gratings. The stretching produces chirped pulses. The advantage is that it reduced the peak power of the incoming pulse, such that intensities are below the damage threshold of the crystal of the amplifier. After all the amplification stages, the pulse is time-shortened again to a duration closer to the one of the input pulse thanks to a compression stage and the final pulse is free of chirp. Then a very high peak power is reached and one has to be sure that the beam size is big enough in the compressor in order not to damage the optical components.

The following drawing summarizes the different steps of the CPA method:

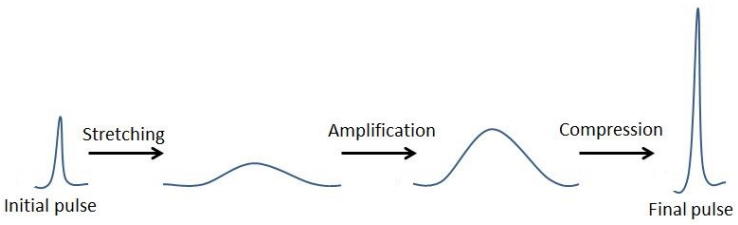

Figure 3.1: This sketch explains the different steps of the *Chirped Pulse Amplification* technique.

Basically, in the lab the CPA method allows to generate femtosecond pulses with several mJ of energy at the output of the compressor. This means that peak powers of the order of hundreds of GW and even 1TW can be achieved.

The laser system was designed by the company AMPLITUDE TECHNOLOGIES [8]. It consists of a full integrated Ti:Sa oscillator with its DPSS (diode Pumped Solid State) pump laser, a stretcher, a regenerative amplifier and two multipass amplifiers for each beam-line all pumped by six DPSS laser system at 100Hz designed by QUANTEL (Centurion model). The last amplifier used on the beam line is pumped by a LITRON laser delivering 100mJ pumped by flash lamps.

Stretching or compression are usually achieved thanks to dispersive elements such as gratings or prisms. The principle is that different optical paths are needed for the different wavelengths of the spectrum of the initial pulse.
A typical stretcher design uses two gratings and a telescope system as shown below:

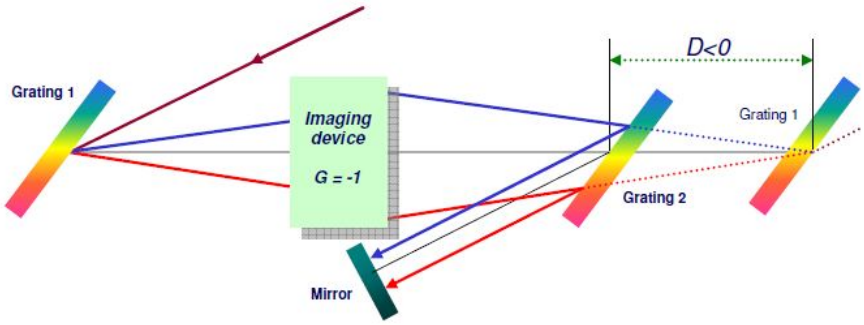

Figure 3.2: This sketch shows the typical design of a stretcher (Öffner triplet). The stretching factor depends on the distance D between the two gratings.

On this previous sketch, one notices that the optical path for shorter wavelengths is longer than the one for longer wavelengths. This means that shorter wavelengths take more time to travel through the entire system than the longer wavelengths.Thus, the blue part (trailing edge of the pulse) of the spectrum is delayed compared to the red part (leading edge of the pulse) so at the output of the stretcher, the pulse is then stretched and looks like a rainbow (temporally).
The stretching factor can be tuned thanks to several parameters. First it depends on the the width of the spectrum of the initial pulse: the wider the input spectrum is, the longer the stretched pulse is. Then, it depends also on inner parameters of the stretcher set-up. For instance, one can play on the grooves density of the gratings, the distance D between the gratings or even the number of round trips in the stretcher.

The stretched pulse is then sent to different amplification stages: a regenerative amplifier and then two 4-pass amplifiers for each beam-line. After amplification, the pulse must return to its initial duration, so it needs to be compressed. The compression stage uses a set-up similar to the one of the stretcher, involving a dispersive system. The compressor must be able to exactly compensate the stretching (and any additional dispersion introduced by the optics of the amplification stages) that is why the alignment of a compressor can be very critical (especially the incident angle). An example of typical compression set-up is presented below [24]:

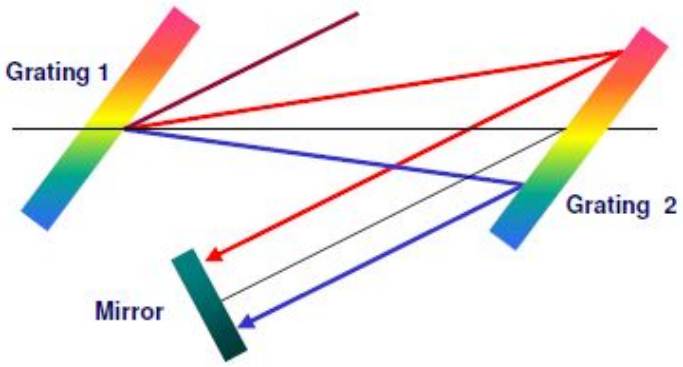

Figure 3.3: This sketch shows the typical design of a compressor.

3.3 Overall laser system

Based on CPA technique, the overall laser system can be described thanks to the following sketch:

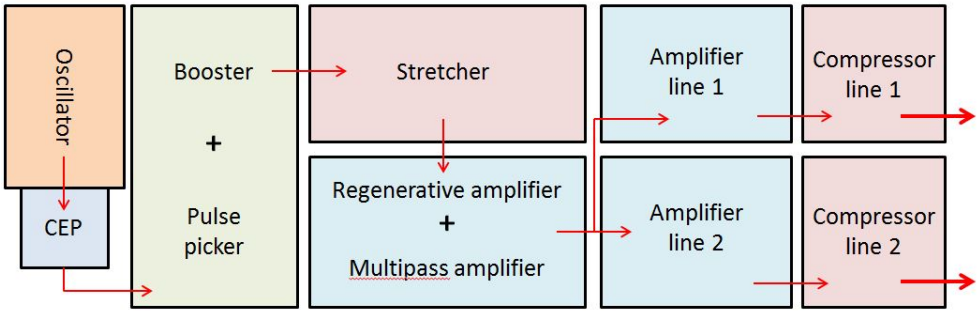

Figure 3.4: This sketch shows the different parts of the laser driving system. It also shows that we have two output lines.

One of the output line is used for the HHG line directly (line 1), the other beamline goes through a TOPAS stage (traveling wave three amplification stages white light seeded OPA) and can be used for two-colors experiments.

Femtosecond pulses are generated at 800nm with a Ti:Sa oscillator. The output of this oscillator is mode-locked and goes through a Carrier Envelop Phase (CEP) controller. Then the beam is sent to a pre-amplification stage (booster). We want

to generate femtosecond pulses at a repetition rate of 100Hz. However, the ultra-short pulses generated by the mode-locked oscillator are in a form of a pulse train with a frequency of around 83MHz. So it is necessary to pick certain pulses from the pulse train and this is done by using a pulse picker, which is an optical switch electronically controlled (Pockels cell).

After those stages, CPA process begins [24]. The pulses are going through the stretcher where they are expanded in time. Then they are first amplified by the regenerative amplifier and after by another multi-pass amplifier. The beamline is then separated in two and each new beamline is being amplified again before compression.

In the next sections, the different parts of the laser system are described with more details as well as the optional devices which were added to the system to help shaping the pulses.

3.4 Description of the different elements

For the description of the different stages of the laser system, let's refer to the above sketch of the overall set-up.
The front-end of the laser system is detailed first.

Oscillator

The Ti:Sa oscillator (see Appendix A for absorption and emission spectra) is from the company FEMTOLASERS (Rainbow oscillator). It is pumped by a COHERENT Verdi V6 compact DPSS laser suited for Ti:Sa pumping (12 to 18W). It enables the lowest CW noise at 532nm and it is suitable for single frequency applications.

This oscillator is mode-locked through Kerr-lens mode-locking process (see Appendix B for more details).

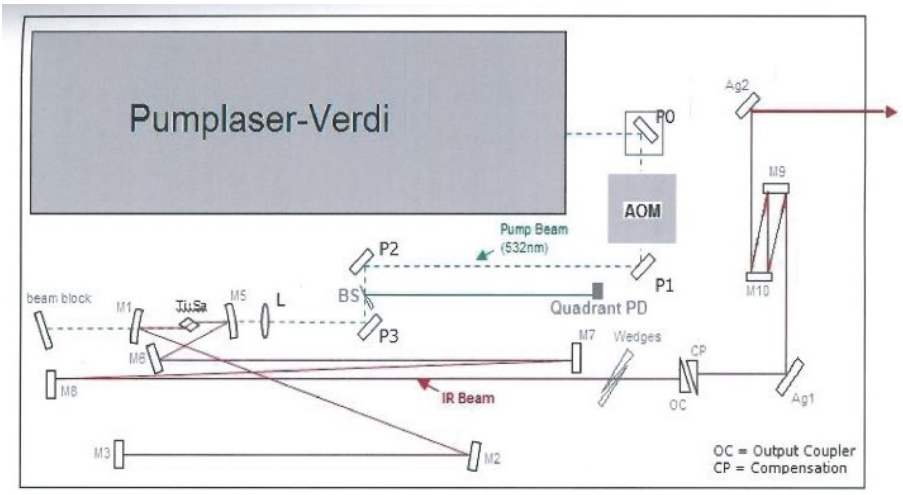

Figure 3.5: This picture represents the oscillator pump and the oscillator box. Sketch taken from [8].

CEP controller

Theoretically, a pulse can be described as an envelope superimposed on a carrier wave. However, there can be a phase-shift between the peak of the envelope and the maximum of the carrier as it propagates. This is due to the fact that, in general, the group velocity and the phase velocity are not exactly the same so this varying phase-shift appears as the pulse propagates, for instance inside a cavity. This can be a drawback because then the successive pulses generated by a mode-locked laser cavity (here the oscillator) are slightly different from one another.
A CEP (carrier Envelope Phase) allows us to lock the group and phase velocity inside a given laser cavity. This is very important when working with really short pulses with for instance 5 cycles (around 10fs of pulse duration).

Booster

The contrast ratio booster device is used to correctly inject the seeding pulses in the regenerative amplifier. Basically, it consists in a compact multi-pass amplifier used to enhance the direct output of the oscillator to the μJ level. In the same stage, a saturable absorber is also found and is used to *clean* the pulses by removing all the residual ASE (Amplified Spontaneous Emission) of the oscillator. This is also the stage where we select pulses so that the repetition rate becomes 100Hz and no longer tens of MHz. This device increases the contrast ratio from 10^{-4} to 10^{-6}.

Pulse picker

With the contrast ratio booster, there is also a pulse picker which allows to pick certain pulses and block the others in order to satisfy the repetition rate we want for the laser system. It consists of an electro-optic modulator (Pockels cell and polarizing optics). The Pockels cell manipulate the polarization state and the polarizer transmits or blocks the pulses depending on the polarization. The required speed of the modulator switching on and off is determined by the repetition rate of the laser system. This pulse picker is used for injection later on in the regenerative amplifier.

Stretcher

As said previously, the stretcher is based on dispersive optics. Here it is an all-reflective Öffner triplet combination composed of two spherical concentric mirrors (first one is concave and second convex). The system is completely symmetric so only spherical aberration or astigmatism are present (no coma on axes or chromatic aberration because of all the mirror components).

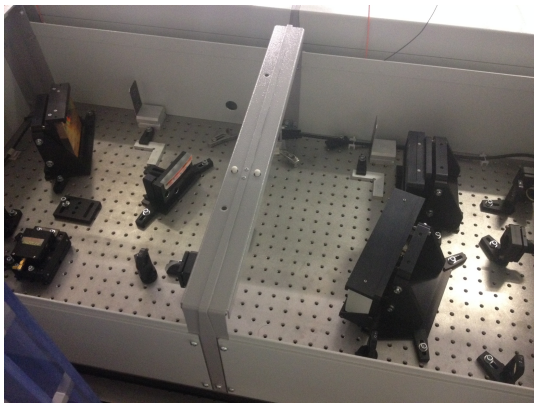

Figure 3.6: This picture represents the stretcher set-up.

Dazzler

In the above picture, on the left side, one can see an additional device called Dazzler. This is an acousto-optic programmable dispersive filter (AOPDF see [9]). This device is designed by the company FASTLITE and can be added right after the stretcher set-up. It acts as a phase modulator which pre-compensates the dispersion and phase distortions introduced along the path in the laser system. It also includes an amplitude modulator to optimize the laser output spectrum but as the the problems of phase and amplitude modulation are decorrelated, one uses the Dazzler for phase control and another device, the Mazzler for the spectrum

optimization. The combination of both devices allows to produce output pulses (after the compression stage) of duration between 20 and 60fs.

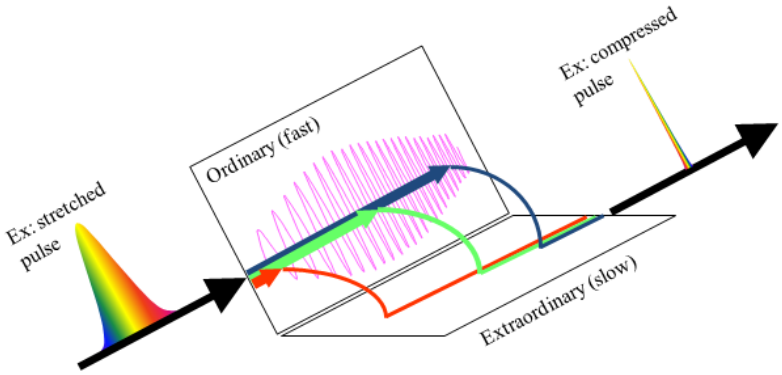

Figure 3.7: This sketch explains how the Dazzler device is working. It relies on a longitudinal interaction between a polychromatic acoustic wave and a polychromatic optical wave in the bulk of a birefringent crystal.

A simple picture to explain the concept of this device would be to consider sum frequency generation between the optical pulse and the acoustic wave. Then, thanks to the acoustic wave for which one can modulate the frequency, the spectrum of the optical pulse can be modified accordingly.

Regenerative amplifier

The regenerative amplifier constitutes the first amplification stage of the CPA process. This is not a stage where the amplification is strong but the important issue with this amplifier is that it keeps the beam quality. Indeed, it uses a TEM_{00} laser resonator and allows to deliver diffraction-limited beams. Then, the additional high-power multi-pass amplifiers on both beam lines only use flat mirrors, thus the beam quality is not affected by the amplification stages.

In the regenerative amplifier cavity, there are two Pockels cells (the gray boxes on the picture below) allowing to either introduce the pulse in the cavity or to escape it and a third Pockels cell is used to optimize the contrast ratio output. One cell allows the seeding pulses to enter the cavity and the other one allows pulses to get out of the cavity when they have reached the maximum energy level.

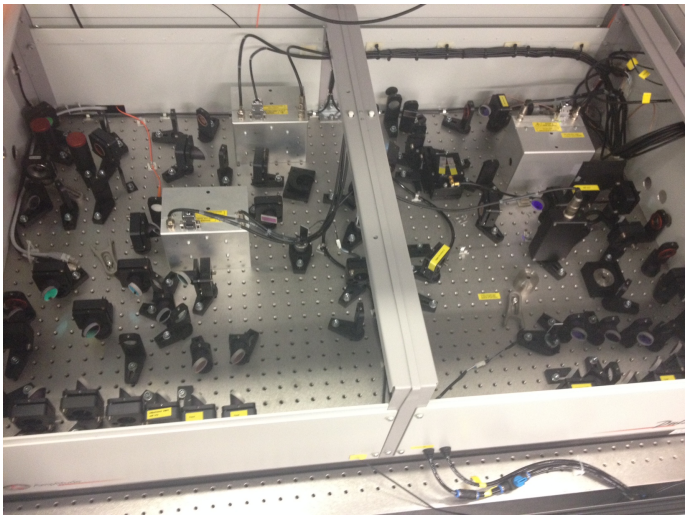

Figure 3.8: This picture represents the set-up of the regenerative amplifier (upper part of the picture) and the first high-power multi-pass amplifier (lower part of the picture).

Mazzler

Inside the regenerative cavity, it is possible to add an additional acousto-optic modulator called Mazzler [10] which works on the same principle as the Dazzler. The Mazzler, or Acousto-Optic Programmable Gain Control Filter (AOPGCF) is a solution to the gain narrowing process which happens in laser amplifiers. Indeed, when a light beam with a given bandwidth (the Ti:Sa beam in our case) is sent to an optical amplifier medium which has a limited gain bandwidth, the bandwidth of our light beam is then reduced, that is to say there is a gain narrowing phenomenon. It translates by the fact that the center region of the spectrum experiences a higher gain than the wings of the spectrum. In mode-locked laser with short pulses this phenomenon tends to increase the pulse duration because it compresses the optical spectrum.

Gain narrowing is particularly important for high-gain amplifiers and also regenerative amplifiers. A solution is to put inside the cavity an optical filter which can compensate the gain narrowing by introducing higher losses for the spectral components of the pulses which experience higher gain.

The Mazzler is a device which can flatten the global amplifier gain in order to enlarge the spectrum (up to 80nm, that is to say down to 20-25fs pulse duration for the output).

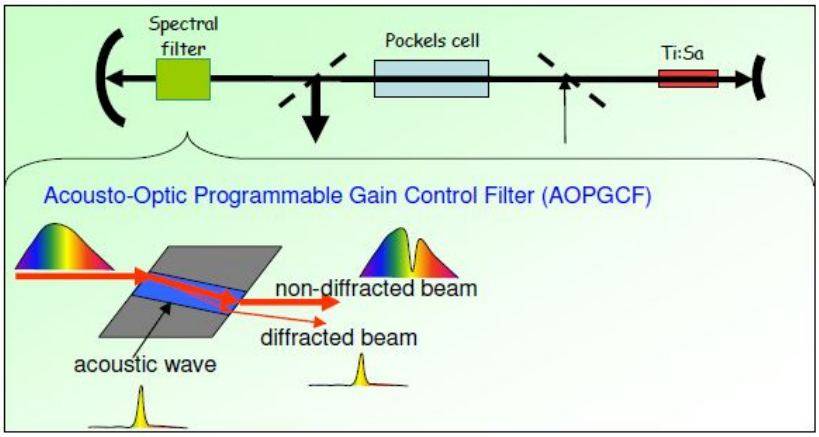

Figure 3.9: This sketch explains how the Mazzler is working inside the regenerative cavity. Similarly to the Dazzler device, the Mazzler uses an acoustic wave to diffract the beam. The unwanted spectral components belong to the diffracted beam and we get rid of this beam. Thus, the non-diffracted beam which stays in the cavity has some holes in its spectrum (where the amplifier gain is the highest). Gain flattening is obtained with this method. For more details see [10].

High-power multi-pass amplifiers

The regenerative amplifier is followed by one high-power multi-pass amplifier pumped by a DPSS laser at 532nm (Centurion by QUANTEL). Then the beam is split into two lines and on the HHG beam line we get another high-power multi-pass amplifier pumped by a 1064nm SHG laser at 532nm (Nano series by LITRON Lasers). All the amplifiers are based on Ti:Sa crystals.

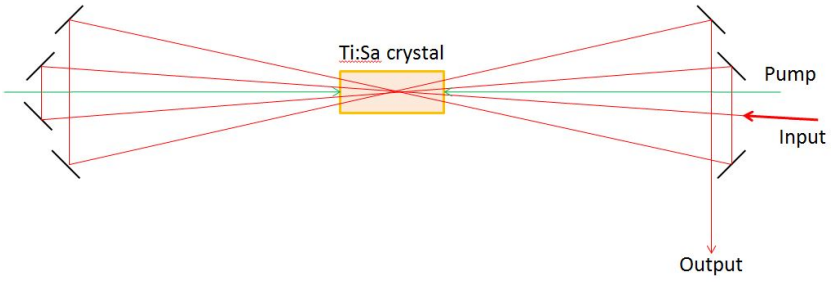

Figure 3.10: This sketch shows the multi-pass amplifier principle.

Compressor

As presented in the previous section the pulses coming from the output of the high-power multi-pass amplifiers are then compressed back to shorter pulse durations thanks to dispersive optics (two gratings).

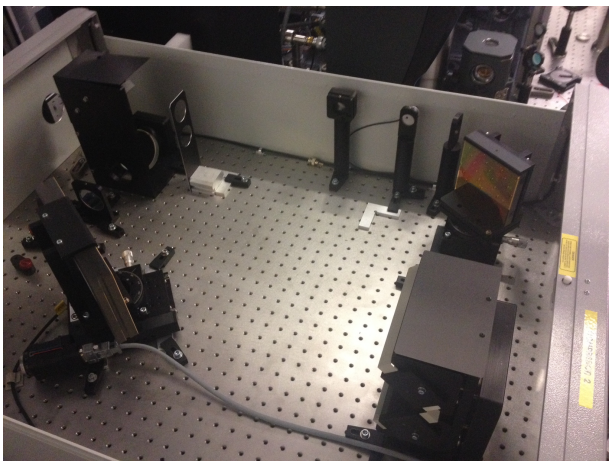

Figure 3.11: This picture shows the compression set-up with the two gratings.

3.5 Performances of the laser system

The range of pulse durations achievable by the laser system is 20 to 60fs, that is to say spectral width of 48 to 16nm (time-bandwidth product for a Gaussian pulse with a central wavelength of around 810nm).
The mode-locked output of the oscillator delivers pulses of duration 4.6fs (Fourier Limit) and spectral width of 168nm.
The output power of the CEP controller is around 180mW. At the end of the regenerative amplifier (number of passes superior to 10 but not fixed, depending on when the pulse reach the needed level of energy), we have an energy of 300μJ. Then, the first multi-pass amplifier (5 passes) gives an output energy of 16 to 18mJ. Finally, the high-power amplifier of the HHG beam line (4 passes) is pumped by 100mJ at 532nm and gives an output energy of around 32mJ at 800-810nm before the compression stage.
After the compressor, the useful output energy for the HHG beam line is 20mJ which is then split into two parts (almost 50-50%). One part is going into the vacuum chamber for generation of harmonics and the other is going to the THz generation stage.
The laser system repetition rate is 100Hz.

3.6 Characterization of the Ti:Sa beam

Spectral measurement

After the first amplification stage, the spectrum of the beam at 800nm was measured, first without any action of the MAZZLER device (natural spectrum) and then with the MAZZLER on in broadband mode. The spectrometer is a fibered OCEAN OPTICS device.

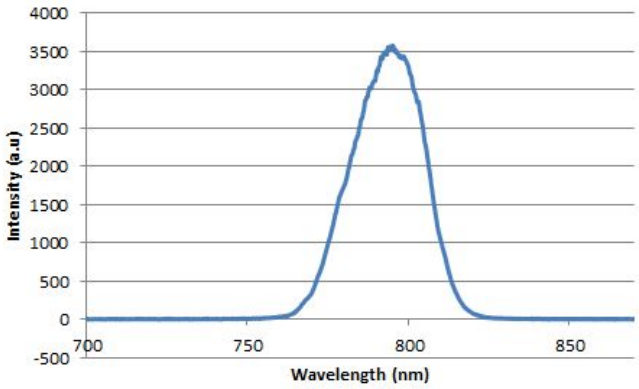

Figure 3.12: This graph show the natural emission spectrum of the beam at 800nm (peak wavelength).

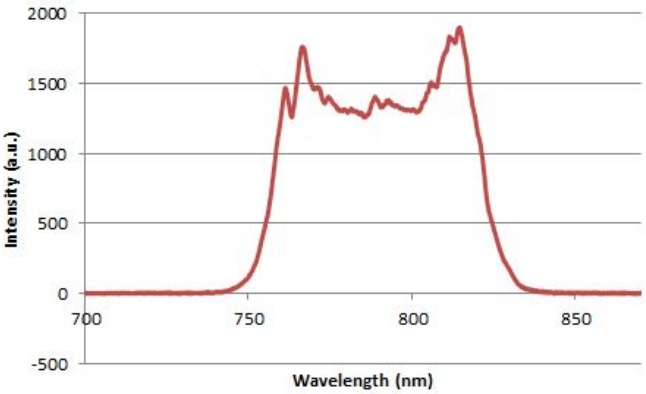

Figure 3.13: This graph show the emission spectrum of the beam at 800nm for a broadband MAZZLER configuration.

Both spectra were measured after the amplifier following the regenerative cavity.

Temporal measurement

In order to measure femtosecond pulse durations, a special device is needed: the WIZZLER which is base on Cross-Polarized Wave Generation.

WIZZLER device

In order to fully characterize the incident laser beam of Ti:Sa [15], a temporal characterization of the pulse sent to the high-harmonic generation chamber is needed. The Mazzler device helps to decide which spectrum is sent. Thus it influences the pulse duration.
The company FASTLITE also designed an interferometric instrument able to measure ultrafast pulses. This device is called Wizzler and is based on Self-Referenced Spectral Interferometry (SRSI).

Figure 3.14: This picture extracted from FASTLITE website shows the Wizzler device.

The principle of the measurement is as follows [14]:

- A replica of the pulse to be measured is created but with perpendicular polarization.
- This replica is slightly delayed.
- The main pulse undergoes Cross-Polarized Wave Generation(XPW) in order to generate a reference pulse which presents a broader spectrum and a flatter phase. However the carrier frequency stays the same.
- This reference pulse is also on the perpendicular polarization compared to the initial pulse.

- This means that a correctly oriented polarizer can transmit only the reference and the replica of the pulse we want to measure.

- Those two signals create an interference pattern which is then recorded by a spectrometer.

- From the analysis of the fringes, one retrieves the spectral phase and amplitude of the pulse, allowing to fully characterize it.

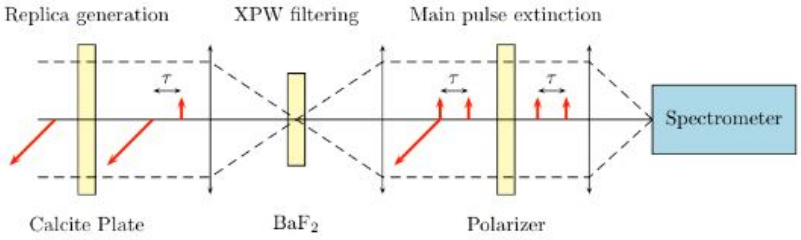

Figure 3.15: This sketch extracted from FASTLITE website shows the different steps of the measurement.

The XPW third-order nonlinear process allows the generation of a linearly polarized wave, perpendicular to the incident one. This can be done with a BaF_2 crystal.
The generated reference pulse is the same as the initial pulse but filtered by the intensity of the initial pulse. So the crystal acts as a temporal filter and shortens the pulse, thus increasing the spectrum [16]:

$$E^{ref}(t) \propto |E^{initial}|^2 \cdot E^{initial}(t) \tag{3.7}$$

Once we get the interference pattern of the two pulses delayed thanks to the spectrometer, Fourier Transform analysis can be applied. the first step consists in acquiring an interferogram:

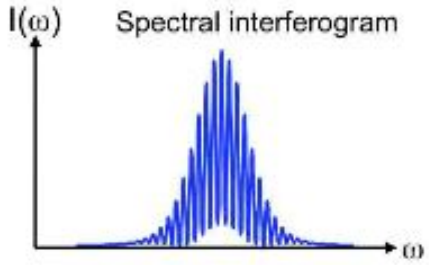

Figure 3.16: This graph shows the interference fringes between the two pulses.

Then, an inverse Fourier Transform is applied and gives a three-peaks pattern. The interesting term, that is to say the one containing the oscillations due to the phase difference between the two pulses is centered at the delay position:

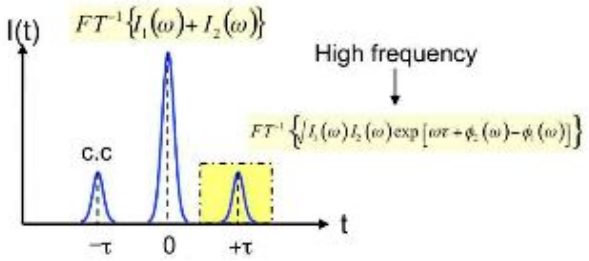

Figure 3.17: This graph shows the different peaks retrieved from the inverse Fourier Transform of the interferogram.

The two other peaks are filtered out in order to keep only the interesting one:

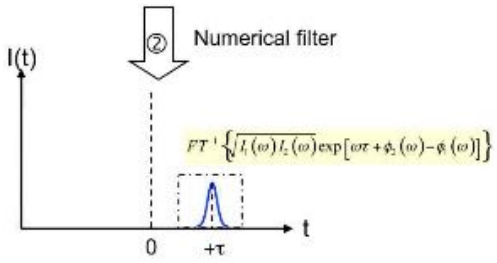

Figure 3.18: This graph shows the filtering of information.

A final Fourier Transform is applied to retrieve the phase difference and the intensity in the spectral domain:

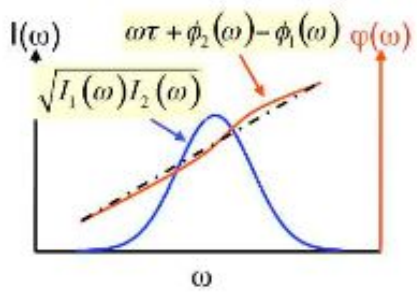

Figure 3.19: This graph shows the final characterization of the pulse with the phase retrieval and the intensity.

The general lay-out of the Wizzler device is the following:

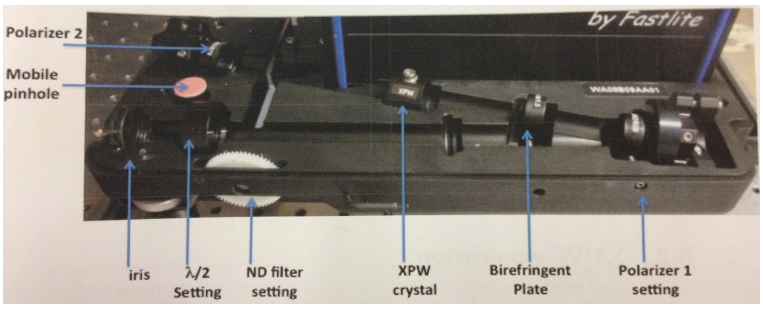

Figure 3.20: This picture shows the different components of the Wizzler device.

Measurements

With the above-mentioned device, pulse durations of FWHM of 59fs were measured.

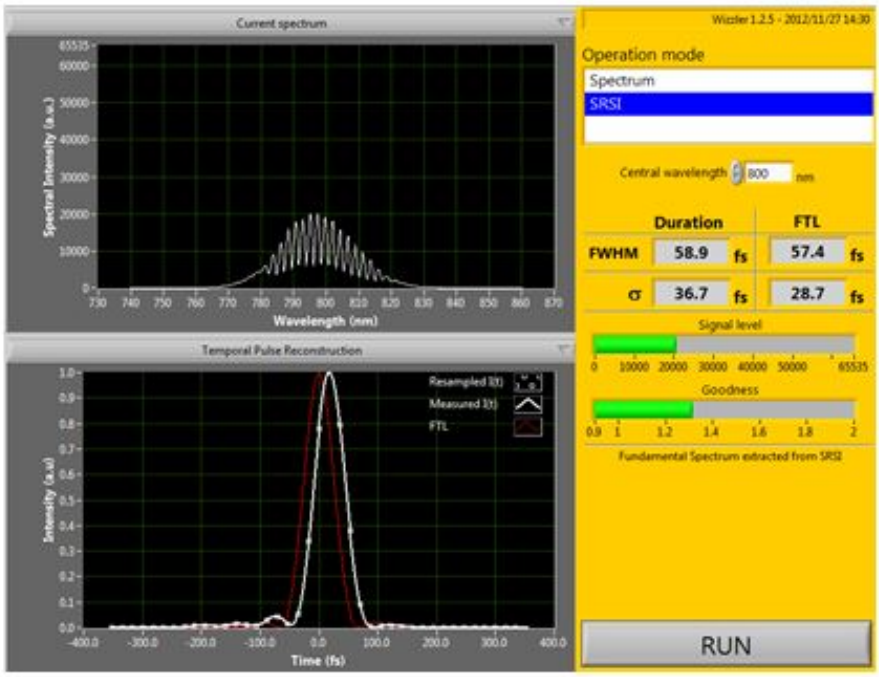

Figure 3.21: This picture shows an example of pulse duration measurement. On the top graph, one can see the interferogram with the fringes and below is the reconstructed pulse.

Thanks to the MAZZLER, the spectrum can be shaped in order to obtain pulse durations in the range 20-60fs.

Beam profile and divergence

One last step to characterize the Ti:Sa beam is to study its beam profile. After a focusing lens, a camera was put (WinCamD by DATA RAY Inc.). The camera has 1.4M pixels (1360×1024) and the pixels are squared, of size $6.45 \times 6.45 \mu m$ for a total sensor area of $8.8 \times 6.6 mm$
The corresponding software (Data Ray) allows to display the beam profile in two dimensions and gives the size of the spot.

Around the focus, the camera was used to scan over 7cm to measure the spot size and then deduce the divergence of the beam, then the data were mirrored in order to get a larger range (14cm).

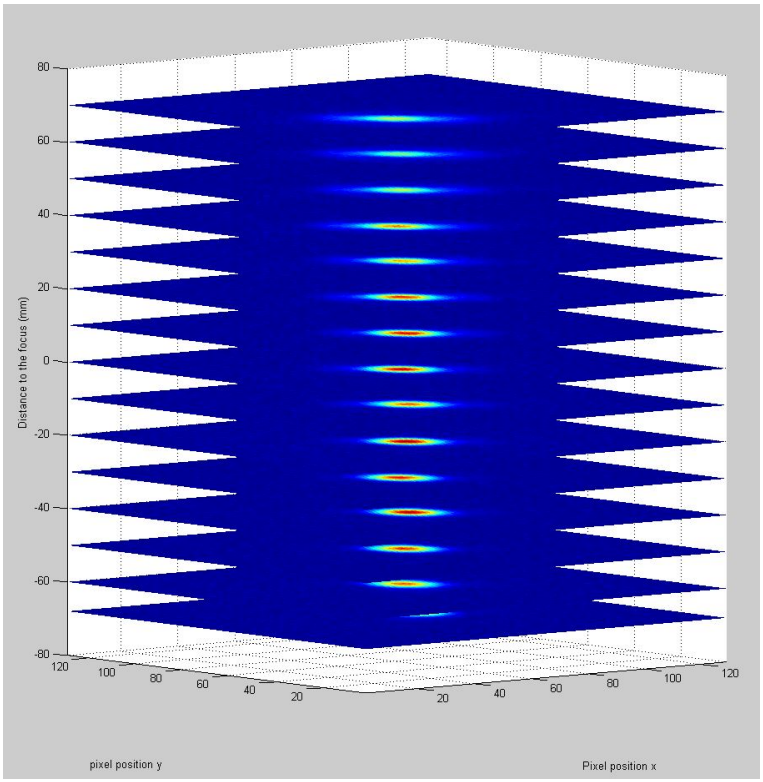

Figure 3.22: These stacked images show the beam profile around the focus.

The divergence of the beam can be characterized by the M^2 parameter which translates the discrepancy between the beam divergence and a normal Gaussian divergence:

$$\theta_{gau} = \frac{\lambda}{\pi w_0} \tag{3.8}$$

Where w_0 is the beam waist (smallest beam size, at focus). If θ is the real divergence angle of our beam, then the M^2 paramter is defined as:

$$M^2 = \frac{\theta}{\theta_{gau}} \tag{3.9}$$

For the Ti:Sa beam, the waist (radius) was measured in the x- and y-directions thanks to a Matlab fitting with the data given by the camera:

$$w_0^x = 85.1\mu m \tag{3.10}$$

$$w_0^y = 92.5\mu m \tag{3.11}$$

The fitting are obtained thanks to the following formula:

$$w^2 = w_0^2 + M^4 \left(\frac{\lambda}{\pi w_0}\right)^2 \times (z - z_0)^2 \tag{3.12}$$

Where w_0 is the size of the waist (radius) of the beam, z_0 is its position.

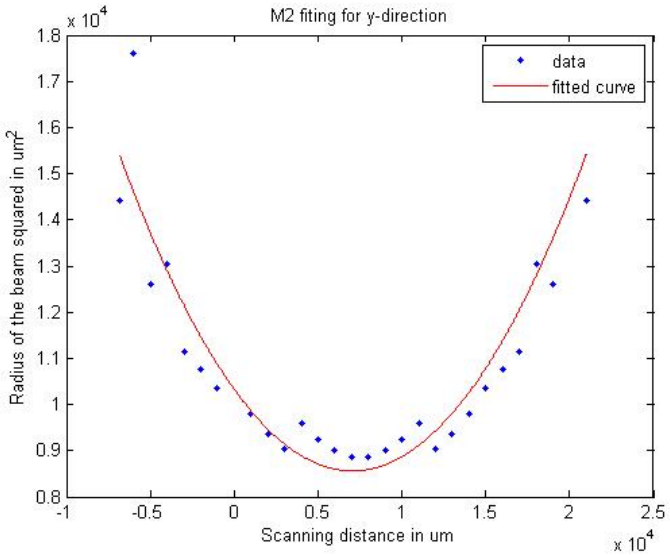

Figure 3.23: This picture shows the fitting for the y-direction of the beam with the above-mentioned formula.

The M^2 value in the y-direction gives:

$$M_y^2 = 2.1 \tag{3.13}$$

In the x-direction, the results given by the Matlab fitting falls just under 1 (0.9). This might be due to the fitting error and most likely to the quality of the measurement. A maximal limit for this parameter can only be obtained by considering the waist size (which is determined) and retrieve the beam size on the lens used to focus the beam 3m before the camera. This beam size is of 1cm (in radius). We have the following relationship:

$$W^2 = \frac{M^2 \lambda f}{\pi w_0} \tag{3.14}$$

A W waist of 1cm is obtained for M between 1.1 and 1.2, giving thus the upper limit for the M^2 parameter in the x-direction.

The Rayleigh range can also be calculated for a waist size of $85\mu m$:

$$Z_R = \frac{\pi \left(w_0\right)^2}{\lambda} = 28mm \tag{3.15}$$

Chapter 4

Experimental set-up

After the compression stage of the drive laser system, a 20mJ beam line at 800nm is split into two beams. One beam is dedicated to the high-harmonic generation and the other one is used to generated either THz beam for streaking or simply to shape the 800nm beam to do RABBIT measurements. The aim of this chapter is to describe the different parts of the set-up.

4.1 HHG beam line

First, the generation set-up which involves vacuum chambers is detailed with a generation stage, a focusing stage and experimental chambers.

Overview of the vacuum line

The whole vacuum line is around 12m long and has 8 chambers including the one used for streaking measurements.
Once the output of the compression stage is split into two beams, one part is entering the vacuum line through a 3m-focusing lens. At the focus, the generation stage is found which is a hollow waveguide (gas cell). The alignment is done thanks to several gold mirrors in the first two chambers. After the generation stage, there is a chamber with different pinholes which can be used for alignment.
The high-harmonics produced in the hollow waveguide are then focused thanks to a flat mirror-toroidal mirror combination up to the diagnosis and the streaking chambers.

All the chambers are pumped by turbo pumps to reach high vacuum in the experimental chambers (diagnosis chambers) that is to say a vacuum of the order of 10^{-7}mbar and 10^{-4}mbar in the first alignment chambers and generation chamber due to the gas we inject in the cell.

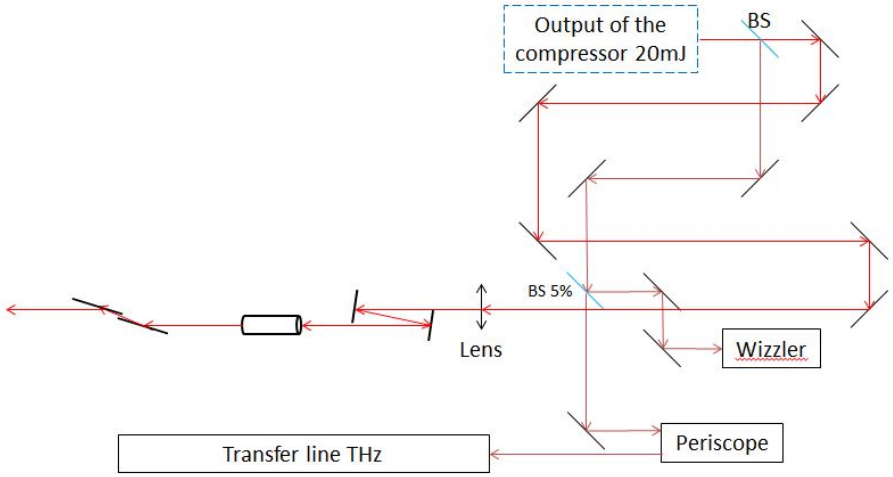

Figure 4.1: This sketch represents the lay-out of the experimental set-up from the output of the compressor.

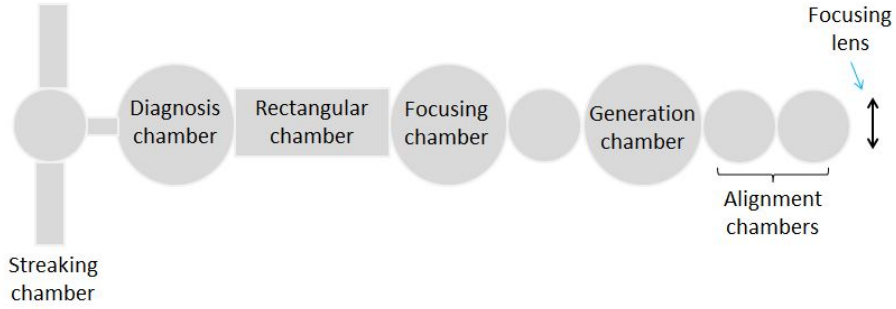

Figure 4.2: This sketch represents an overview of the vacuum line and the function of the different chambers.

HHG generation

In order to generate high-harmonics the beam of the Ti:Sa needs to be focused in the hollow waveguide (generation stage). To have a good coupling, it is also important that the length of the cell is inside the Rayleigh range. This is why the focus of the beam is done with a lens of long focal length: 3m.

However, due to this long focal length, some alignment tricks need to be performed inside the chambers because the entrance of the vacuum line is not really located 3m before the generation stage: it is closer. One idea thus would be to place the lens far away from the entrance window of the vacuum line but this would mean that the beam size of the Ti:Sa would already be quite small while impacting the entrance window. This is not good at all because such small beam sizes at such energies (10mJ) could induce nonlinear effects and beam distortions non suitable for the measurements.
This is why the lens is placed directly before the entrance window and build a kind of delay line inside the first two chambers thanks to two mirrors in order to get the focus in the right place in the generation chamber. Moreover, this trick enables to align more easily the beam inside the chambers.

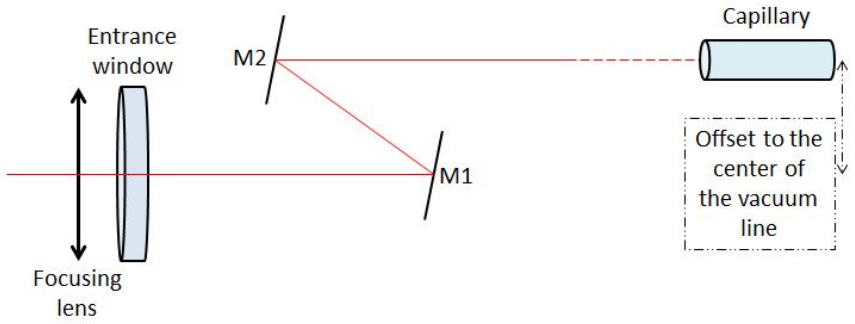

Figure 4.3: This sketch shows how the beam is focused into the hollow waveguide. The alignment mirrors are used at almost 0 degrees. The angle here are exaggerated.

As seen on the previous sketch, the final beam is not in the center of the chamber, there is an offset which can be later on compensated by mirrors (toroidal mirror combination). But one drawback is that a lens is used, which can introduce chromatic aberration so that the different colors are not focused at the same spot in the capillary. In chapter 6, which deals with HHG beam line optimization, another focusing scheme is implemented in order to solve this problem.

Gas cells with different lengths and geometries are used. For instance, cells of 6cm- or 2cm-length with the following shape can be installed on the generation stage. The use of gas cells of the type of waveguide could be an improvement of the generation set-up because the phase-matching could be enhanced by the wave-guiding properties of the cell.

Figure 4.4: Hollow waveguide with special inside geometry.

The cells are drilled on top in order to inject the gas. There is a valve which can be remotely controlled so that to chose the opening time of the valve, the delay between the different gas pulses and the differential pressure we want to have.

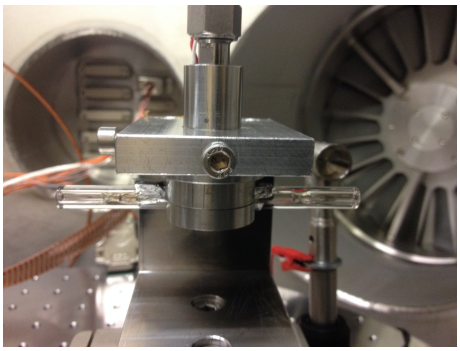

Figure 4.5: Picture of the 6cm-long cell on its stage inside the generation chamber.

Focusing set-up

After the generation stage (hollow waveguide), both the fundamental beam at 800nm and the high-harmonics are propagating together along the vacuum line. For some measurements (streaking or RABBIT for instance), the beam needs to be focused in the streaking chamber. In order to do that, the combination of two mirrors is used. One is a long flat mirror made of fused silica which reflects the high-harmonics radiation and absorbs a substantial amount of the 800nm. But there is no special coating. This mirror is at 2 degrees from the initial beam and then deflects the beam by 4 degrees (we will see later that this 4 degrees-deflection has a special purpose: aiming at the vacuum spectrometer arm). It is combined to a toroidal mirror which focuses the beam down to the last chamber. The toroidal mirror is a cylindrical gold mirror and is angled so that to correct the beam trajectory imposed by the first mirror.

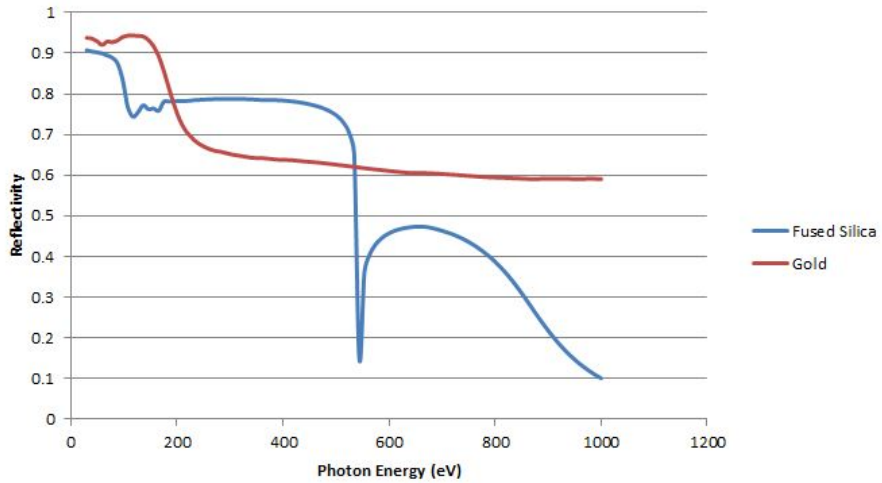

Figure 4.6: These curves show the reflectivity of fused silica and gold for a thick mirror at 2 degree incidence as in our set-up.

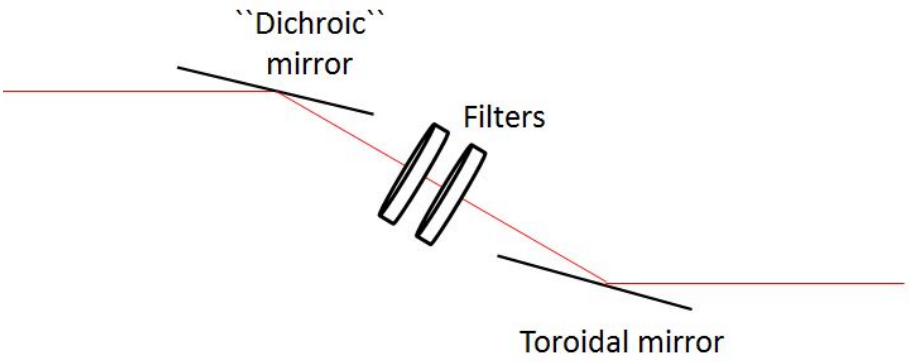

Figure 4.7: Sketch of the two-mirrors combination for focusing. The angles are exaggerated.

In case the 800nm needs to be completely blocked, for instance to study the beam profile of high-harmonics on a camera chip, there are filters (aluminum, zirconium) at our disposal in the focusing chamber.

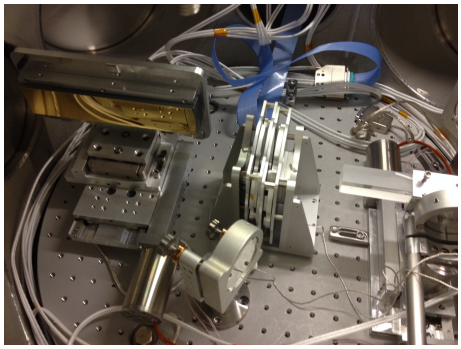

Figure 4.8: Picture of the two mirrors as well as the filters. The picture is the reversed of the above sketch: there is first the toroidal mirror on the left side, then the filters and finally the "dichroic" on the right side of the picture.

Spectrometer

As mentioned previously, one of the chamber (the rectangular one) includes a vacuum spectrometer (see chapter 5). The design of this chamber is such that if we remove the above mentioned toroidal mirror, the beam ends in the spectrometer (due to the 4 degrees deflection of the glass plate).

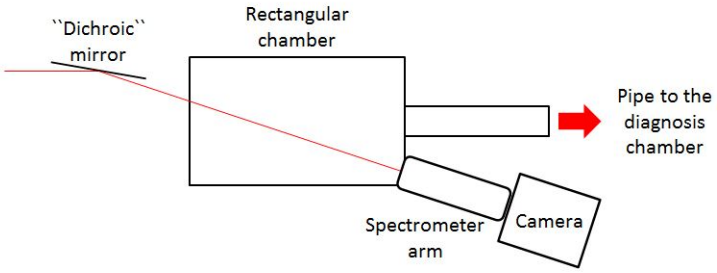

Figure 4.9: This sketch shows how the beam is directed to the spectrometer arm through the rectangular vacuum chamber.

For more details about the spectrometer, see chapter 5.

Diagnosis chamber

Before the streaking chamber, some diagnosis can be handled thanks to a vacuum CCD camera and a transmission grating. Both are on motorized stages and

can be controlled remotely. The camera is a x-ray camera from PRINCETON INSTRUMENTS (PI-MTE series).

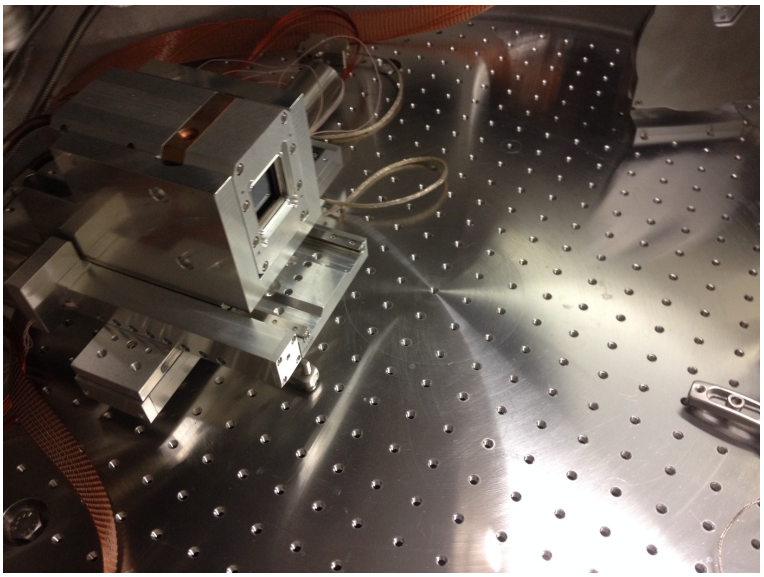

Figure 4.10: Picture of the PRINCETON vacuum camera.

This camera is very sensitive so one must take care to put aluminum filters in order to suppress the 800nm radiation before shining on the CCD. It is dedicated to soft x-ray imaging (30eV to tens of keV). It has 2048×2048 pixels for a total chip area of $27.6mm \times 27.6mm$. The camera can be cooled down to reduce the noise. The camera can be moved away from the center of the chamber to let the high-harmonic beam go through to the streaking chamber (see later in this chapter).

4.2 THz beam line

As mentioned above, the 20mJ output of the compressor is split into two lines. One is going to the vacuum chambers for HHG and the other one is used mainly for THz generation. THz beam is needed for streaking experiments in order to characterize the XUV pulses in spectral and temporal domains (see chapter 7).

This line is constituted first by a transfer line in low vacuum traveling parallel to the vacuum chambers of the HHG beam line.

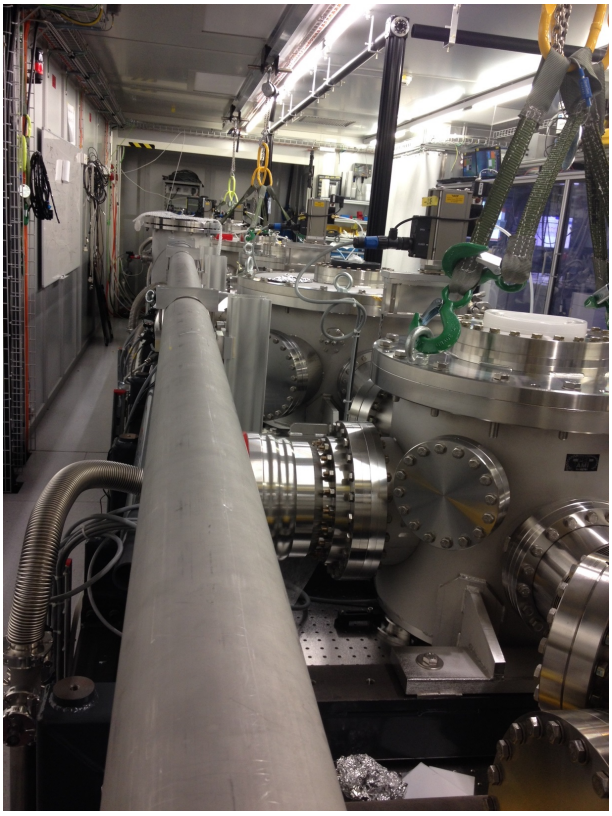

Figure 4.11: Picture of the transfer line for the THz generation stage.

On one side of the streaking chamber, there is an entrance window for the streaking field (THz). THz field is generated from the IR beam (Ti:Sa) thanks to a crystal.
The optical scheme used here for THz generation is the method of optical rectification of femtosecond laser pulses with tilted front in a $LiNbO_3$ crystal (for more details see [20]). The set-up involves in particular a grating followed by two lenses and a half-wave plate to turn the polarization vertically (vertical polarization needed in the crystal for THz generation) and then the crystal. The lenses form a telescope used to image the laser spot onto the crystal.

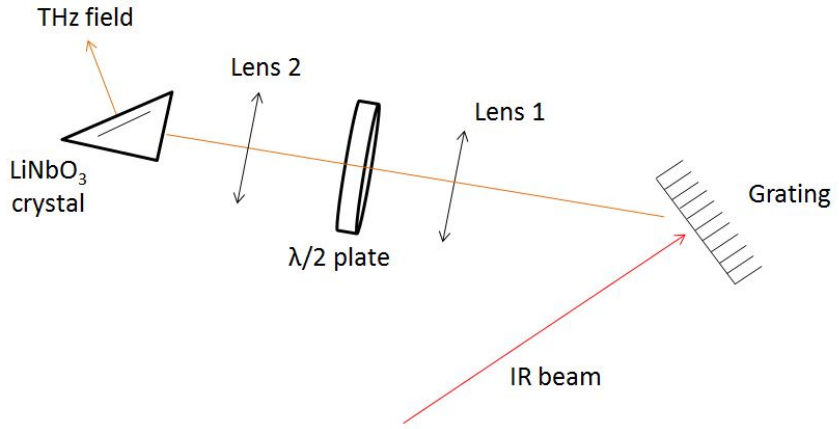

Figure 4.12: Sketch explaining the principle of THz generation by optical rectification.

4.3 IR delayed beam line

Apart from streaking measurements, it is also possible to characterize the XUV beam (high-harmonics) thanks to the method called RABBIT (Reconstruction of Attosecond harmonic Bursts By Interference in Two photon transition) [22]. In this case, the probe beam is not a THz field but simply the fundamental beam: Ti:Sa at 800nm (see chapter 7). In order to be able to compare the results given by both techniques, it is important to build a delay line for the IR which follows more or less the same optical path as the THz field during the THz generation. Thus, the delay stage used for streaking (see chapter 7) could serve for both beams.

This is why a general delay line for IR was built next to the streaking chamber.

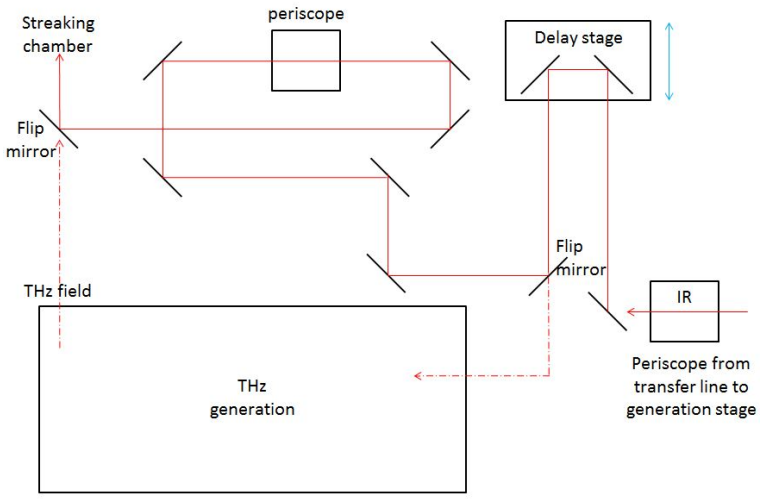

Figure 4.13: Sketch of the IR delay line before the streaking chamber. Flip mirrors are used to quickly pass from one line to the other, depending on the measurement to be done.

4.4 Streaking chamber

In order to do streaking measurements, a special experimental chamber is needed. This is the last vacuum chamber of the line and it is mounted on a motorized optical table so that the XUV beam is correctly sent to the center of a gas jet. Indeed, the streaking chamber involves a gas jet and two Time-Of-Flight spectrometers located in front of each other.

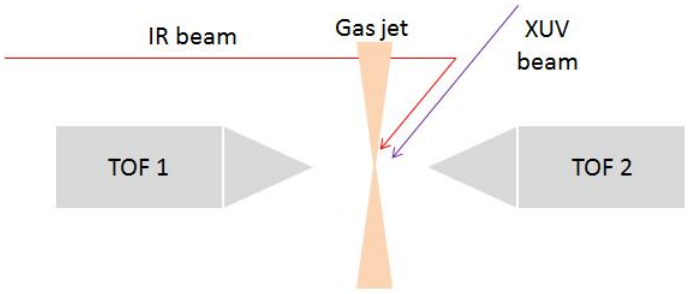

Figure 4.14: Sketch of the inside of the streaking chamber.

The XUV beam is sent to the gas jet thanks to the hole in a parabolic mirror which is used to reflect the IR beam coming from the side of the chamber.

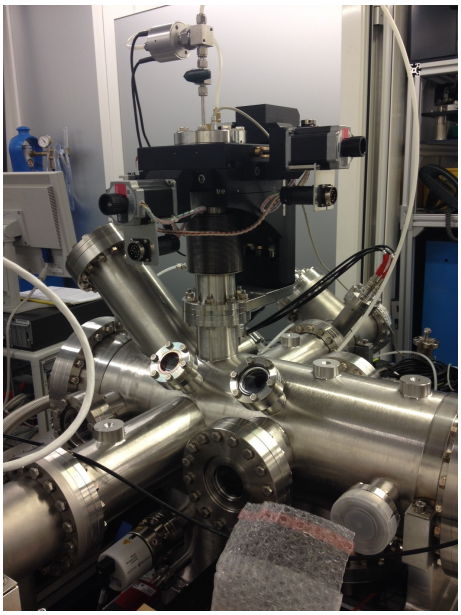

Figure 4.15: Picture of the streaking chamber.

Externally, the signals (arrival times of photo-electrons ionized by the XUV beam) of the two TOF spectrometers are amplified through MCP (Multi Channel Plates) and sent to an oscilloscope to be recorded.

Chapter 5

XUV spectrometer

In order to fully characterize the high-harmonic beam one of the first step is to look at the spectrum of the HHG. A new diagnosis tool, a XUV spectrometer, was commissioned during this master thesis project. This chapter aims at describing how this device works, its calibration and some of the spectra obtained with different gas media.

This spectrometer is used with an ANDOR vacuum camera (Newton series) to observe the spectrum of high-order harmonics generated beforehand in the beam line thanks to a gas cell filled with gas.

5.1 Description of the XUV spectrometer

The spectrometer is a XUV device: imaging flat-field XUV spectrometer by Dr. Hoerlein & Partner. Spectroscopic measurements in the XUV spectral region require several adaptations in the design because first the XUV radiation needs to be measured in vacuum. Then, it is known that the reflectivity of optics in this spectral region is very low and that the signals we want to detect are also really low. Thus, an efficient detecting scheme is necessary as well as an optical solution for the grating design.

Though, imaging grazing incidence vacuum spectrometers offer a solution for such requirements because they allow the combination of the diffractive grating and the imaging optic in only one single optical element. the set-up beneficiates from both the grazing incidence of the XUV radiation onto the grating, which allows high efficiency, and also the imaging properties in the dispersion plane which optimize the detected signal and the spectral resolution. Moreover, the grating is an aberration-corrected flat field optic which allows the focusing of all the wavelengths onto a plane (rather than a circle with a conventional grating). Thus, it is easier to use with a planar detector, such as a CCD-camera that can be put in the focal

plane and then keep a good image quality.
In addition to that, this spectrometer offers different ranges of wavelengths by employing different grating angles and adaptable pieces. In practice, the angle of the grating is fixed and the camera is moved in the horizontal plane to scan the spectrum. This is not very handy but it allows a higher resolution. The distance from the high-harmonic source to the grating required for imaging can be adjusted.

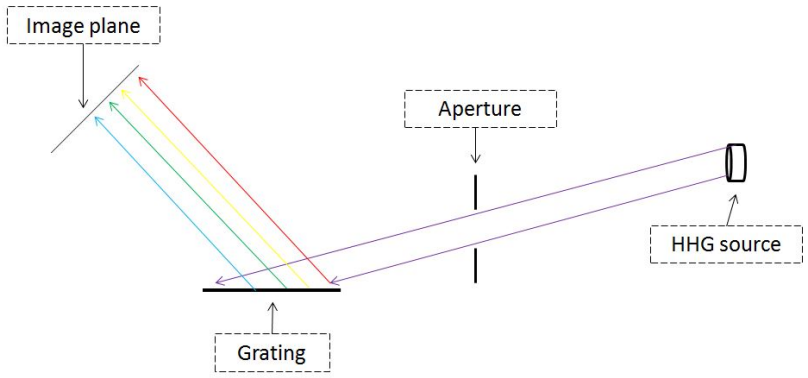

Figure 5.1: This picture shows a schematic drawing of the imaging grazing incidence flat-field spectrometer. The source is directly imaged on the CCD plane thanks to the grating.

The spectrometer is constructed in a modular way allowing operation in different configurations which cover different wavelength ranges. The spectrometer we have has been optimized for the wavelength range from 1 to 17nm and 15 to 70nm with two different gratings.
All components are made from non-magnetic materials.

After the zero-order block used to prevent light directly reflected from the grating from reaching the detector, one can find the angled adapter specifically designed to meet the requirements in source distance and wavelength coverage. The adapter is designed to operate with a specific range of angle of incidence onto the grating depending on the source distance required. The camera mounting is connected directly to the adapter piece.

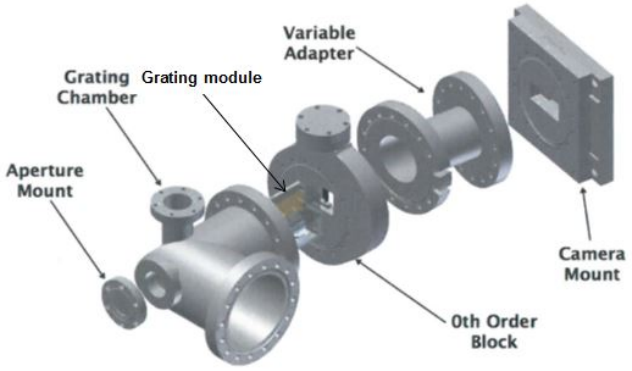

Figure 5.2: This picture shows the basic configuration of the XUV spectrometer.

At the entrance of the spectrometer, an aperture mount is also present (this is not a real slit like in conventional spectrometers). One can choose between different aperture ranges to prevent incident radiation from missing the grating or scattering off its edges. The signal strength as well as the grating angle we use will determine the optimal size of the aperture. But, the grating should not be illuminated for more than 75% otherwise it will cause some degradation and lost of resolution.

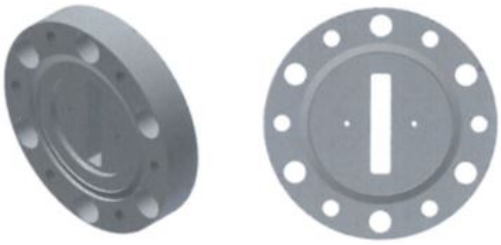

Figure 5.3: This picture shows the aperture mount in the spectrometer.

The heart of the spectrometer is constituted by the grating stage. This part allows us to align the grating correctly thanks to three motors. One moves the grating up and down to ensure that the beam goes to the center of the grating. One ensures focusing and the last one allows rotating the grating at the angle needed. The grating also beneficiates from a protective shield which prevents debris or dust from falling on the surface of the optic.

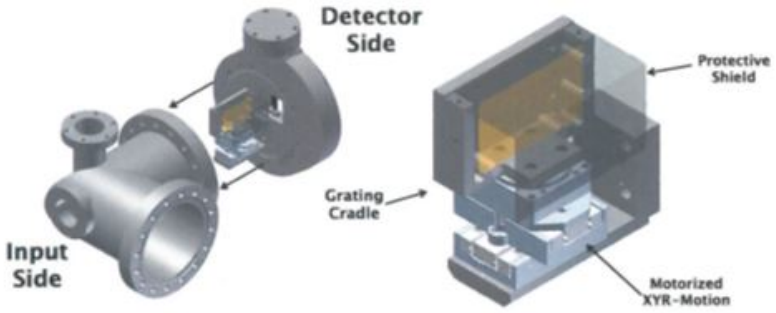

Figure 5.4: This drawing shows the grating stage and its location inside the spectrometer.

The spectrometer is also provided with a zero-order block which traps light that is directly reflected from the grating and thus it should suppress the background. One can also say that it can protect (in a certain way) the detector (camera chip) in the case a filter breaks because the zero-order laser light will then be blocked. There is a small plate inside this block that can be moved in order to carefully block the zero-order beam according to the alignment of the spectrometer. To optimize the block, we simply move the plate to the correct position to block the beam used for alignment once the grating angle has been set (see next section).

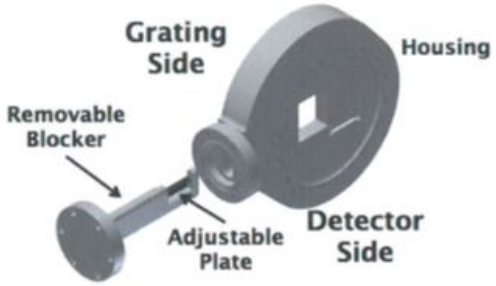

Figure 5.5: This drawing shows the zero-order bean blocker.

And finally, at the end of the spectrometer arm, one has the detector mount which consists of two plates. One is fixed to the spectrometer while the other one can be moved sideways when the spectrometer is vented in order to adjust the spectral region covered by the detector (camera chip).

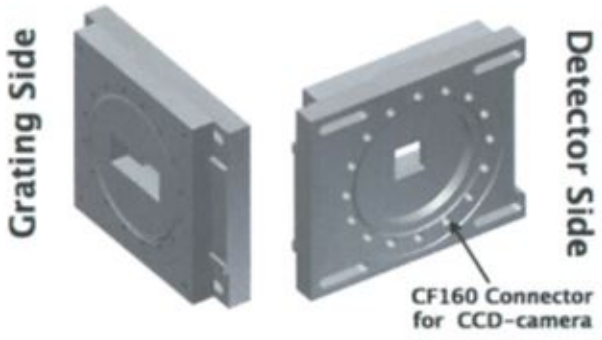

Figure 5.6: This drawing shows the detector mounting system.

5.2 Grating configurations

Two gratings, with 3 different configurations for each of them, are at our disposal.

1200lines/mm grating

This one allows detection of wavelengths between 15 and 70nm from three different source distances. Depending on the source distance, different grating angles are required in order to reach the best imaging configuration as possible in the spectrometer.

Table 5.1: Useful parameters of the 1200lines/mm grating

Source distance (mm)	1700	3400	6800
Grating angle (degrees)	84.9	84.7	84.6

The dispersion of the grating is between 0.8 and 1.3nm/mm and the resolution of the spectrometer in those configurations is given between 0.09 and 0.12nm.

In order to use those configurations, it is necessary to install the right angled adapter. The one for the 1200lines/mm grating as a stronger angle between the two flanges (22 degrees).

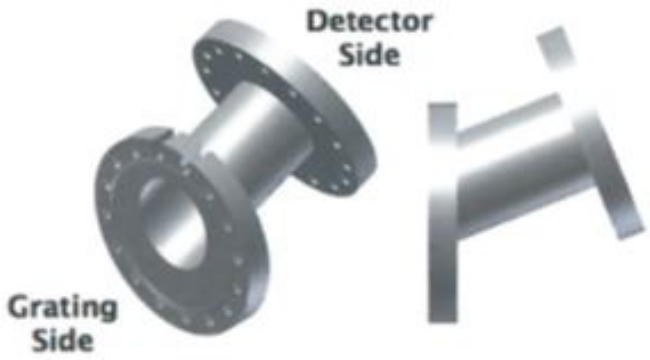

Figure 5.7: This drawing shows the correct angled adapter for the 1200lines/mm grating.

For the generation set-up, the hollow waveguide is located around 3.4m before the grating, so the second configuration mentioned in the above table is used.

2400lines/mm grating

This one allows detection of wavelengths between 1 and 17nm from three different source distances. Depending on the source distance, different grating angles are required in order to reach the best imaging configuration as possible in the spectrometer.

Table 5.2: Useful parameters of the 2400lines/mm grating

Source distance (mm)	1700	3400	6800
Grating angle (degrees)	88	87.9	87.8

The dispersion of the grating is between 0.2 and 0.5nm/mm and the resolution of the spectrometer in those configurations is given between 0.03 and 0.05nm.

In order to use those configurations, one has to install the right angled adapter. The one for the 1200lines/mm grating as a lower angle between the two flanges (10.5 degrees).

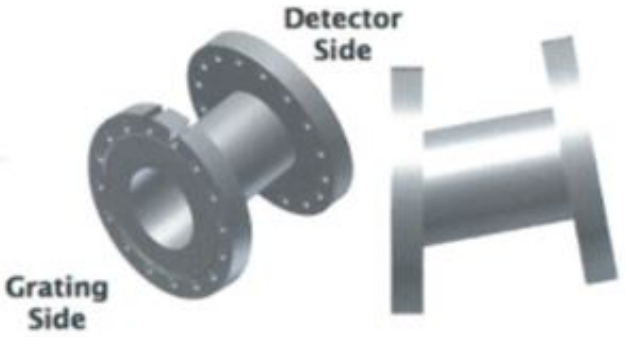

Figure 5.8: This drawing shows the correct angled adapter for the 2400lines/mm grating.

5.3 Presentation of the vacuum camera

The camera is from the series Newton (DO-940) of the brand ANDOR. It has a 2048×512 array of $13.5\mu m \times 13.5\mu m$ pixels which can be cooled down to -100 degrees in order to get negligible dark current.

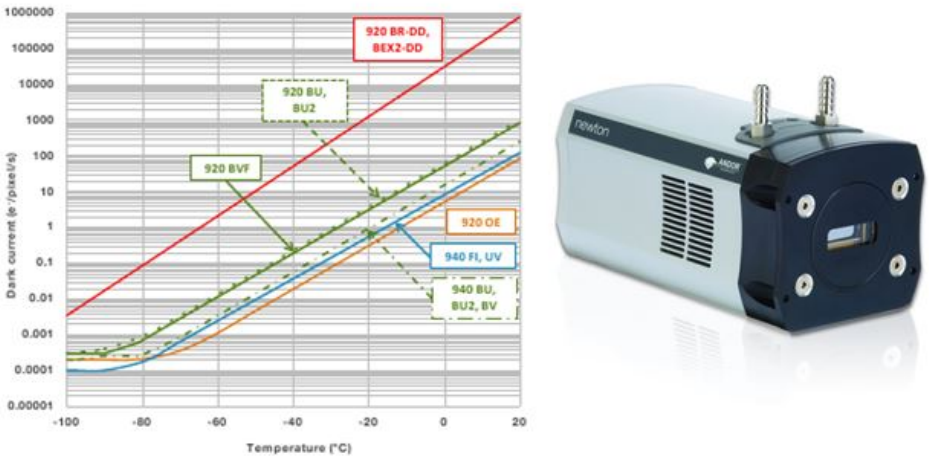

Figure 5.9: These pictures show the dark current evolution as a function of the temperature and also how the camera looks like.

Thus the image area is $27.6mm \times 6.9mm$. It can allow readout up to 3MHz.

The quantum efficiency of the camera is also needed in order to be able to convert integrated numbers of photon counts to energy.

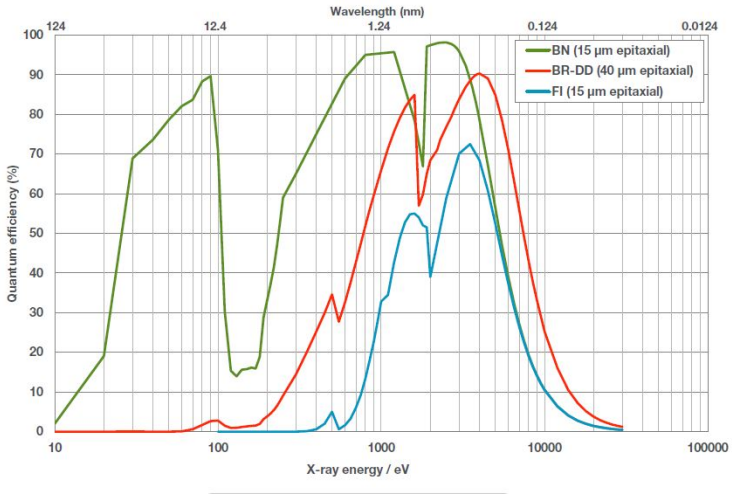

Figure 5.10: These curves show the evolution of the quantum efficiency as a function of the wavelength. Our camera is of the type back illuminated (BN).

To see the alignment procedure, please refer to Appendix A.

5.4 Calibration of the spectrometer

The spectrometer can operate with two different gratings: one for the shorter wavelengths (1 to 17nm) and another one for the longer wavelengths (15 to 70nm). In the case of the longer wavelengths, the grating has 1200lines/mm and in the other case it has 2400lines/mm.
Harmonics of the Ti:Sa beam are used. They are produced by argon gas in the gas cell. To be able to calibrate the spectra seen thanks to the camera, the procedure use the fact that we have aluminum (Al oxide) filters before the spectrometers in order to get rid of the fundamental at 800nm.
There are two filters and each of them has a thickness of 200nm leading to a total thickness of 400nm. The transmission of a 0.4μm thick layer of aluminum is represented below for the interesting range of energy:

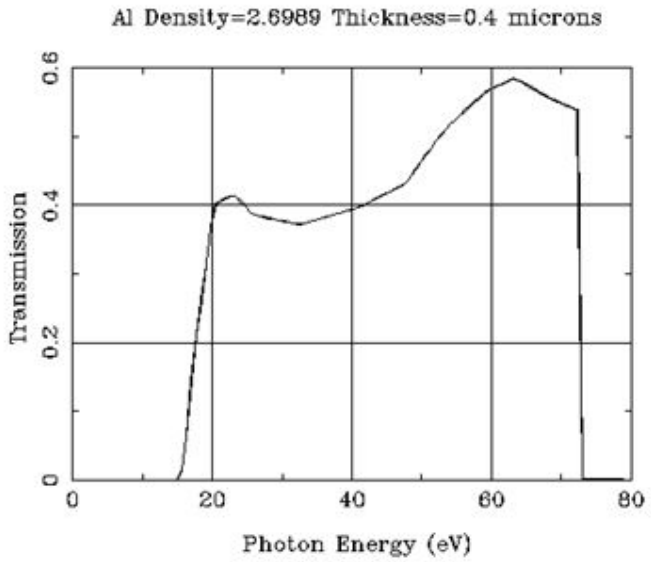

Figure 5.11: This graph represents the transmission of a 0.4μm Aluminum filter as a function of the photon energy. The graph was taken from the x-ray database website `http://henke.lbl.gov/optical_constants`.

The first cut-off occurs for the energy of 15eV. This limit will be considered in the following calibration steps.
So, one should only see on the spectra the harmonics which have energies higher than 15eV. Moreover, a cut-off for the energy of 50eV is also present (cut-off law for the harmonic plateau), so there is only need to consider few harmonics.The fundamental wavelength is 800nm that is to say of energy 1.55eV.Only odd harmonics are considered, which are then separated by 3.1eV. So the interesting harmonics can be counted:

Table 5.3: Harmonics

HH number	9	11	13	15	17	19
Wavelength (nm)	72.8	61.6	53.4	47.1	42.1	38.1
Energy (eV)	17.05	20.15	23.25	26.35	29.45	32.55

Table 5.4: Harmonics

HH number	21	23	25	27	29
Wavelength (nm)	34.8	32	29.7	27.6	25.8
Energy (eV)	35.65	38.75	41.85	44.95	48.05

The next step consists in determining the location of each harmonic on the camera chip. In order to do that, it is necessary to determine the angle at which the different harmonics are leaving the grating. First order diffraction only needs to be considered and the following configuration for the grating inside the spectrometer can be sketched as follows:

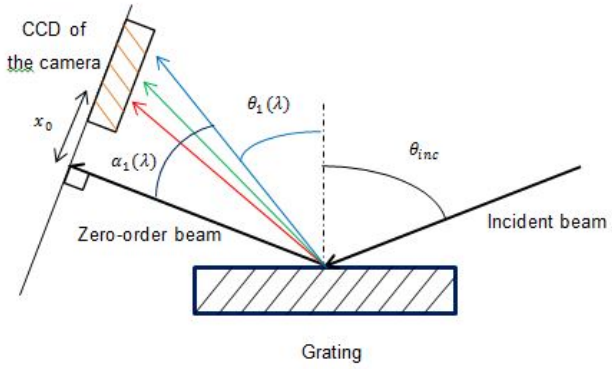

Figure 5.12: This sketch presents the grating geometry inside the spectrometer arm.

- x_0 is the supposed pixel position of the zero-order (it can be outside of the camera chip, thus being a negative value)
- - The distance from the grating to the plane of the camera chip is called L and must be around 27cm (to be checked with optimization calculation)

Then, three free parameters are unknown:

- x_0 the supposed pixel position of the zero-order
- θ_{inc} the incident angle of the beam on the grating
- L the distance from the grating to the plane of the camera chip

The aim of the calibration is to find a formula which gives the pixel position of each harmonic as a function of those three free parameters. One should then be

able to optimize the calculation by taking a spectrum and launching an optimization algorithm on this formula. Thus, one would retrieve the correct parameters.

So let's first derive the needed formula which involves the free parameters. From the above sketch, one can write the equations:

$$\theta_1(\lambda) = arcsin\left(\frac{\lambda}{d} - \sin(\theta_{\text{inc}})\right) \tag{5.1}$$

This is the grating law for the first order of diffraction, where d is the groove density for the grating.
Then, let's be careful with the orientation of the angles on the drawing. To do that, let's sketch the different orientations:

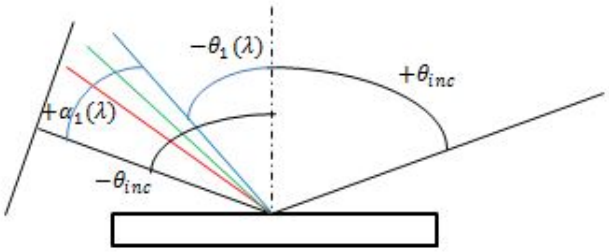

Figure 5.13: This sketch presents the different orientations of the angles onto the grating.

So now, the angle $\alpha_1(\lambda)$ is now a positive angle and can be expressed as:

$$\alpha_1(\lambda) = \theta_{\text{inc}} + \theta_1(\lambda) \tag{5.2}$$

Thus, the pixel position of the different harmonics with respect to the zero-order position becomes:

$$x_1(\lambda) = L \cdot \tan(\alpha_1(\lambda)) \cdot \frac{1}{pixelsize} \tag{5.3}$$

Then, one needs to subtract the pixel position of the zero-order, which is also unknown:

$$x_1^{real}(\lambda) = x_1(\lambda) - x_0 \tag{5.4}$$

Thus, the final pixel position is:

$$x_1^{real}(\lambda) = L \cdot \tan\left(\theta_{\text{inc}} + arcsin\left(\frac{\lambda}{d} - \sin(\theta_{\text{inc}})\right)\right) \cdot \frac{1}{pixelsize} - x_0 \tag{5.5}$$

In order to do the calibration, with the help of a Matlab code, we choose to represent the wavelength as a function of the pixel position, thus, the above equation is reversed:

$$\lambda = d\left\{\sin(\theta_{\text{inc}}) + \sin\left(arctan\left(pixelsize \cdot \frac{x_1^{real}(\lambda) - x_0}{L}\right) - \theta_{\text{inc}}\right)\right\} \tag{5.6}$$

In order to have the distance L in mm, the pixels size should be converted to mm also:

$$pixelsize = 13.5 * 10^{-3} mm \tag{5.7}$$

In the previous case, the wavelength unit would be the same as d. d is the parameter of the grating, that is to say the inverse of the line density of the grating. Here, the parameter is 1200 lines/mm, so if the wavelength is in nm then $d = 833.33$nm.

It is sometimes more convenient to express the wavelength in energy unit (eV). In order to do that, the above equation is divided by 1240 (conversion from nm to eV via Planck constant).

The final calibration gives us the following results for the three free parameters:

Table 5.5: Calibration results

Angle of incidence (degrees)	77
Distance grating-camera (mm)	316
Pixel position for 0 order	≈ -2600

5.5 How to proceed for the calibration

The theoretical model for the calculation of the wavelength is now established for a given pixel position on the camera chip.
In order to calibrate the spectrometer, several spectra were recorded where different harmonics could be seen. In theory one does not know which harmonic number they have. Thanks to Matlab, the files produced by the camera can be opened (.spe files) and the spectra are displayed. Then the pixel positions of the different peaks are located. Those positions correspond to the variable $x_1^{real}(\lambda)$. The variable λ is not fixed (as we do not really know the harmonics number we are looking at, but we can have a first guess and then change the numbers as we get the results of the code). Indeed, while recording the spectra, some initial values are obtained for the three free parameters (θ_{inc},L and x_0). Though, as the code runs, one can deduce if the hypothetical values of the wavelengths are right or not by comparing

the retrieved values of the parameters to the calculated one.

Basically, the Matlab code is an optimization fitting. It sketches the couples of points derived from the recorded spectra and then tries to fit a curve to them via the theoretical model with the free parameters.

5.6 Results of calibration

Calibration procedures were tested first with Argon gas as a generation medium and then with Neon to confirm it.

In order to do the calibration in terms of counts per bandwidth, we need to apply a correction factor. Indeed, the raw data contains the counts per pixel. However, the weight in energy for each pixel is not constant so we need to calibrate it. The formula used for this is the following where we find again the free parameters mentioned earlier:

$$pix = L \tan\left(\theta_{inc} + \arcsin\left(\frac{1240}{d \cdot E} - \sin\left(\theta_{inc}\right)\right)\right) - x_0 \tag{5.8}$$

Where pix is the energy weight for one pixel, x_0 is the location of the zero-order on the CCD plane and E is the photon energy in eV. This formula is then derived as a function of the energy and then this derivative is the correction factor which we apply to our raw data in order to calibrate the number of counts in number of counts per bandwidth.

Argon gas

The two aluminum filters were used to get the spectra with Argon gas. The calibration resulted in the display of harmonics 29 to 17, from left to right:

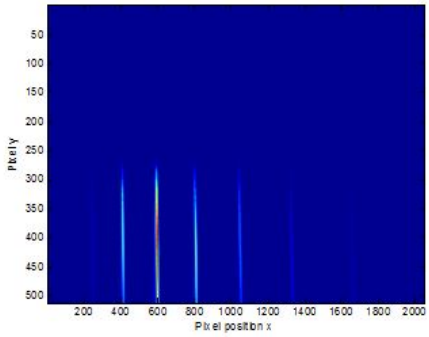

Figure 5.14: This spectrum shows the different harmonic lines down to 25.8nm (29^{th} harmonic, 48.1eV).

The calibrated spectrum is then the following:

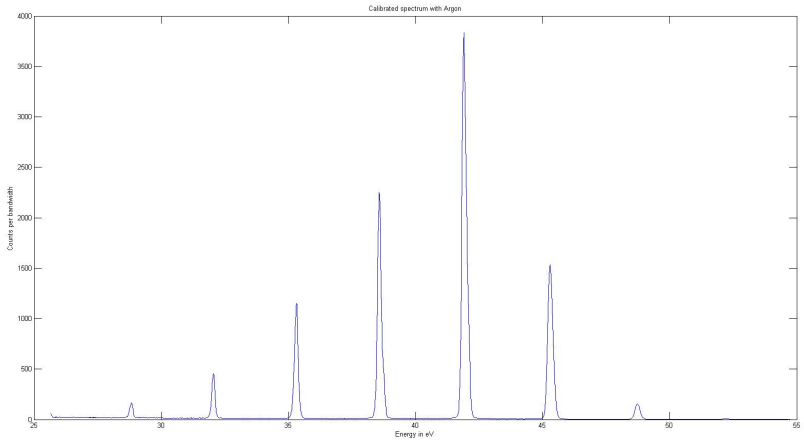

Figure 5.15: This curve shows the calibrated spectrum for generation in Argon gas.

Neon gas

The specificity of Neon gas is that now fewer lines can be seen on the spectrum, making it easier to confirm a given calibration. However, in order to use these harmonics lines, we need to work with different filters. We keep one aluminum filter and replace the second one with a zirconium (Zr) filter which is way more fragile.

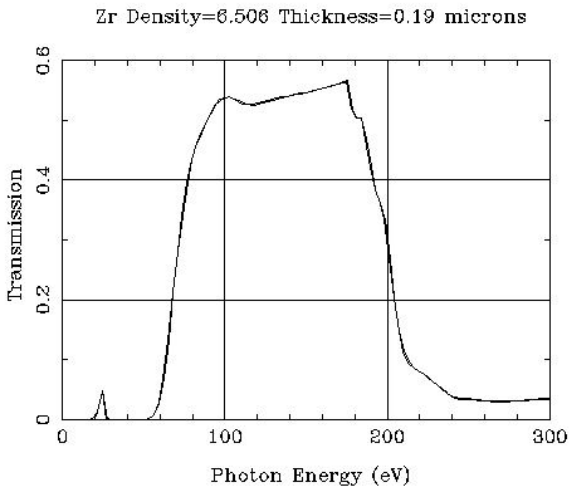

Figure 5.16: This graph presents the transmission of a Zirconium filter of thickness 0.19μm.

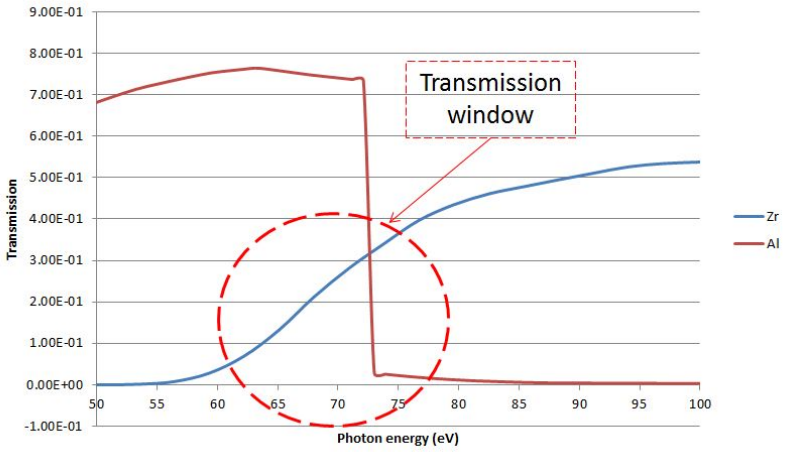

Figure 5.17: This graph presents the transmission window obtained by combining Al and Zr filters.

Then, by using both an aluminum filter and a zirconium filter, there is only a 20eV window left from around 55eV to 75eV. Though, the calibration would be

easier to handle.

The calibration resulted in the display of harmonics up to 47 on the left of the image below:

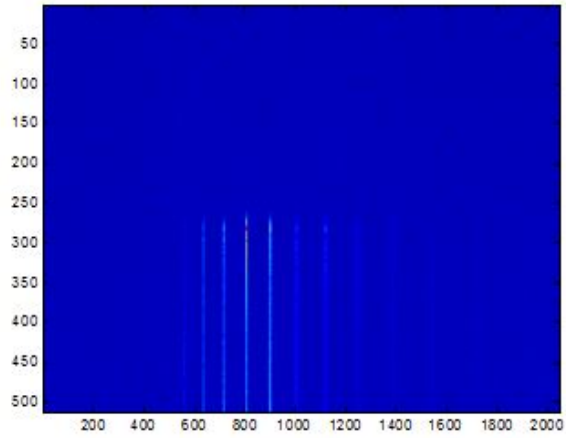

Figure 5.18: This spectrum shows the different harmonic lines down to 16.3nm (47^{th} harmonic, 75.95eV).

The calibrated spectrum is then the following:

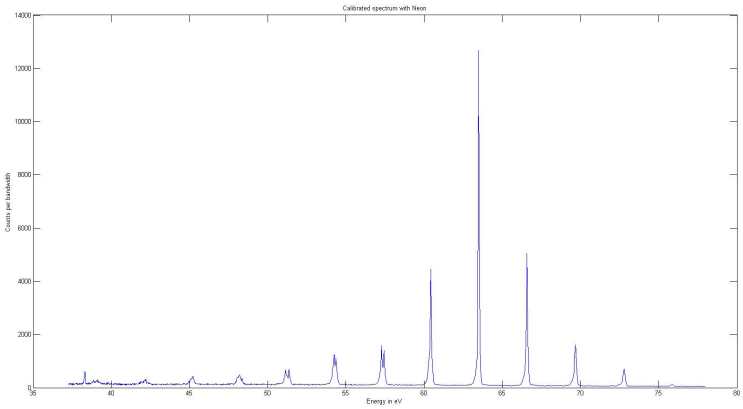

Figure 5.19: This curve shows the calibrated spectrum for generation in Neon gas.

Generation in Helium

High-harmonics were also generated in He at the end of the project and the spectrum was displayed thanks to a transmission grating located in front of the vacuum camera in the diagnosis chamber.
The ionization potential of Helium is higher than for neon and Argon, thus it should be possible to see higher energies. Nevertheless, it is also more difficult to ionize this medium, thus the beam splitter of the beam line was removed in order to be able to have 20mJ only for the generation of high-harmonics.

Due to the geometry of the set-up (transmission grating, 2000lines/mm), the Matlab routine for the calibration was adapted and a calibrated spectrum can be the following, where the highest harmonic order seen is 59. Two Zirconium filters were used here to filter out the 800nm and in order to have a larger window than with 2 Aluminum filters (especially concerning the higher energies because the cut-off for the Al filters is around 73eV).

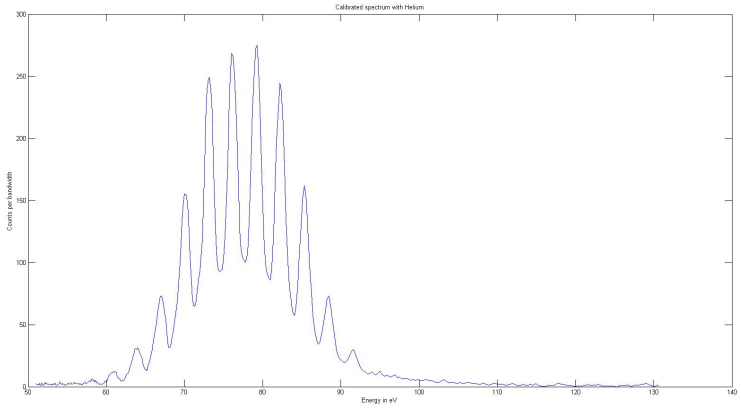

Figure 5.20: This curve shows the calibrated spectrum for generation in Helium gas.

One can notice that for generation in Helium, the resolution of the spectrum is quite limited. This due to the fact that, in this case, we used the transmission grating which is not optimized for imaging purposes. Moreover, there is no real aperture allowing to select the beam, just a kind of knife-edge. This might explain why the imaging is that poor, with some lines which seem to be nearly merging to each other.

5.7 Pressure scans with Neon

The goal of this section is to keep all the parameters constant for the generation of harmonics and change the pressure of the neon gas injected in the gas cell and study the harmonic spectrum for each pressure.

The initial parameters are the following:

- Ti:Sa energy before the entrance of the vacuum line (90% of maximum pump power on control panel) that is to say 7.3mJ.
- Pulse duration of Ti:Sa measured before the entrance of the vacuum line with the WIZZLER: $FWHM = 58fs$.
- Channels values of the spectrometer motors: $B = 0mm$, $A = 4.8mm$ and $C = 349.4degrees$.
- Two aluminum filters in the vacuum chamber, before the entrance of the spectrometer arm.
- Acquisition time for the camera software: $5sec$
- High sensitivity configuration on the camera software (enables up to 150 000 electrons per pixels)

As the pressure will decrease, the opening time of the gas valve will need to be increased in order to see the harmonic lines (it corresponds to the "width" control in the EPIC panel). It helps us to optimize the spectrum obtained thanks to the camera.
The range of pressures used is from 1.5bars to 6bars by steps of 0.5bars. The first step is to calibrate the spectrometer according to the previous sections of this chapter. To do this, the pressure was fixed to 4.5bars and harmonics 35 to 47 were observed:

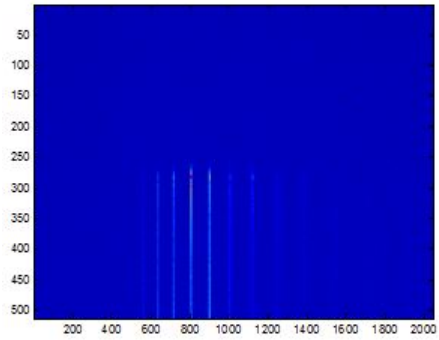

Figure 5.21: This spectrum shows the different harmonic lines down to 16.3nm (47^{th} harmonic, 75.95eV) for Neon gas as the nonlinear medium.

Depending on the pressure, it is interesting to explore the way the shape of the harmonic lines is evolving. Due to noisy spectrum, the lines of the matrix (data of the camera) were integrated:

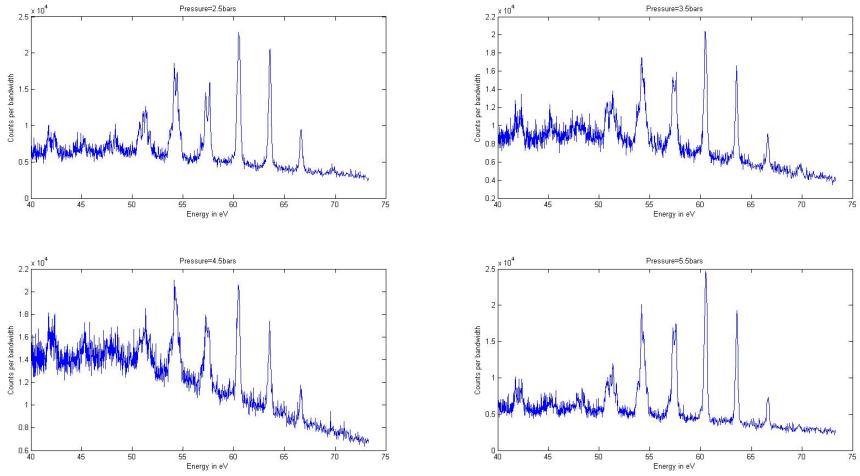

Figure 5.22: These curves show the spectra of the high-harmonics for different pressures.

There is no real change in the shape of harmonics, however, one could look at the overall spectrum shape. In order to do that it was decided to fix the pressure given by the pressure controller and to change instead only the opening time of

the gas valve (it changes the gas flow). The optimization of the spectrum is now done by adjusting the "delay" function of the gas jet (duration between two gas pulses) for the first opening time selected ($300\mu sec$). As the spectrum is not stable shot-to-shot, it is necessary to record several shots for the same configuration and integrate when analyzing the data. The pressure set on the controller is 4.5bars.

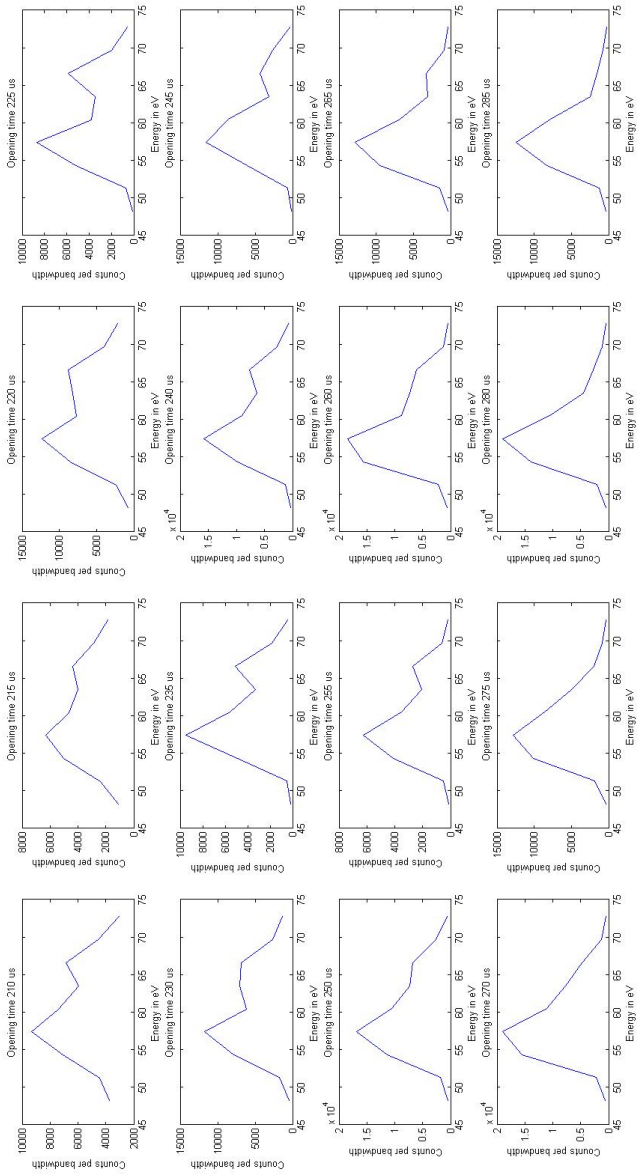

Figure 5.23: These curves show the spectra of the high-harmonics for different opening times (expressed in μ sec). The abscissa is calibrated with the energy in eV.

These curves give an indication on the phase-matching efficiencies for the different energies. However, one has to take into account the transmission of the aluminum filters to have relevant results. In our case, a good estimation of the thickness of the oxide layer is 16nm for an aluminum filter of thickness 0.2μm. This represents 8% of oxidation in total. References [26] and [27] give some measurements of this layer of oxide.

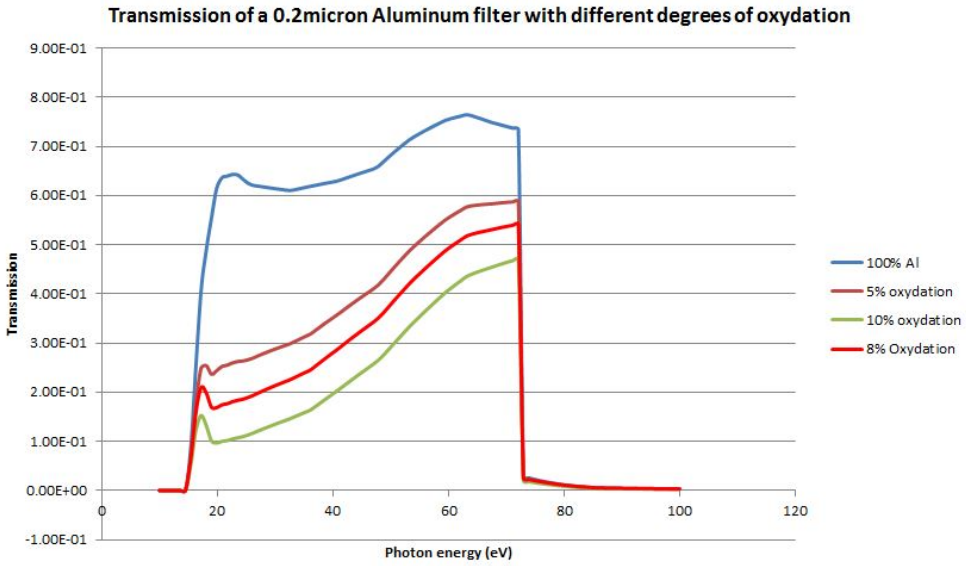

Figure 5.24: These curves show the transmission of one aluminum filter for different degrees of oxidation.

This means that for small opening times were the spectrum shape is quite uniform, there is actually a higher signal for lower energies (thus a better phase matching for lower energies).

Then, for higher opening times (higher pressure difference), there is a more uniform spectrum if the correction due to the filter transmission is applied. This means that the phase matching is good for the whole 20eV energy window that was considered. Below are the curves corrected thanks to the aluminum filter transmission (for two filters of 100% aluminum).

The result is clearer if the evolution of the counts per bandwidth are displayed as a function of the opening time for the different harmonic lines as fig. 5.26 shows.

We can clearly see that it is possible to enhance the signal of one specific energy of an harmonic line by selecting the good opening time of the gas valve, improving thus the phase matching for this particular energy.

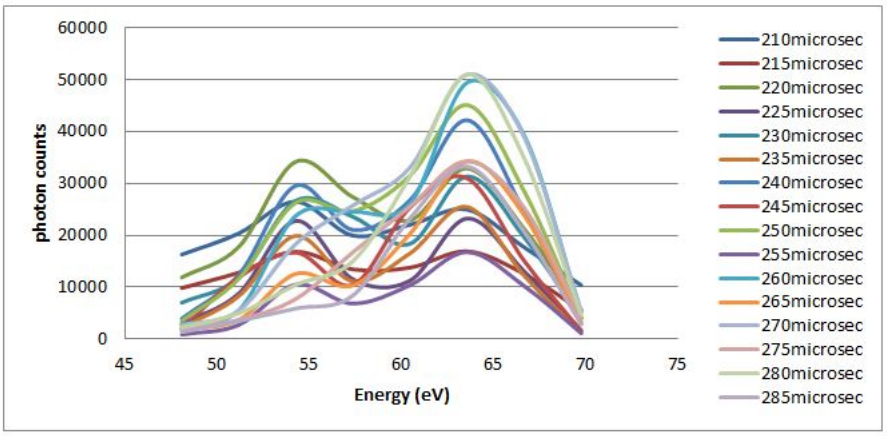

Figure 5.25: These curves show the corrected curves for different opening times for aluminum filters with no oxidation.

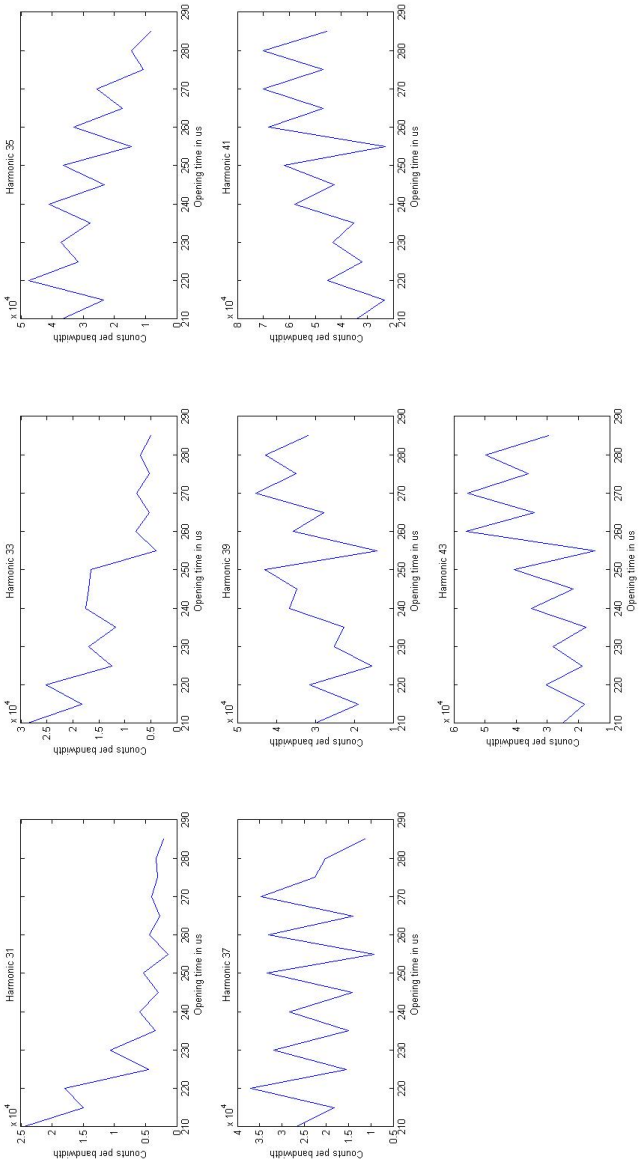

Figure 5.26: These curves show the behavior of the counts per bandwidth for each harmonic for different opening times, taking into account that we have aluminum filters with 8% oxidation.

Chapter 6

Optimization of the HHG beam line

Efficient high-harmonic generation can also be achieved by optimizing the beam line, that is to say, by improving the focusing set-up for instance or the design of the beam line before hitting the target (hollow waveguide).

6.1 HHG profiles

One first step is to look at the HHG beam profile. This is done thanks to the PRINCETON camera located in the diagnosis chamber described in chapter 4. The following beam profiles are taken with a gas cell of length 6cm.

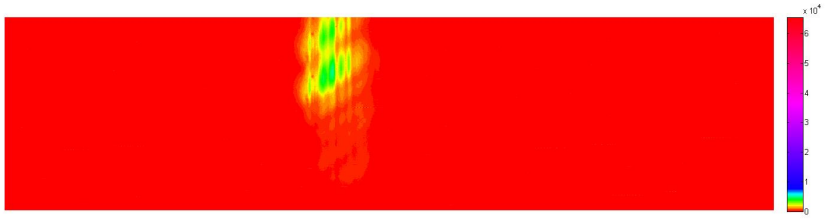

Figure 6.1: This picture shows the profile of the HHG beam.

There are two different toroidal mirrors at our disposal. The previous profile was taken with the gold toroidal mirror. When putting the other toroidal mirror (longer focal length: 5m), the following profile is obtained:

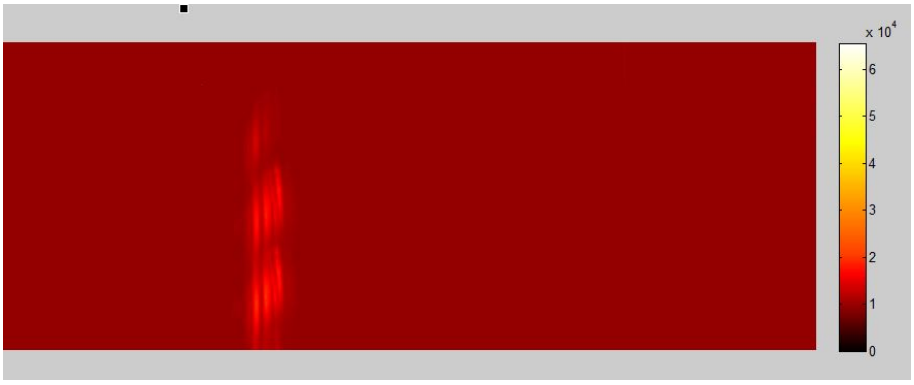

Figure 6.2: This picture shows the profile of the HHG beam with the other toroidal mirror.

One can notice that, on the profiles, there are some stripes on the sides of the harmonic spots, like an interference pattern which might come from a periodic structure present on a mirror for instance. This is why a surface quality testing of the focusing mirrors will be handled later on in this chapter in order to determine from where this pattern comes from.

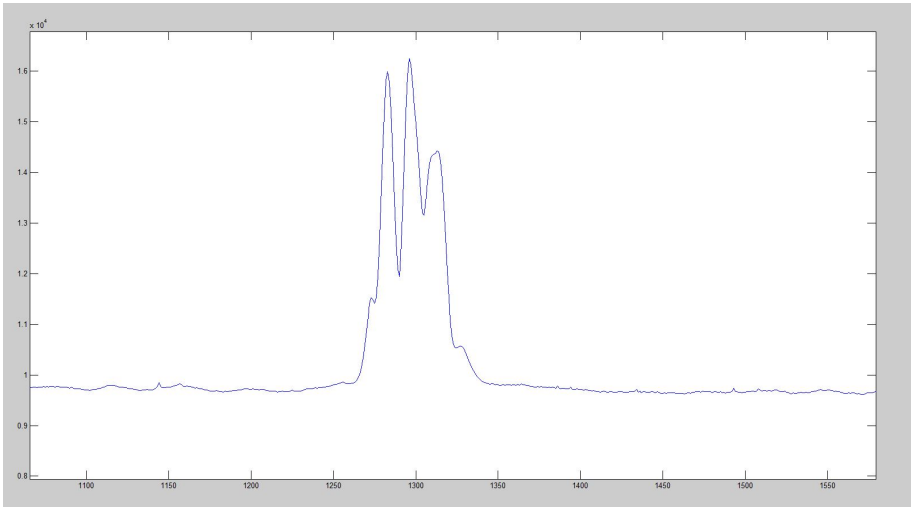

Figure 6.3: This graph shows the different “stripes“ seen on the HHG beam profile. The period of the “interference pattern“ is around 0.2mm.

6.2 Re-design of the focusing set-up for generation

It was previously mentioned that the disadvantage of the actual focusing set-up (up to the target) was that a lens is used and it introduces chromatic aberration. This means that, in the gas cell, the different wavelength of the fundamental beam (Ti:Sa) are not exactly focused at the same point.

The lens was bought from the company CVI Laser Optics. The radius of curvature is 1545mm and it is made of fused silica (SiO_2). The specifications for the wavelength are the following:

Table 6.1: Specifications lens

Wavelength (nm)	532	1064
Focal length (mm)	3353.5	3436.2

If we apply a linear fit to these values, the focal length at 800nm should give us:

$$f(800nm) = 3395mm \tag{6.1}$$

To cross-check this approximate calculation, one could calculate the focal length for this particular wavelength thanks to the following formula:

$$f = \frac{R}{n(\lambda) - 1} \tag{6.2}$$

Where the refractive index for fused silica is obtained through the Sellmeier equation:

$$n^2 = 1 + \frac{A_1\lambda^2}{\lambda^2 - \lambda_1^2} + \frac{A_2\lambda^2}{\lambda^2 - \lambda_2^2} + \frac{A_3\lambda^2}{\lambda^2 - \lambda_3^2} \tag{6.3}$$

From the literature [28], the different parameters of this formula can be retrieve:

Table 6.2: Sellmeier parameters for Fused Silica

Parameters	A_1	A_2	A_3	λ_1 in μm	λ_2 in μm	λ_3 in μm
Fused Silica	0.0696749	0.408218	0.890815	0.069066	0.115662	9.900559

This gives the following result for the focal length at 800nm:

$$f_{sell}(800nm) = 3406mm \tag{6.4}$$

There is 0.3% error with the previous result.

Due to the potentially chromatic aberration introduced by the lens, it was decided to try another design for this focusing set-up. Instead of a lens a spherical

mirror of same focal length can be used and the beam can enter the vacuum line from one side thanks to a 45 degrees mirror with a hole so that the focusing beam can still go to the final target (gas cell). Let's explain this new design with the following drawing:

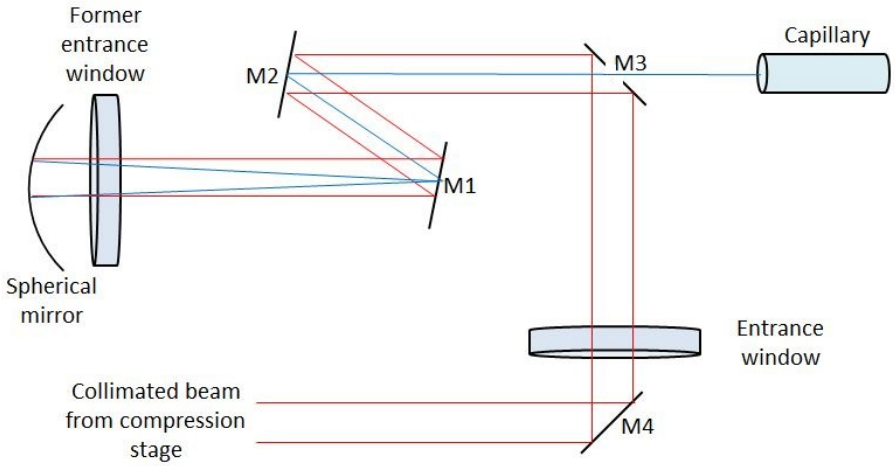

Figure 6.4: This sketch shows how the beam is focused into the cell thanks to a spherical mirror. The angles of the mirrors M1 and M2 are exaggerated here.

The advantage of this configuration is that the spherical mirror can be used with normal incident radiation to avoid any parasitic optical aberration. One also has to be careful to have a sufficiently small hole in the 45 degrees mirror in order no to loose too much of the incoming beam.

However, it happened that the flat gold mirror with the hole cannot be used in 45 degrees configuration because the hole was drilled straight (perpendicular to the surface of the optics). Thus, another set-up must be implemented where this flat mirror is used near to normal incidence.

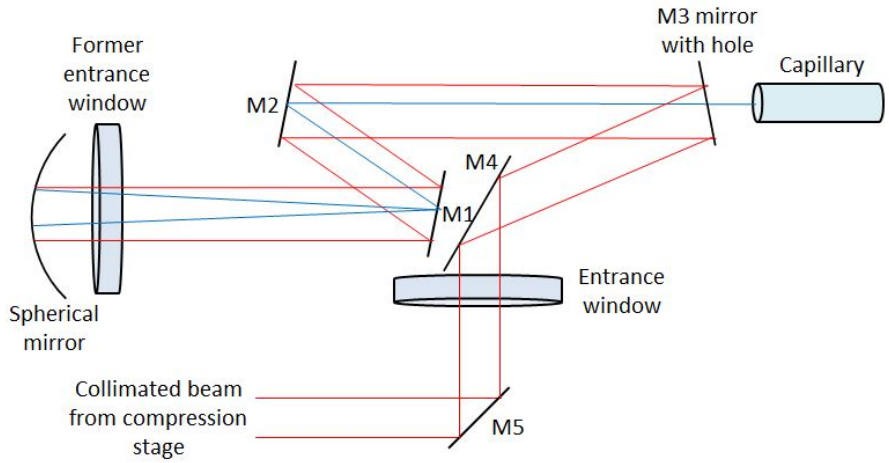

Figure 6.5: This sketch shows the second design solution. The angles of the mirrors M1 and M2 are exaggerated here.

In this new configuration, the mirror M3 is used near normal incidence but with an angle such that the combination M2-M1 can still be used. In order to do that, the mirrors M4 and M5, normally at 45 degrees, must have a bigger angle. It was decided to keep M3 fixed and to adjust the alignment thanks to M4 and M5 first. Then the fine alignment is done by moving both the mirror with a hole and the spherical mirror to get the focused beam at the center of the target.

Beam profiles

With the spherical mirror of focal 3m, high-harmonics are generated in Argon and the beam profile is studied thanks to the vacuum camera.

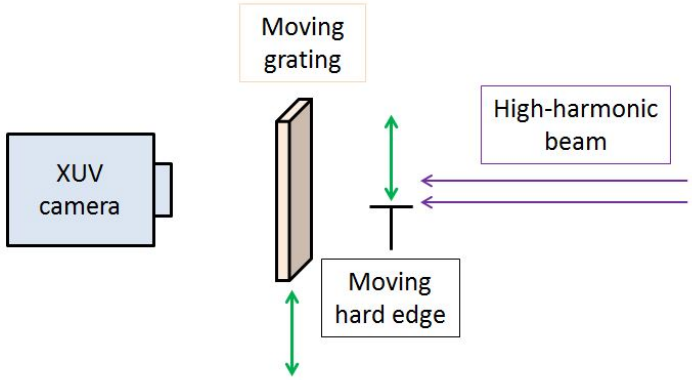

Figure 6.6: This sketch shows the experimental set-up use for this measurement.

Then, it is possible to determine if the new set-up introduces some chirp in the XUV spectrum. In order to do that, the transmission grating is shifted in front of the vacuum camera and thanks to a knife-edge, parts of the beam are cut. This way, the whole beam profile is scanned and for each position of the combination grating-knife-edge, a spectrum is recorded. The zero-order is also seen on this spectrum.

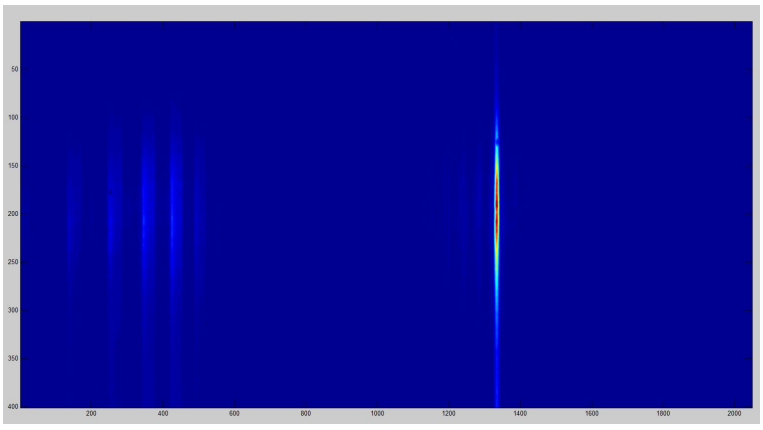

Figure 6.7: This picture shows an example of the spectrum taken for one part of the beam profile. The zero-order can be seen as well as the first order of diffraction on the left side.

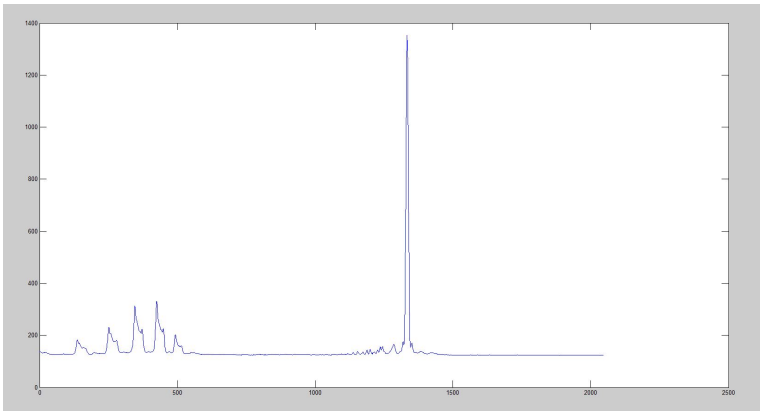

Figure 6.8: This curve shows an example of the spectrum taken for one part of the beam profile. The zero-order can be seen as well as the first order of diffraction on the left side.

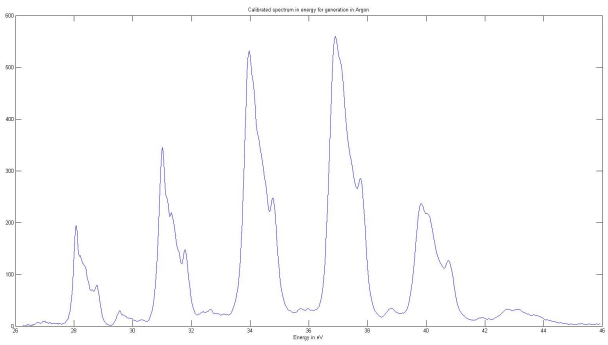

Figure 6.9: This curve shows the calibrated spectrum for generation in Argon gas with the transmission grating.

The goal of this study is to determine if the first order of diffraction peaks are still at the same location compared to the zero-order. If it is not the case, this would mean that there is spatial chirp introduced by the set-up.

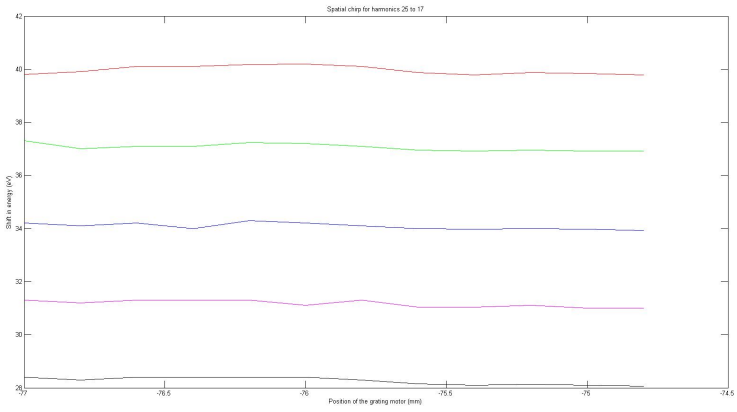

Figure 6.10: These curves show the shift in eV measured for the different harmonic lines of the spectrum as a function of the grating position. With the grating, different parts of the beam profile were selected.

Then, we can deduce, that there is no real spatial chirp given those curves. The spectrum is quite stable.

Another study can be done by using the shortest pulse as possible thanks to the spectral shaping with the MAZZLER. The MAZZLER loop was set for a spectrum with a full width of 100nm.

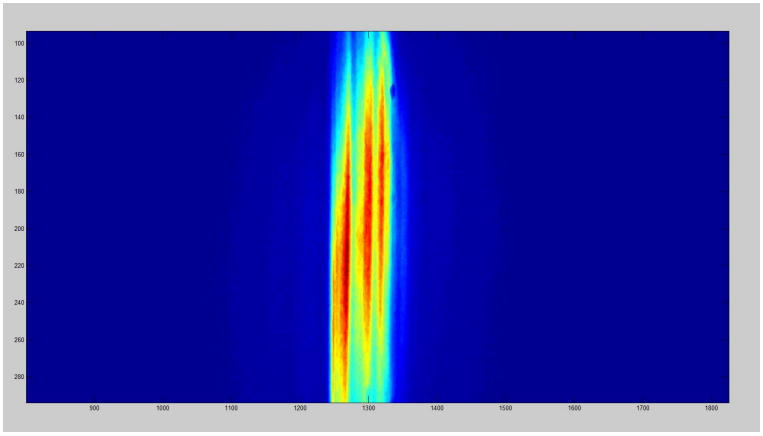

Figure 6.11: This picture shows the beam profile with the new focusing design and the short pulse configuration. The generation medium is Argon.

The beam shows three main lobes. Let's look at the spectrum for each lobe.

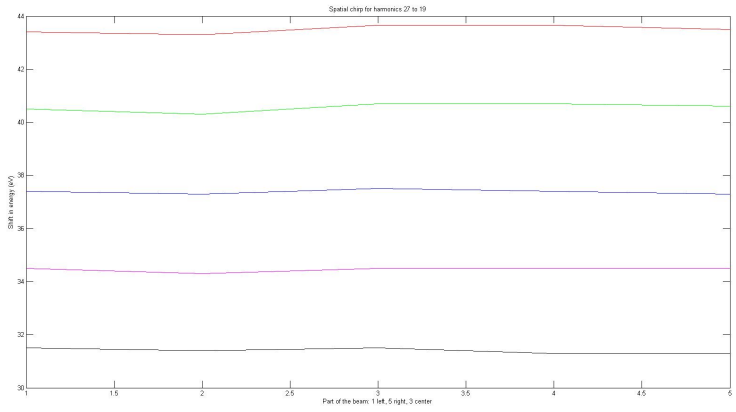

Figure 6.12: These curves show the shift in eV for each harmonic in the spectrum as a function of the part of the beam which is scanned. Position 1 represents the extreme left of the beam, 5 is the right part and 3 is the center of the beam.

Once again, the shift is really small and we can conclude that there is no spatial chirp for our XUV beam.

6.3 Surface quality of mirrors

Another improvement of the HHG beam line can be done by optimizing the focusing set-up to the diagnosis chambers. The focusing is allowed by the above mentioned combination of a flat mirror (glass) and a toroidal mirror (gold). The flat mirror actually used is non-coated and transmits a part of the 800nm. It is designed for x-ray radiations.

One first step consists in characterizing this mirror. One can measure how much it transmits the 800nm beam. This is done with a special detector (for a Joulemeter) which can detect down to several hundreds of nJ. The Ti:Sa beam was attenuated thanks to optical densities in order not to damage the empty target (measurements performed with open vacuum chamber, at atmospheric pressure, without gas in the target except air).

The energy measured before the flat mirror is:

$$E_{in} = 2.8\mu J \tag{6.5}$$

And after the flat mirror:

$$E_{out} = 1.9\mu J \tag{6.6}$$

This means that the flat mirror transmits 68% of the IR beam.

The same flat mirror is also available but with a coated surface. In order to characterize its surface quality, interferometry measurements were performed on this mirror.

Zygo NewView

The first interferometer used is a ZYGO NewView. This device can characterize the roughness of a surface and is based on white light measurement. Several interferometric objectives can be used with this ZYGO such for example a $\times 20$ Mirau objective or a $\times 2.5$ Michelson objective.

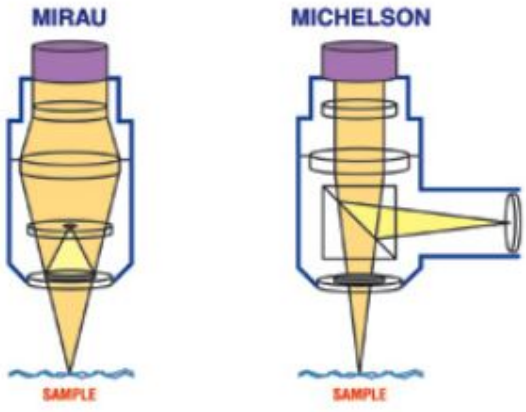

Figure 6.13: This sketch from the website of ST Instruments is showing how the interferometric objectives are working.

The lens of the objective is coupled to a beam splitter so that part of the light is reflected to a mirror at 90 degrees for reference in the case of Michelson. In the case of the Mirau objective, the reference beam is collinear to the light path.

First, the Mirau objective (field of view $2.82 \times 2.11mm$, numerical aperture 0.075) is used to characterize the roughness of the sample (flat mirror) in the center. The vertical resolution of the device is around 0.1nm. A peak-to-valley roughness of 14.5nm was measured (rms value 3.2nm) and the surface is quite flat (radius of curvature in x and y directions larger than 100m):

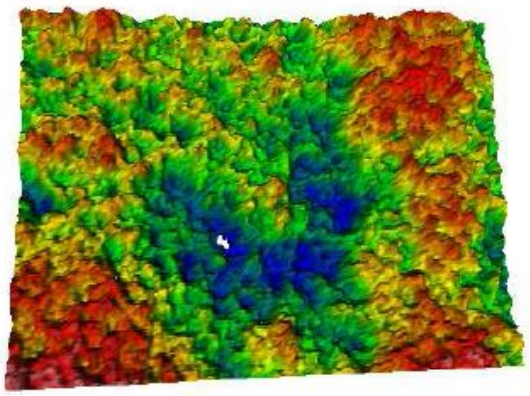

Figure 6.14: This picture shows the profile of the surface of the flat mirror near the center of the sample. Acquisition with the software METROPRO.

This means that the mirror is not super polished (PV of the order of tens of nm instead of 0.1nm for super polished optics).

With the second objective (Michelson, field of view $0.35 \times 0.26mm$, numerical aperture 0.4), the measurement is less localized and a peak-to-valley roughness of 5.4nm was found.

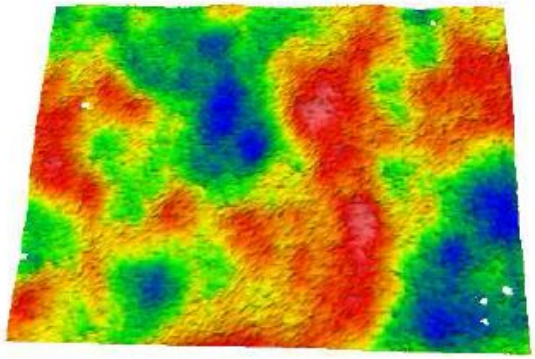

Figure 6.15: This picture shows the profile of the surface of the flat mirror near the center of the sample.

Zygo Verifire

This other Zygo device is working with a He-Ne light source at 633nm (monochromatic). It can analyze the whole surface of the sample at the same time and also

performs wavefront measurements.

The Zygo Verifire is first used in normal incidence. It was noticed that the measurement was disturbed by a static pattern of fringes:

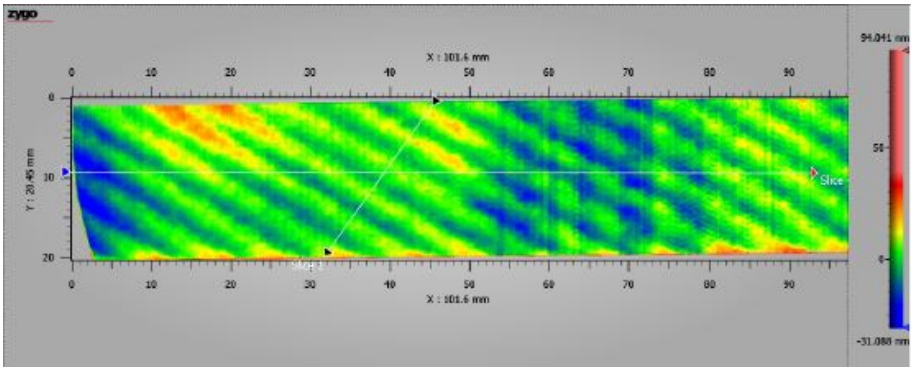

Figure 6.16: This picture shows the profile of the surface of the flat mirror.

Those internal fringes have a period of around 1mm and they are static fringes. They do not correspond to the striped patterns observed on the HHG beam profile (period 0.2mm) but it is possible to know which kind of periodic structure can create those by building a model of a virtual grating located at the same spot as the toroidal mirror (focusing optics).

Let's take the example of a transmission grating where the angle of incidence is zero. Knowing the distance L from the supposed grating (located on one of the two mirrors of the focusing set-up) and the XUV camera ($L \approx 3m$) and the distance Δx separating two lines of the spectrum (the 0.2mm period calculated before), one can express the problem with the following relationship:

$$\Delta x = L\left(tan\left(\frac{m\lambda_2}{d}\right) - tan\left(\frac{m\lambda_1}{d}\right)\right) \tag{6.7}$$

Where d is the parameter we are looking for, that is to say the groove parameter in m/lines. λ_1 and λ_2 are the wavelengths of two consecutive harmonics and m is the diffraction order. In the case of first order of diffraction, a number of 0.1 lines/mm is found and this is not realistic for a grating. Moreover, this does not correspond to the 1mm periodic pattern found during ZYGO measurements.
However, focusing also has to be taken into account because there is still the toroidal mirror which focuses the beam, thus it reduces the actual angle of diffraction of the virtual grating considered above. Indeed, the toroidal mirror has a focal length of 4m and the image taken by the vacuum camera of the beam profile is located at 3m. This means that the Δx parameter has to be corrected by a magnification factor

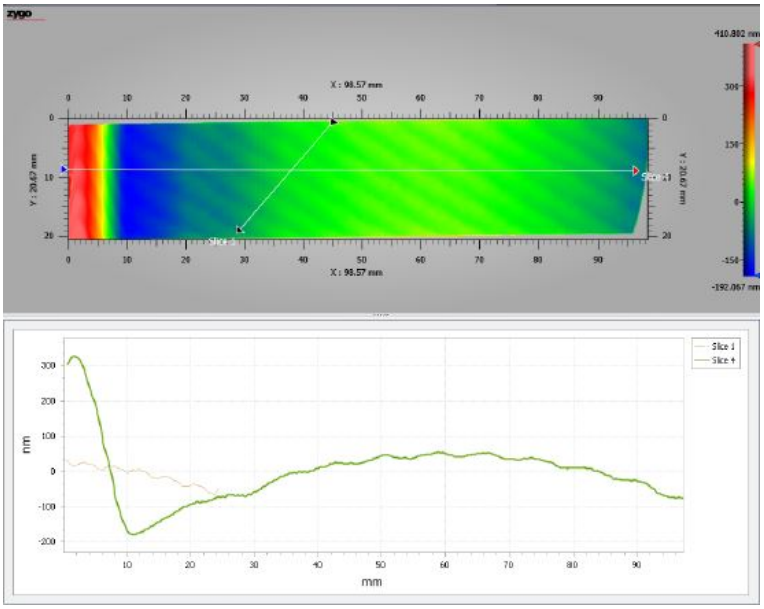

Figure 6.17: This picture shows the profile of the surface of the flat mirror on one side of the sample (left part) at normal incidence.

because it appears on the camera smaller than it actually is due to the reduced angle of diffraction. The correction factor is 4 for our configuration and it gives a new value of the parameter $\Delta x = 0.8mm$. The Matlab simulation which involves the formula for gratings gives for this parameter a result of 0.35 lines/mm, which is still too low compared to what we observed.
In the case of reflecting grating at grazing incidence (2degrees), the result is the same.

The sides of the sample were also studied:

Moreover, as the flat mirror is normally used at grazing incidence in our set-up (2 degrees) it is also possible to perform interferometric measurements at “grazing“ incidence (here 10.5 degrees).

In this last case, the standard deviation is 14nm (rms value). This mirror could cause wavefront distortions mostly in the tangential direction (horizontal). In the case of the Marechal criterion, the distortion, in order to keep a good wavefront, must be smaller than $\frac{\lambda}{14}$. This gives the following relation for the maximal roughness height (rms) which can be achieved [21]:

$$2 \times h_{rms} \times \theta_{gra} \leq \frac{\lambda}{14} \tag{6.8}$$

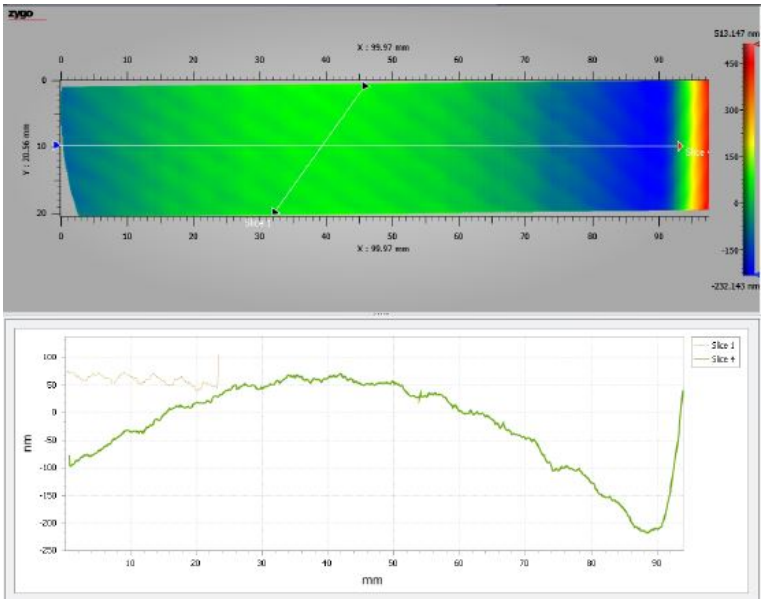

Figure 6.18: This picture shows the profile of the surface of the flat mirror on one side of the sample (right part) at normal incidence.

Where θ_{gra} is the grazing incidence angle in the measurement (10.5 degrees). For high-harmonics, let's take a medium wavelength: 40nm. Then the calculated maximum rms roughness is of the order of 0.1-0.2nm. Thus the beam profile obtained must be somehow distorted.

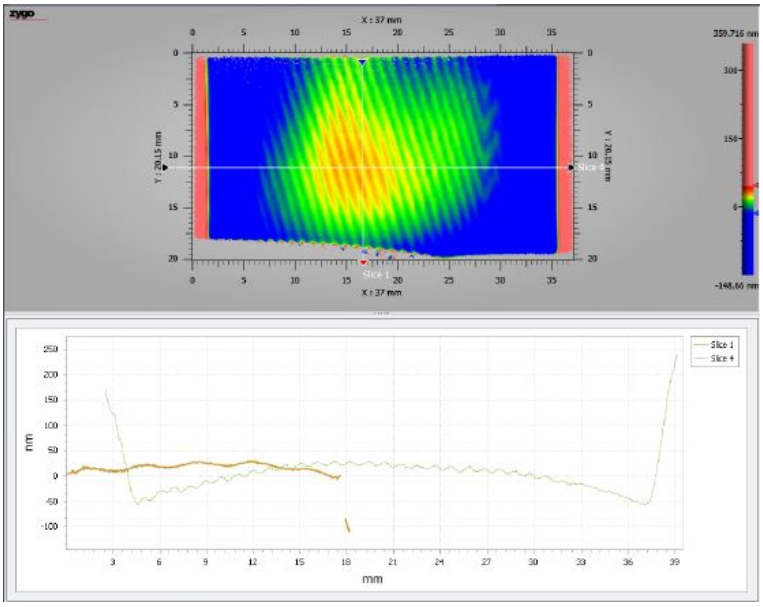

Figure 6.19: This picture shows the profile of the surface of the flat mirror in the center at grazing incidence.

Chapter 7

Temporal reconstruction of the XUV pulses

The unique temporal feature of high-harmonic beams is the duration of the XUV pulses which can be in the attosecond time scale. One challenge is that new methods are needed to characterize such ultrashort pulses.
In the lab, researchers are implemented a technique to reconstruct the temporal shape of XUV pulses called streaking. The light-field streaking technique enables to measure this temporal profile [18]. This chapter will first introduce what this method consists in and then another reconstruction technique will be presented: RABBIT. The set-up for this latter method was implemented during this master thesis project.
Streaking measurements were not performed during this master thesis project, but an introduction of this method is presented here.

7.1 Principle of streaking measurements

The principle is the following: an infrared beam is used to accelerate photo-electrons created by the XUV beam to be characterized. The change in photo-electron energy is measured. The XUV beam and the IR beam overlap collinearly. The XUV beam is focused onto a gas jet and ionizes the electrons. Those electrons are then streaked by the oscillating electric field of the IR laser beam. The change in photo-electron energy is directly linked to the phase of the oscillating electric field at the time where the ionization process occurs. Near-infrared beams are used to characterize attosecond pulses or far-infrared beams to characterize femtosecond pulses. This far-infrared light is mainly in the THz domain. Thus the XUV pulse is shorter than the oscillation time of the IR field and it is possible to map the XUV pulse temporal profile thanks to photo-electron energies.

This technique differs from the conventional streak camera method which in-

volves a photo-cathode and the generation of an electron bunch when the x-ray pulse hits the photo-cathode. Those electrons are then accelerated and deflected by a field while sent to a detector. The spatial distribution of the electrons is mapped. The resolution is poorer with this technique (hundreds of fs) due to the momentum dispersion.

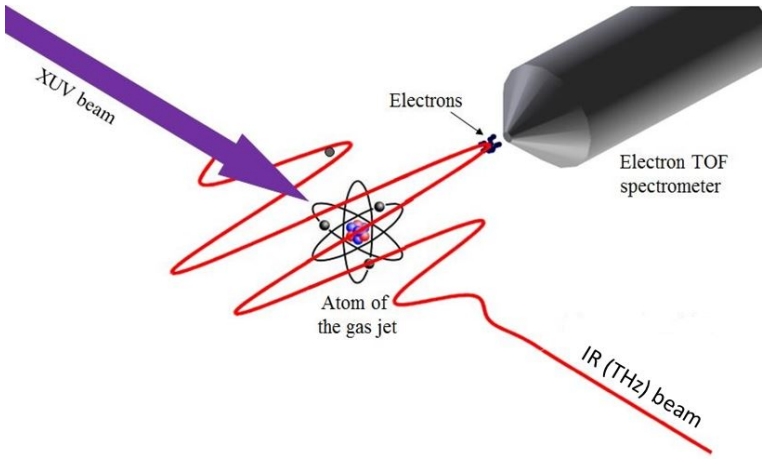

Figure 7.1: This sketch shows the basic lay-out of the set-up for the measurement and the interactions of the different beams.

7.2 Streaking theory

For this streaking process with light, it is assumed that the XUV and THz beams are impinging on the gas jet collinearly [17]. The aim is to determine the expression of the change in photo-electron energy due to the streaking process. In order to do this, i is possible derive the expression from the change in momentum or the change in electron velocity.
The electric field of the IR beam is defined as follows:

$$E_{\mathrm{THz}}(t) = E_0 \cos\left(\omega_{\mathrm{THz}} t + \phi\right) \tag{7.1}$$

The time when the ionization takes place as t_0 is also defined. It is the exact moment at which the photo-electron is released from the gaseous medium. At t_0 the photo-electron has the initial velocity v_0 and it is then accelerated by the electric field of the THz beam. So the final velocity of the photo-electron can be expressed as:

$$v_{\mathrm{final}} = v_0 + v_{\mathrm{THz}} \tag{7.2}$$

Where v_{THz} is derived from the acceleration:

$$v_{\mathrm{THz}} = \int a_{\mathrm{THz}} = \int -\frac{eE_{\mathrm{THz}}}{m_{\mathrm{e}}} \tag{7.3}$$

Where m_{e} is the mass of the electron. The vector potential of the streaking field is:

$$E_{\mathrm{THz}} = -\frac{dA_{\mathrm{THz}}}{dt} \tag{7.4}$$

This means that the final velocity of the photo-electron after acceleration by the streaking field can be expressed as:

$$v_{\mathrm{final}} = v_0 + \frac{eA_{\mathrm{THz}}}{m_{\mathrm{e}}} \tag{7.5}$$

Thus, the vector potential of the streaking field can be determined through:

$$\begin{aligned} A_{\mathrm{THz}}(t) &= -\int_{t_0}^{\infty} E_{\mathrm{THz}}(t')dt' && (7.6)\\ &= \frac{E_0}{\omega_{\mathrm{THz}}} \sin\left(\omega_{\mathrm{THz}} t + \phi_0\right) && (7.7) \end{aligned}$$

Where ϕ_0 is the phase of the electric field of the streaking beam at t_0. Thus, the kinetic energy of the photo-electron after acceleration by the streaking field is defined as:

$$E_{\mathrm{kin}} = \frac{1}{2} m_{\mathrm{e}} v_{final}^2 \tag{7.8}$$

After some calculations, the following result appears:

$$\begin{aligned} E_{\mathrm{kin}} = E_{kin}^0 + \frac{1}{2}\frac{e^2 E_0^2}{\omega_{THz}^2 m_e} \sin^2\left(\omega_{THz} t_0 + \phi_0\right) \\ + e\sqrt{\frac{2E_{kin}^0}{m_e}} \frac{E_0}{\omega_{THz}} \sin\left(\omega_{THz} t_0 + \phi_0\right) \end{aligned} \tag{7.9}$$

Where $E_{kin}^0 = \frac{1}{2} m_e v_0^2$ is the kinetic energy of the photo-electron right after ionization. In chapter 3, the ponderomotive potential was expressed as:

$$U_P = \frac{e^2 E_0^2}{4 m_e \omega_{THz}^2} \tag{7.10}$$

Then, the equation (5.17) becomes:

$$E_{kin} = E_{kin}^0 + 2U_P \sin^2\left(\omega_{THz} t_0 + \phi_0\right) + \sqrt{8E_{kin}^0 U_P} \sin\left(\omega_{THz} t_0 + \phi_0\right) \tag{7.11}$$

The second term in the above equation can be neglected by approximation. Indeed, the streaking field has frequencies in the THz domain, this means that for this field U_P is very small. Thus one is left with the third term which is the change in photo-electron kinetic energy due to streaking process:

$$E_{kin} = E^0_{kin} \pm \Delta E = E^0_{kin} \pm \sqrt{8E^0_{kin}U_P}\sin\left(\omega_{THz}t_0 + \phi_0\right) \tag{7.12}$$

Let's assume that the duration of the XUV pulse is way shorter than the period of the oscillations of the streaking field. Thanks to an optical delay stage on the THz generation set-up, one can also monitor the delay such that the XUV pulse coincides with a zero-crossing of the streaking field vector potential.
As said previously, the arrival time measured for the photo-electrons (that is to say their release time from the atom) is directly linked to their change in energy, or momentum.

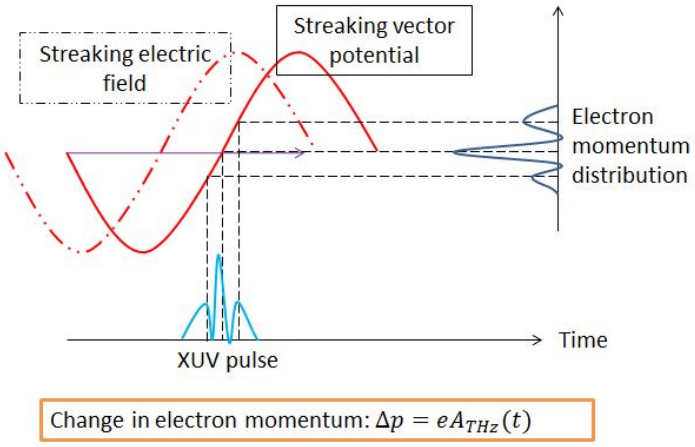

Figure 7.2: This sketch adapted from [18] shows that the incoming XUV pulse generates through the gas jet an electron beam with same temporal properties as the initial pulse. The knowledge of the vector potential allows to map the change in energy/momentum of the electrons.

One challenge is that most of the time, the incoming XUV pulse has a chirp. If this was not the case, this would be easier given that the streaking spectrum which could be obtained from Time-Of-Flight spectrometers would be directly the representation of the XUV pulse shape.
In the case where the initial XUV pulse has a chirp, it is necessary to use several streaked spectra to reconstruct the whole pulse profile. This is why the set-up involves two Time-Of-Flight spectrometers (parallel and anti-parallel) as it will be

shown later on.

Let's now assume that the incident XUV pulse has a linear chirp and that the profile is Gaussian:

$$E_{XUV}(t) = E_0 \exp\left(-a(t-t_0)^2\right) \exp\left(\mathrm{i}(\omega_0(t-t_0) + c(t-t_0)^2)\right) \tag{7.13}$$

Where c is the linear chirp rate. In our case, where there are parallel and anti-parallel spectrometers, depending on which one you measure the arrival time of the electrons, the electron beam will not see the same streaking electric field. Indeed, the streaked spectra will be broader or narrower whether the streaking field the electrons see is positive or negative. This change of sign is experimentally realized by placing two Time-Of-Flight spectrometers in parallel and anti-parallel positions. In one case the ionization can happen while the electron see a positive slope of the vector potential of the streaking field. So the electrons generated by the first part of the XUV pulse will be even more decelerated and the ones generated at the end of the pulse will be even more accelerated leading to a broader streaked spectrum in comparison with the incident chirped spectrum. If the slope of the vector potential that is seen by the electrons is negative, the reverse phenomenon will happen and we get a streaked spectrum which is narrower. Studying the relative difference between those two types of spectra can enable to derive the linear chirp of the incident XUV pulse.

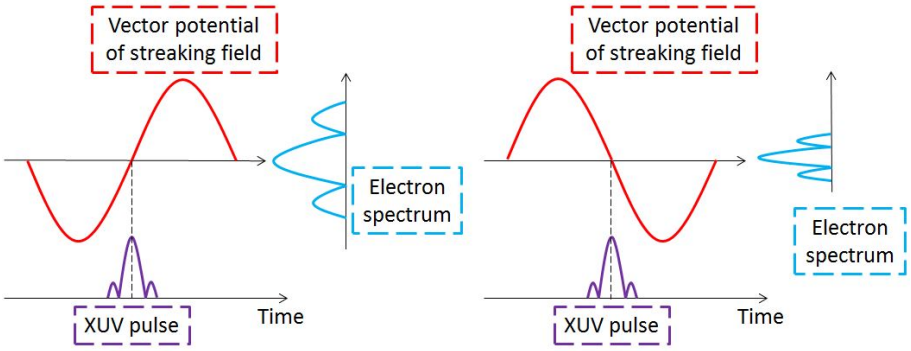

Figure 7.3: This sketch shows the response of the streaked spectrum depending on the slope of the vector potential of the streaking field.

From quantum mechanics the shape of the spectrum which undergoes streaking can be defined as (see details in [18]):

$$S(\omega) = \left| - \int_{\infty}^{\infty} d_{ion} E_{XUV}(t) \exp(\mathrm{i}\phi(t)) \exp(-\mathrm{i}\omega t) dt \right| \tag{7.14}$$

Where d_{ion} is the dipole element for ionization process and the phase $\phi(t)$ is given by:

$$\phi(t) \approx \sqrt{\frac{8E^0_{kin}U_P}{\omega^2_{THz}}} \cos\theta \left(1 - \frac{\omega^2_{THz}t^2}{2}\right) \tag{7.15}$$

Where θ is the observation angle between the laser polarization direction and $\vec{v}$ the final velocity of the photo-electron. From the width of the streaked spectrum, the rms duration of the XUV pulse can be derived:

$$\sigma_{Streaked} = \sqrt{\sigma_0^2 + \tau^2_{XUV}(s^2 \pm 4cs)} \tag{7.16}$$

Where σ_0 is the width of the unstreaked spectrum and s is the streaking speed, that is to say the derivative of the change in kinetic energy:

$$s = \frac{\partial \Delta E_{kin}}{\partial t} \tag{7.17}$$

Where the $\pm$ sign translates the fact that either the signal from the parallel (1) or the anti-parallel (2) Time-Of-Flight spectrometer is used. From the previous equation, the pulse duration and the linear chirp rate for the XUV pulse can be expressed as follows:

$$\tau_{XUV} = \sqrt{\frac{(\sigma^2_{streaked1} - \sigma_0^2) + (\sigma^2_{streaked2} - \sigma_0^2)}{2s^2}} \tag{7.18}$$

$$c = \frac{\left(\sigma^2_{streaked1} - \sigma_0^2\right) - \left(\sigma^2_{streaked2} - \sigma_0^2\right)}{8s\sigma^2_{XUV}} \tag{7.19}$$

The energy shift of the photo-electrons which is measured can also be used to completely map the streaking field (THz beam). From equation (5.20) an approximate expression for the change in photo-electron energy is derived:

$$\Delta E_{kin} \approx \sqrt{\frac{2E^0_{kin}}{m_e}} e A_{THz}(t) \tag{7.20}$$

In order to reconstruct the complete temporal profile of the XUV pulse, several algorithms can be used, for instance FROG-CRAB [20,21]. An example of raw data obtained through such measurement can be the following spectrogram:

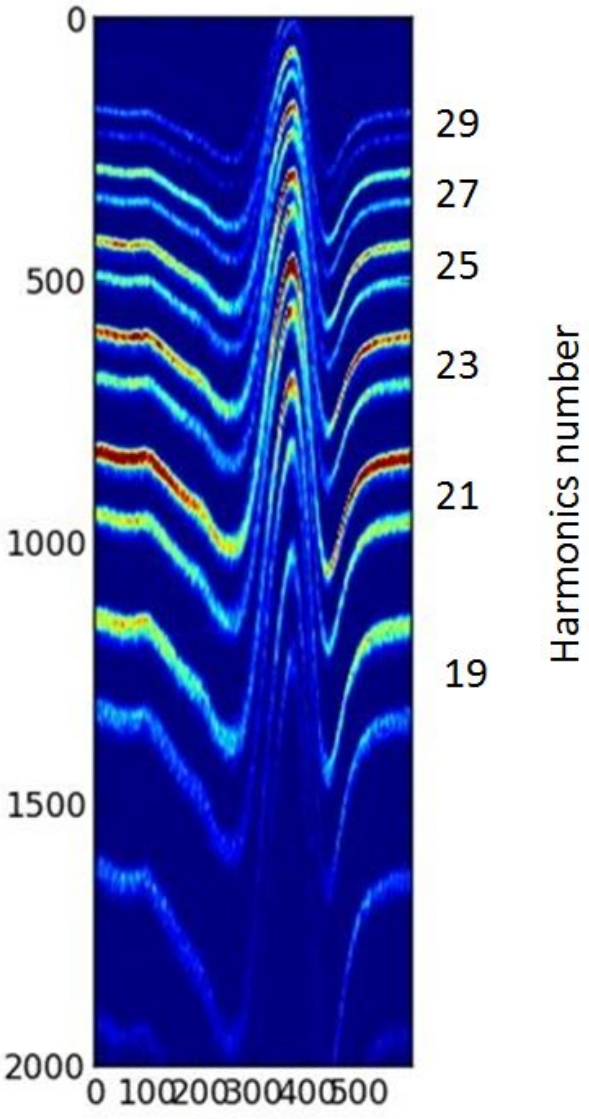

Figure 7.4: These curves represent the different harmonic lines and the change in kinetic energy due to the streaking effect. The axis are not calibrated but one represents the motor position of the delay stage (abscissa) and can be calibrated to time and the other is the arrival time of electrons on the Time-Of-Flight spectrometer, it can be calibrated to give the kinetic energy. The generation medium is Argon and the gas used in the gas jet is Xenon. The first ionization energy of Xenon is 12.13eV and the lines in the spectrum are doubled, see [29].

The THz field use to streak the photo-electrons has the following spectrum, with a central frequency at 0.2THz:

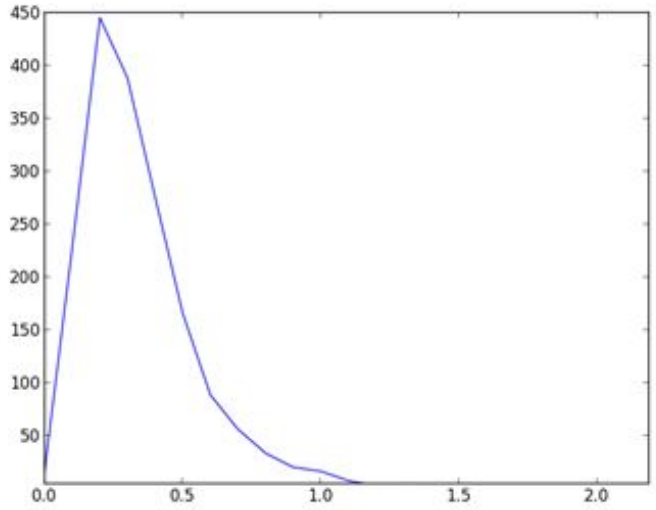

Figure 7.5: This curve represents the spectrum of the THz radiation used for streaking. The abscissa is given in THz.

7.3 Measurement of the gas jet size

It was said previously that the experimental streaking chamber contains a gas jet. A measurement which can be done is to determine the size of the actual gas jet in the section where the gas is ionized by the XUV beam. In order to do that, the XUV beam from high-harmonic generation is used and sent directly to the gas jet. The THz field for streaking is not used and only the electrons issued from ionization mechanism are recorded by the two Time-Of-Flight spectrometers. The signals from both spectrometers (CH2 and CH3) are displayed on the oscilloscope. One can remind that the streaking chamber is motorized and can be slightly moved with respect to the general vacuum line by some mm.

So the principle of this small experiment is to measure the photo-electron signal for different positions of the streaking chamber. One should observe a maximal signal when the XUV beam hits the center of the gas jet and a minimum signal (extinction) when the XUV beam is at the edge of not hitting the gas jet any longer.

The signals from the two spectrometers are of this type:

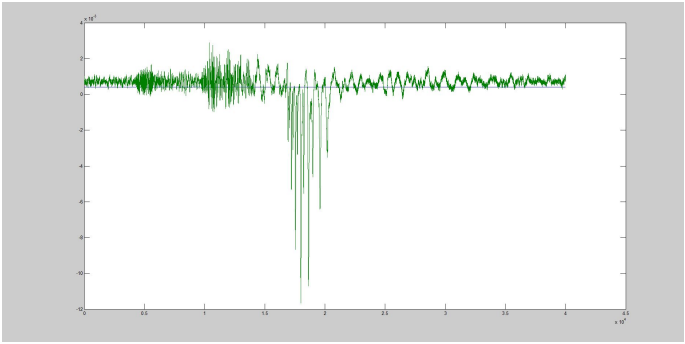

Figure 7.6: This curve represents the photo-electron signal of one of the spectrometers.

For the different positions of the chamber, the signals are recorded and according to the evolution of the intensity of the signal for the different positions, a Gaussian fit is applied in order to determine the width of the gas jet. The result is the following:

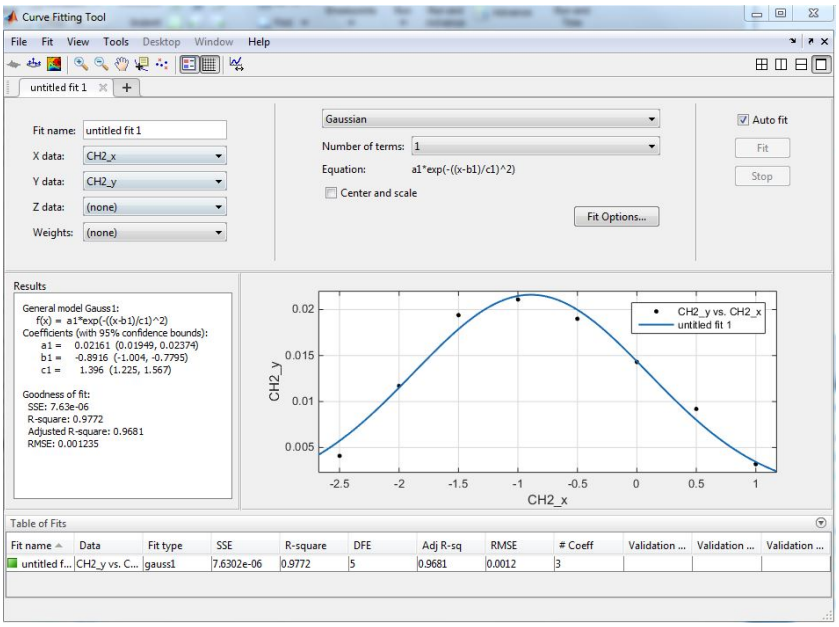

Figure 7.7: This screen shot represents the Gaussian fitting to the experimental data.

Finally, it happens that the FWHM of the gas jet is 1.4mm.

7.4 RABBIT principle

The RABBIT method is also used to characterize XUV pulses. It stands for Reconstruction of Attosecond harmonic Bursts By Interference in Two photon transition [19].
The principle of this technique is to measure the signal of a photo-electron which is created thanks to a two-photon transition process by a two-colors ionization. The medium (gas jet) is ionized with the XUV beam generated in a hollow waveguide (HHG) and then a second beam (IR, Ti:Sa at 800nm) is used for the second transition.
Under the action of the XUV beam, one electron goes from the ground state $|g\rangle$ to an intermediate state $|i\rangle$ where it can then absorb or emit one photon (IR photon at ω_{IR}) to go to a final state $|f\rangle$. The frequencies obtained by high-order harmonic generation are odd multiples of the fundamental frequency of the Ti:Sa so with the absorption or emission of one photon at the fundamental frequency, RABBIT process leads to the appearance of frequencies which are even multiples of the fundamental. They are called sidebands (here q is the order of the sideband).
In order not to trigger multi-photon absorption with the IR beam, this one has to be quite low in intensity so there are still these even multiples of the fundamental frequency.

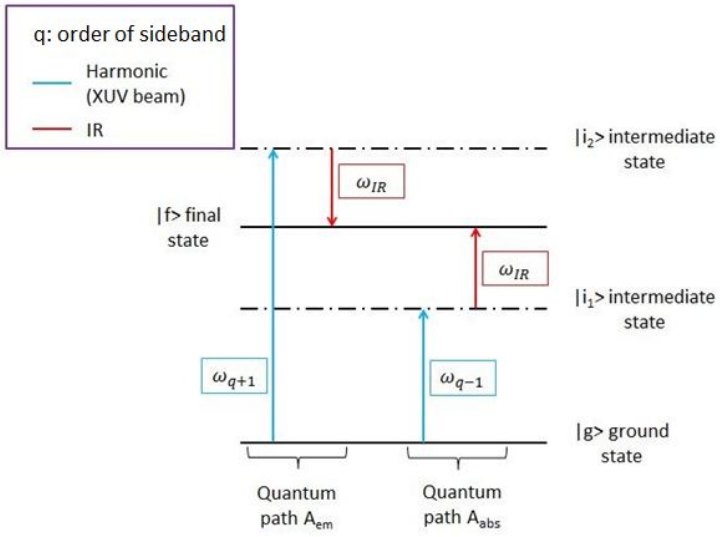

Figure 7.8: This sketch shows the transitions at stake in RABBIT process.

It is possible to define two different quantum paths, as shown on the previous sketch. One relies on the absorption of the harmonic photon or lower order followed by the absorption of one IR photon (absorption quantum path). The second one relies on the absorption of the harmonic photon of higher order followed by the emission of one IR photon (emission quantum path).
For the high-harmonic, the electric field can be expressed as:

$$E_{XUV}(t) = E_q \exp\left(-\mathrm{i}q\omega_{IR}t - \phi_q\right) \tag{7.21}$$

Where ϕ_q is the phase of the q^{th} harmonic and the electric field of the IR beam is just the following:

$$E_{IR}(t) = E \exp\left(-\mathrm{i}\omega_{IR}t\right) \tag{7.22}$$

As in streaking experiments, the two beam are delayed with respect to each other by τ and thus, the signal contained in the sideband reached by two-photon transition is obtained thanks to perturbation theory:

$$S(q,\tau) \propto \left| \int_{-\infty}^{+\infty} \left(A_{em} + A_{abs}\right) dt \right|^2 \tag{7.23}$$

It is possible to demonstrate [23] that the sideband signal can be expressed as:

$$S(q,\tau) \propto S_0 + S_1 \cdot \cos\left(\Delta\phi_q^{at} + \Delta\phi_q + 2\omega_{IR}\tau\right) \tag{7.24}$$

Where S_0 and S_1 are related to squared amplitudes, $\Delta\phi_q^{at}$ is the atomic phase and $\Delta\phi_q$ is the relative phase difference between two consecutive harmonics:

$$\Delta\phi_q^{at} = \phi_{em}^{q+1} - \phi_{abs}^{q-1} \tag{7.25}$$

$$\Delta\phi_q = \phi_{q+1} - \phi_{q-1} \tag{7.26}$$

The delay introduced between the XUV beam and the IR beam allows to control the oscillating term of the sideband signal. If the atomic phase is known, the relative phase difference between two adjacent harmonics can be retrieved thanks to the oscillation.

This atomic phase is the phase acquired by the electron from the XUV ionization, when it is removed from the atom. In some cases (generation in Argon), the atomic phase can be neglected. Then, the harmonic phase difference can be linked to the emission time of the XUV pulse:

$$S(q,\tau) \propto \cos\left(\Delta\phi_q + 2\omega_{IR}\tau\right) \tag{7.27}$$

$$\Delta\phi_q = \phi_{q+1} - \phi_{q-1} \tag{7.28}$$
$$\approx 2\omega_{IR} \cdot \frac{d\phi_q}{d\omega} \tag{7.29}$$
$$\approx 2\omega_{IR} t_{em} \cdot q \tag{7.30}$$

Where t_{em} is the emission time of the pulse.

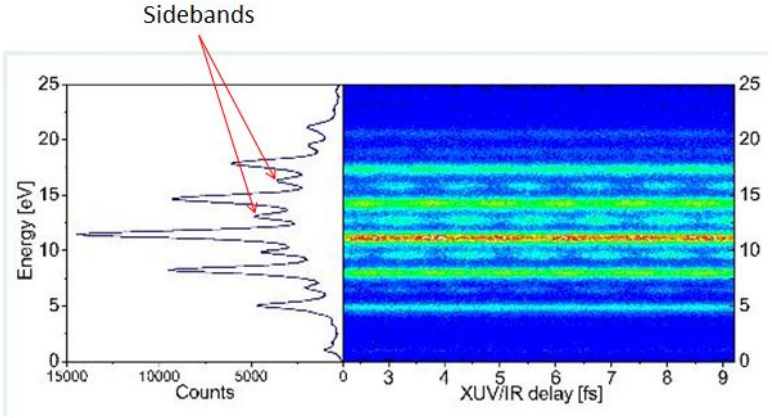

Figure 7.9: This sketch, adapted from the Max Planck Institute website, shows the appearing sidebands in the spectrum and the consequences on the recorded spectrogram.

The spectrogram which shows the energy evolution of the photo-electrons is dependent on the delay between the XUV pulse and the IR beam and it contains the spectral phase information which allows to map the XUV pulses.

7.5 RABBIT set-up

To implement the RABBIT set-up, the streaking chamber is used but the probing beam is replaced by the fundamental beam at 800nm. In order to be able to do quick comparison measurements between streaking and RABBIT, the two reconstruction methods, the IR optical path is built so that it mimics the optical path of the THz field previously used.

This gives the following set-up, involving a periscope in order to get the beam at the correct height:

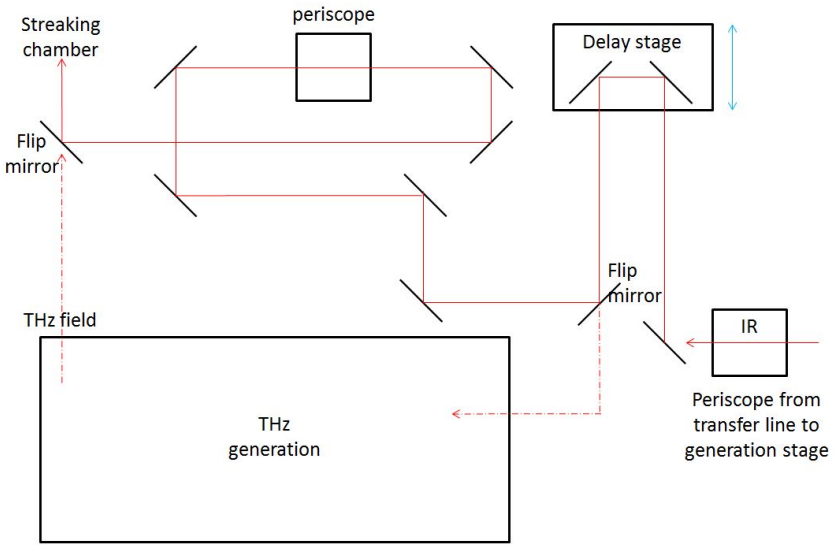

Figure 7.10: This sketch show the implemented optical set-up for RABBIT measurements. It contains two mirrors with flip mounts so that one can quickly shift from RABBIT measurement to streaking.

In order not to trigger multi-photon absorption process, the energy needed for RABBIT measurements is reduced thanks to optical densities and also with an iris.

The most important alignment feature in this setup is to find the temporal overlap between the XUV beam and the IR beam. This is done thanks to a BBO crystal located after a focusing lens at the output of the streaking vacuum chamber. The XUV beam is focused first (actually the 800nm of the HHG line) in the crystal and the SHG signal is recorded after by a fast photodiode. The crystal is aligned so that the signal is maximized. Then the IR beam is sent to the crystal and the goal is to overlap first spatially the beams by adjusting the alignment mirrors of the IR delay set-up. Then thanks to the photodiode and the previous recorded signal of the XUV line, the delay stage is adjusted to find the temporal overlap between the two beams.
The delay stage is then limited to a useful range around this position and the scans for the RABBIT measurements can be done. Unfortunately, we did not have time to perform the scans before the streaking chamber was removed from the lab due to heavy construction works, but the set-up is operational for the measurements.

Chapter 8

Conclusion and outlook

This master thesis project aimed at generating high-order harmonics in neutral gases through gas cells and more specifically to improve the generating set-up.
One first step was to characterize the laser source used for generation: spectrum, pulse duration, divergence, waist size. The HHG beam line was optimized, especially, by changing the focusing design to have the target at 3m from the focusing optics. The lens was replaced by a spherical mirror in order to avoid any chromatic aberration.
Another step of this project was to study the XUV beam profile and its irregularities. Some might be induced by the mirrors of the focusing combination. This is why the surface quality of the flat mirror was checked thanks to a Zygo interferometer.

One main achievement was to commission a XUV spectrometer, to align it, to calibrate it and to display calibrated spectra of high-harmonics generated in different gases such as Argon, Neon or Helium. Thanks to this work, parametric studies on the high-harmonic spectrum were done. Indeed, the influence of the gas pressure on the signal strength for particular energies was investigated leading to an enhance phase-matching for higher energies in Neon.

The XUV beam is also meant to be characterized in the temporal domain through the streaking technique by THz field used by the researchers of the lab. This technique was presented here but not investigated during this master thesis project. However, a set-up for RABBIT measurement, a temporal reconstruction method, was prepared during this project in order to be implemented soon. It will allow researchers to compare the results obtained to the one given by streaking measurements.

The largest issue of this project was the beam quality which still needs to be improve, as the beam profile can testify. The toroidal mirror has not yet being

studied as source of those irregularities and we also wondered if there might be filamentation phenomenon in the initial laser source.

The future developments will involve the use of OPA output in mid-IR in order to generate harmonics of higher orders given that the cut-off law scales with the wavelength squared. Thus, it could be possible to reach higher photon energies.

Bibliography

[1] S. Reiche, “Overview of seeding methods for FELS“, proceedings of IPAC2013, China, 2013.

[2] G. Schneider,”Cryo x-ray microscopy with thigh spatial resolution in amplitude and phase contrast”, Ultramicroscopy, 1998.

[3] D. Bauer, “Lecture notes, derivation of the ponderomotive potential“.

[4] Ammosov, Delone and Krainov (ADK), JETP, 1991.

[5] C.-G. Wahlstrom and al., “High-order harmonic generation in rare gases with an intense short-pulse laser“, Physical Review A, 1993.

[6] Tenio Popmintchev, Ming-Chang Chen, Paul Arpin, Margaret M. Murnane and Henry C. Kapteyn, “The attosecond nonlinear optics of bright coherent X-ray generation“, nature Photonics 4, 2010.

[7] M. Lewenstein and al., “Theory of high-harmonic generation by low-frequency laser fields“, Physical Review, 1994.

[8] Amplitude Technologies, “User’s manual“.

[9] Pierre Tournois, “Acousto-optic programmable dispersive filter for adaptive compensation of group delay time dispersion in laser systems“, Optics Communications 140, 245-249, 1997.

[10] T. Oksenhendler, D. Kaplan, P. Tournois, G. M. Greetham, F. Estable, “Intracavity acousto-optic programmable gain control for ultra-wide-band regenerative amplifiers“, Appl. Phys. B 83, 491-495, 2006.

[11] Website of GT Advanced Technologies.

[12] X-ray database website, `http://henke.lbl.gov/optical_constants`.

[13] Mikhail Grishin, “Advances in solid state lasers development and applications“, ISBN 978-953-7619-80-0, 2010.

[14] T. Oksenhendler and al., “Self-Referenced Spectral Interferometry“, Applied Physics B, 2010.

[15] A. Trisorio and al., “Self-referenced spectral interferometry for ultrashort infrared pulse characterization“, Optics Letter vol. 37, No. 14, 2012.

[16] Robert W. Boyd, “Nonlinear Optics“, Academic Press, third edition, ISBN-13 978-0123694706, 2008.

[17] Ulrike Frühling, “Tutorial: Light-field streaking for FELs“, J. Phys. B: At. Mol. Opt. Phys. 44, 2011.

[18] U. Frühling and al., “Single-shot terahertz-field-driven X-ray streak camera“, Nature Photonics, 2009.

[19] P. M. Paul and al., “Observation of a train of attosecond pulses from high harmonic generation“, Science vol. 292, 2001.

[20] A. G. Stepanov, “Efficient generation of terahertz radiation by the method of optical rectification of terawatt laser pulses“, Optics and Spectroscopy, vol. 107, 2009.

[21] P. Heimann and al., “Linac coherent light source soft x-ray materials science instrument optical design and monochromator commissioning“, Review of Scientific Instruments 82, 2011.

[22] L. V. Keldysh, ”Ionization in the field of a strong electromagnetic wave”, JETP 47, 1964.

[23] V. Tosa and al, ”Generating single attosecond pulse using multi-cycle lasers in polarization gate”, Optics Express vol.17 no.20, 2009.

[24] D. Strickland and G. Mourou, ”Compression of amplified chirped optical pulses”, Optics Communications vol.56, no.3, 1985.

[25] E. B. Treacy, ” Optical pulse compression with diffraction gratings”, IEEE Journal of Quantum Electronics vol. QE-5 no.9, 1969.

[26] R. Lopez-Martens and al., ”Amplitude and phase control of attosecond light pulses”, Physical Review Letters 94, 2005.

[27] C. Erny and al, ”Metrology of high-order harmonics for free-electron laser seeding”, New Journal Of Physics 13, 2011.

[28] W. C. Tan and al., ”Optical properties of condensed matter and applications”, John Wiley and sons Ltd, 2006.

[29] P. N. Juranic and al, "A scheme for a shot-to-shot, femtosecond-resolved pulse length and arrival time measurement of free electron laser x-ray pulse that overcomes the time jitter problem between the FEL and the laser", IOP publishing Ltd and Sissa Medialab srl, 2014.

Appendix A

Ti:Sapphire solid state medium

At the beginning, femtosecond lasers systems where based on dye solutions. Dye solutions can provide a gain bandwidth of around 100nm (Rhodamine for instance). However, those materials have maintenance defects (degradation of the medium) and can be toxic. Thus, solid state materials were preferred. The one with the highest bandwidth and most suitable for generating short pulses is Ti:Sapphire. It provides the largest gain bandwidth from around 600 to 1000nm.

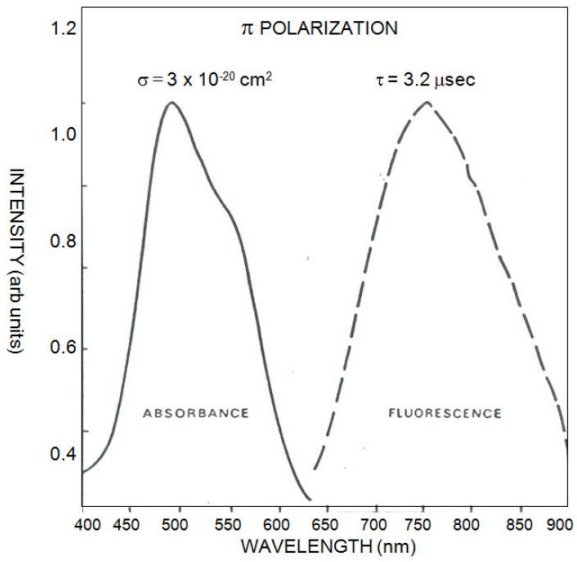

Figure A.1: This curves represent the absorption and emission spectra of Ti:Sa at 300K. Data taken from [11].

Appendix B

Kerr lens mode-locking

The mode-locking technique used here is a passive one.It consists in Kerr lensing in the gain medium. This lensing effect causes a reduction of the beam size while the intensity increases inside the medium.
Let's consider a Gaussian beam profile propagating in the nonlinear medium, the intensity profile can be expressed as:

$$I(r) = \exp\left(-\gamma r^2\right) \tag{B.1}$$

Where r is the radial coordinate (transverse profile $r^2 = x^2 + y^2$) and γ is a parameter characterizing the shape of the profile while propagating. In presence of high intensities, which is the case for femtosecond lasers, the refractive index in the nonlinear medium exhibits a dependence with the intensity:

$$n^{\text{med}}(r) = n_0 + \frac{n_2 I(r)}{2} \tag{B.2}$$

In the above equation, n_2 is the nonlinear refractive index coefficient which describes the link between the electric field strength and the refractive index. This refractive index is modified along the beam path because of the intensity and is greater in the center of the beam than on the wings.
Thus self-focusing process can be witnessed in the center of the nonlinear medium when n_2 is positive, that is to say Lens Kerr effect.

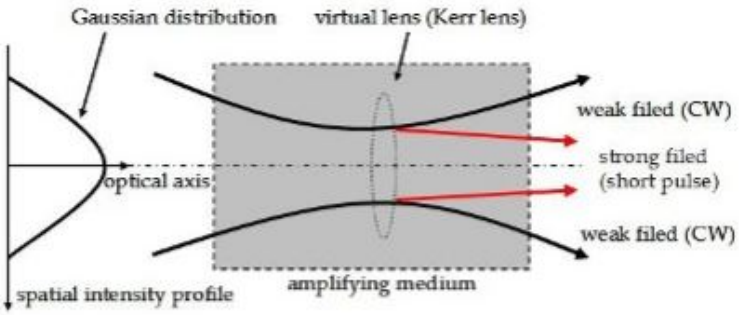

Figure B.1: This sketch explains how the Kerr lensing phenomenon is working. Picture taken from [13].

Let's consider a seeding Gaussian transverse profile propagating in the Ti:Sa crystal (the nonlinear medium) which is pumped by a CW beam at 532nm. For high intensity the Kerr lens effect is happening. Inside an usual resonator, the free-running laser can oscillate on different resonant frequencies at the same time (separated in frequency by $\nu = c/2L$ where L is the length of the cavity). However, in the case of Kerr lensing, some frequencies are more strongly focused and thus undergo a higher amplification.
Those frequencies are forced to have the same phase (mode-locking) so that the waves at different frequencies interfere constructively at one place, Thus one can get very high intensities and short pulses (pulsed regime).

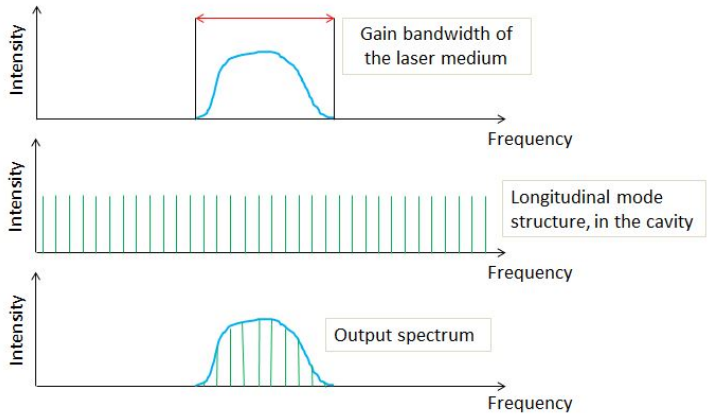

Figure B.2: These sketches explain mode-locking principle.

Appendix C

Alignment of the spectrometer

In order to proceed to the alignment of the spectrometer, we need first to remove the last part of the spectrometer (including the camera) up to the grating mount. We also remove the zero-order blocker. Obviously, the spectrometer arm also has to be vented.
We can use the Ti:Sa beam to align properly the optical path into the spectrometer. Initially, the whole vacuum line is aligned for high-harmonic generation, up to the Time-Of-Flight spectrometers located at the end of the beam line. A dichroic mirror and a toroidal mirror are used to focus the high-harmonics to the end of the line.
In order to send the beam into the spectrometer arm instead of the next vacuum chamber, we just need to remove the toroid mirror from the beam path because the deflection angle matches the orientation of the spectrometer arm with respect to the vacuum chamber.
When the Ti:Sa beam is well centered on the entrance of the spectrometer arm, we first check that the references of the moving motors of the grating stage are done. If it is not the case, go to the options menu and "find reference" for the three channels. The channel B (first knob on the SMARACT remote controller) is the position of the focus; channel A (second knob) is the motor which controls the translation perpendicular to the axis of the beam; and channel C (third knob) controls the rotation.
If the beforehand beam is well aligned, then one should see the Ti:Sa beam at the opened output of the spectrometer arm. One may use a screen (with a paper) placed parallel to the output of the arm and locate the impinging spot with a pen and if needed the IR viewer. The screen must be located as far as possible from the grating.

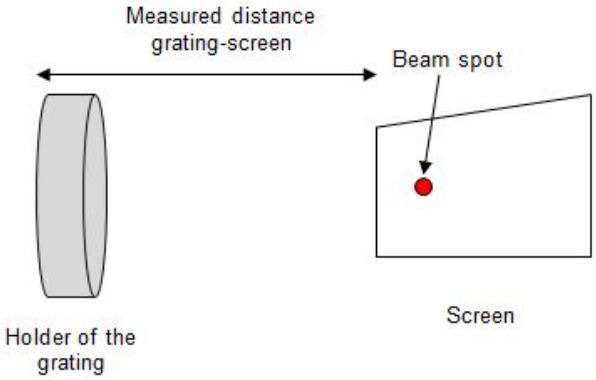

Figure C.1: This sketch shows the alignment procedure of the spectrometer.

Then, according to the documentation of the spectrometer, while we are using a grating of 1200 lines and a certain distance between the source of light and the spectrometer (distance capillary to spectrometer), one should have a total deflection angle of the beam of $2 \times 5.3 = 10.6 degrees$.
In the above configuration, one measures the distance D from the grating to the screen where the beam spot is seen, taking the farther edge of the holder as a reference and adding 5cm to the measured distance.
Then the aim is to find the future location of the diffracted spot after the grating according to those measurements.

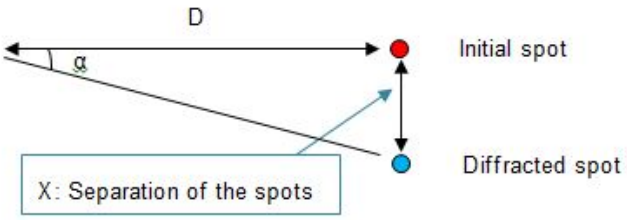

Figure C.2: This sketch shows how to determine the location of the diffracted beam.

As we know the deflection angle, the researched distance only needs a simple calculation:

$$X = D \cdot \tan(\alpha) \tag{C.1}$$

Then, during our first alignment we had the following data:

Table C.1: Alignment data

Deflection angle α (degrees)	10.6
Distance grating-screen D (cm)	36
Distance X (cm)	6.7

Then the next step is to get the deflected beam on the right spot. This is done first by turning the knob C which corresponds to the rotation controller. One must first see the apparition of the deflected spot next to the initial spot, but this spot is in the wrong place (not at the distance X from the initial spot). By going on turning the knob, one must see the spot going to the right place and the initial spot starting to disappear.

However, we are not done yet because we are not sure the beam hits the center of the grating. To do that we turn the knob of channel A such as the spot disappears on one side. We note the value of the controller. Then we turn on the other side of the knob and the spot should disappear on the other side. We note again the position. Then, we take the center of those two positions and then the beam must hit the grating more or less in its center. The last step consists in putting the zero-order blocker. To do that one adjusts the position of the cutting edge so that the operator no longer sees the zero-order beam (non-deflected beam).

The spectrometer is now aligned and one can put back the last part of the arm as well as the camera.

NB 1: References for the different channels in this configuration:

Table C.2: Channel configuration

Channel B	0mm
Channel A	0.87mm
Channel C	353.97 degrees

NB 2: Initializing of the motors with the SMARACT controller: Do “find reference“ for the three channels, then “calibrate“ and then again “find reference“.

Acknowledgments

I like to thank several people for the assistance they gave me during this thesis work. First I would like to thank F. Ardana, the PhD student who I worked with during those five months. I also thank my supervisor at PSI, C. Hauri, for creating this master thesis project and my supervisor at KTH, V. Pasiskevicius, who gave me good advice throughout the work as well as F. Laurell.

I also want to thank C. Erny for answering many questions and helping me with the report and the slides. A. Trisorio for patiently explaining the laser system, for the nice discussions in French and the car sharing to Lyon. A. Dax for his original ideas and his wish to learn new French words every day. J. Bossert and P. Mutter for sharing the office and the numerous chattering. S. Haüsler for the live translation of the Swiss German laser safety course. F. Enderli for his advice on doctoral studies and his bike! M. Divall for her home-made cookies and kindness.

I would like to thank R. Ganter, S. Bacher and A. Minikus for letting me participating to the FEL2014 conference in Basel and also for their kindness.

Finally, I also want to thank all member of the PSI basketball team. They made my stay in PSI sporty and enjoyable!